STRESS & DISPLACEMENT MEASUREMENT FOR GEOTECHNICAL MODELLING USING OPEN PLATFORM

by

Burak ÖZTÜRK

B.S., Civil Engineering, MEF University, 2018

Submitted to the Institute for Graduate Studies in
Science and Engineering in partial fulfillment of
the requirements for the degree of
Master of Science

Graduate Program in Civil Engineering

Boğaziçi University

2020

ACKNOWLEDGEMENTS

I would like to express my deepest gratitude to Prof. Gökhan Baykal for his invaluable guidance and encouragement extended to me throughout this thesis's preparation.

I also would like to thank members of the thesis committee, Prof. Ayşe Edinçliler, and Assist. Prof. Tanay Karademir for their valuable advice and supportive attitudes.

I wish to extend my special thanks to the staff at the laboratory for their kind help and research assistant, Uğurcan Erginağ, for his support and valuable comments throughout this study. The financial support provided by Bogazici University Scientific Research Fund (Project No: BAP-11A04D9 and BAP-18A04P2) is acknowledged.

Last but not least, my biggest thanks to my parents and my sister for their constant love and support they have provided me throughout my life and throughout this study. This wouldn't be possible without their encouragement and unconditional support.

ABSTRACT

STRESS & DISPLACEMENT MEASUREMENT FOR GEOTECHNICAL MODELLING USING OPEN PLATFORM

Stress and displacement measurements are key tasks for geotechnical modelling. Although broad range of techniques are available; the heterogeneity of the soil and the lack of direct observation of the foundation elements cause accurate measurements hard to obtain. Selection of whether a complicated acquisition system with expensive sensors, versus a simple but large number of sensors using open platforms, becomes a major challenge. To address this problem a range of approaches were implemented; a high-end data acquisition board connected to miniature stress transducers to measure the stress in the soil; sensitive films and a dedicated software to measure soil-structure contact stress; Arduino based IMU sensors for measuring inclination to calculate corresponding displacements and LVDTs for verification of the calculated displacements. A stress transducer, connected to a high-end data acquisition board, enclosed in a silicone pacifier that is filled with distilled water, was exposed to a set of different pressures under the soil. Although the results from experiments held on the same date were coherent, the repeatability at different dates was weak. The prescaled sensitive films and IMUs were attached on the blocks of the segmental pile, and the pile was placed in a large-scale direct shear test box which was then filled with loose sand. The pile head was fixed and was allowed to displace up to 5 cm with a rate of 1 mm per minute. It was observed that the obtained horizontal pressure by using the films was compatible with calculated value using the relation between the force and the area. Also, a series of three-point bending tests with external LVDTs were performed to verify the deflections from the inclination measured with IMUs. The calculated deflections were within the range of $\pm 10\%$ error when compared to those measurements from LVDTs.

ÖZET

GEOTEKNİK MODELLEME İÇİN GERİLME & DEFORMASYON ÖLÇÜMLERİNİN AÇIK PLATFORM YARDIMI İLE YAPILMASI

Gerilme ve deformasyon ölçümleri geoteknik modelleme çalışmalarının en önemli aşamasıdır. Bu ölçüm yöntemleri ile ilgili literatürde birçok yöntem yer alsada, zeminin heterojen bir yapıya sahip olması ve temel elemanlarının doğrudan gözlenememesi doğru ölçüm yapılmasını zorlaştırmaktadır. Tek ancak pahalı bir sensör ve üst-seviye veri toplama kartı kullanmak ile ucuz birçok sensörden oluşan, açık kaynak bir geliştirme kartı arasında seçim yapmak kullanım amacına bağlı olmak üzere büyük bir zorluk haline gelebilir. Bu problemi çözmek için bir kaç farklı yaklaşım uygulanmıştır. Zemin içerisindeki stresi ölçmek için üst-seviye bir veri toplama kartına bağlanmış bir minyatür basınç sensörü; uygulanan basıncı ölçmek için basınç ölçüm filmleri ve son olarak karşılık gelen deplasmanları ölçmek ve ölçülen değerleri doğrulamak üzere Arduino tabanlı ekonomik atalet ölçüm üniteleri (IMU) ve LVDT'ler kullanılmıştır. Basınç sensörü, silikon emzik içerisine yerleştirilmiş ve içerisi distile edilmiş su ile doldurulmuştur. Üst seviye bir veri toplama kartına bağlanan bu sensör, zemin içerisine yerleştirilmiş ve farklı basınçlar altında test edilmiştir. Aynı gün içerisinde yapılan deneylerde sonuçlar tutarlı olsada, farklı günlerde farklı sonuçlar elde edilmiştir. Basınç ölçüm filmleri ve IMU'lar eklemli kazığın blokları üzerine yerleştirilmiştir. Bu kazık büyük ölçekli bir direkt kesme cihazına yerleştirilmiş ve kutu düşük sıkılıkta kumla doldurulmuştur. Deney boyunca kazığın tepe noktası sabitlenmiş ve dakikada 1 mm hızla, 5 cm'ye kadar çekilmiştir. Basınç ölçüm filmlerinden elde edilen yanal basınç değerleri karşılaştırılmıştır. Oluşturulan kazık sistemine üç nokta eğilme deneyleri uygulanmış, IMU'lar ile hesaplanan deplasman değerleri LVDT'lerden elde edilen değerler ile karşılaştırılmış ve $\pm\%10$ hata ile deformasyon değerlerinin ölçülebildiği gözlenmiştir.

TABLE OF CONTENTS

LIST OF FIGURES

LIST OF TABLES

LIST OF SYMBOLS

a_{max}	Maximum Acceleration
a_{min}	Minimum Acceleration
a_{raw}	Acceleration (Raw)
B_x	Bias Matrix for X Axis
B_y	Bias Matrix for Y Axis
B_z	Bias Matrix for Z Axis
D	Depth
D_r	Relative Density
E	Young's Modulus
EI	Flexural Rigidity
F	Force
I	Moment of Inertia
K_0	Coefficient of At-Rest Earth Pressure
K_a	Coefficient of Active Earth Pressure
K_p	Coefficient of Passive Earth Pressure
L	Length
MPa	Megapascal
M_{max}	Maximum Moment
N	Newton
X_c	Corrected X-Axis
X_r	Raw X-Axis
Y_c	Corrected Y-Axis
Y_r	Raw Y-Axis
Z_c	Corrected Z-Axis
Z_r	Raw Z-Axis
cm	Centimeters
d	Depth
h	Height

hPa	Hectopascal
k	Soil Modulus
kPa	Kilopascal
kg-f	Kilogram-force
m	Meters
mV/V	Millivolts per Volt
min	Minute
mm	Millimeters
p	Pressure
σ_f	Flexural Stress
ϵ_f	Flexural Strain
ϕ	Roll, Internal Friction Angle
θ	Pitch
ψ	Yaw
μT	Micro Tesla

LIST OF ACRONYMS/ABBREVIATIONS

AHRS	Attitude and Heading Reference System
ASTM	American Society for Testing and Materials
DoF	Degree of Freedom
EPC	Earth Pressure Cell
HDPE	High-Density Polyethylene
IMU	Inertial Measurement Unit
I^2C	Inter-IC
LVDT	Linear Variable Displacement Transducer
MSE	Mechanically Stabilized Earth Wall
MTS	Material Test Systems
NI	National Instruments
N/A	Not Available
RGB	Red-Green-Blue
RMSE	Root Mean Square Error
SPVFR	Segmental pile with variable flexural rigidity
SSE	Error Sum of Squares
TBM	Tunnel Boring Machine
TML	Tokyo Measuring Instruments
USCS	Unified Soil Classification System

1. INTRODUCTION

Stress and displacement measurements are key tasks for geotechnical modelling. Although measuring instruments have evolved dramatically with the technological advancements in this century, it still does not provide complementary solutions to fully understand the behavior of the soil. Because of the heterogenetic and anisotropic nature of the soil, researchers are in need of cost-effective and reliable solutions for stress and displacement measurements.

Researchers have used expensive analogue instruments for centuries, which requires labour and time. By virtue of technological advancements, measuring instruments evolved into electronic devices. Although improvements in hardware and software components were led to fully automated closed-loop measurement systems and make measurement tasks easier, it has created other difficulties such as additional training of staff and decreased freedom of control over the process.

Unlike the analogue instruments, these electronic devices need separately sold data acquisition cards in order to convert the analog data to digital (ADC) and to store data (data logging) in computers. This approach not only increased the overall equipment cost but also required special training of the staff, which takes a considerable amount of time to reach the level of expertise needed. Also, companies closed-platform policies make it hard to track the source of error, and therefore reduce the control of the researcher over their study.

The developments in microprocessor technology and the ever-growing open-source community has created several cost-effective low-end solutions for data acquisition purposes to address these problems. These platforms are open to use, affordable and allow to change the source-code if necessary. Although there are many open-platform cards available, the most popular cards are, in terms of quality of its open-source community, Arduino, RaspberryPi, and Beaglebone.

RaspberryPi and Beaglebone are mini-computers which have its CPU, GPU and memory. Unlike RaspberryPi and Beaglebone, Arduino is a micro-controller that is the cheapest option among them but has limited capabilities. These boards, with the support of a strong community behind, are the feasible solutions to satisfy the need of cost-effective cards for data acquisition purposes.

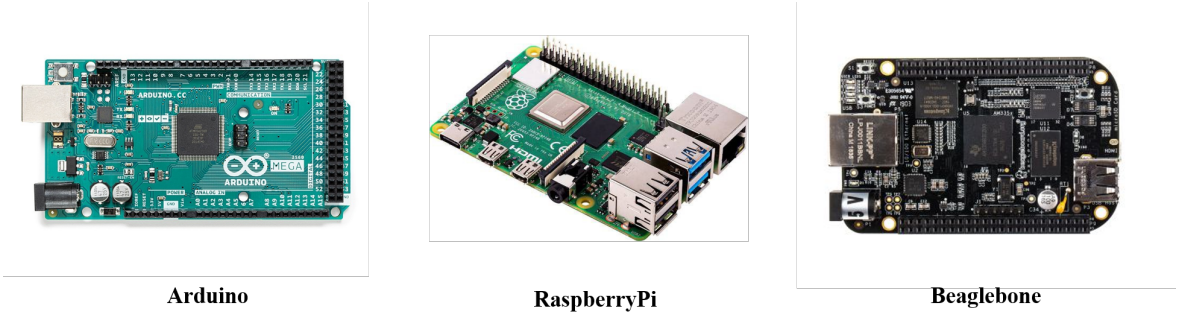

Figure 1.1. Some open-platform development boards. [1]

Selection of whether a complicated acquisition system with expensive sensors versus a simple but large number of sensors using open platforms may become a significant challenge for researchers. The use of costly sensors with a high-end data acquisition board may be seen as a reliable way to obtain measurements at a single point. However, taking measurements from a small number of points may not be enough to picture the overall response of the soil. Utilizing a large number of low-level sensors may be more advantageous for soils considering its heterogenetic nature. But, depending on the level of accuracy needed, it might be hard to obtain high-resolution data with low-level devices. One way of recovering from this problem could be the hybrid utilization of various level sensors.

An expensive high-end data acquisition card and a cost-effective low-end open-platform Arduino board have been compared. All tools have their advantages and disadvantages. Although the Arduino board offers overall control over the end-to-end process, the board's sampling rate capacity might not be suitable for some applications. While the high-end data acquisition card supports sampling at 16-bits up to 100 MHz, Arduino Mega 2560 board supports at 8-bits up to 20 MHz.

A 500 kPa capacity miniature stress transducer, connected to a high-end data acquisition board, enclosed in a silicone pacifier that is filled with de-aired and distilled water, was used to measure the stress within the soil. This transducer requires no physical contact to its pressure-sensing area in order to obtain reliable measurements. Therefore, the direct use of this sensor with soil particles is not possible. To overcome this problem, the sensor was enclosed in a regular silicone pacifier. Although the sensor has 500 kPa capacity, the load is applied up to 75 kPa. By considering the pressure exerted by a baby's teeth through the pacifier is more than 500 kPa; its conceived that the pacifier can accommodate stresses up to 75 kPa.

The prescaled sensitive films and IMUs were attached on the blocks of the segmental pile, and the pile was placed in a large-scale direct shear test box which was then filled with loose sand. The pile head was fixed and was allowed to displace up to 5 cm with a rate of 1 mm per minute. It was aimed that horizontal pressure applied on the segmental pile may be determined using stress films. In the second part of this study, low-cost inertial-measurement-units (IMUs), connected to a low-end data acquisition board, were used to estimate the displacement. The obtained inclination angles were used to estimate the displacement using MATLAB's sensor fusion algorithms, and then estimated values were compared with values obtained from external LVDT's.

This study demonstrated that sensitive stress films and IMUs has potential in geotechnical modelling applications to measure and visualize the stress distribution and to measure the displacement. The study will be presented in the following five chapters. The next chapter, Chapter 2, starts with the introduction of stress measurement methods and presents similar studies in the literature. In the second part of this chapter, IMUs are briefly explained, and the use of these sensors in geotechnical studies was presented. The detailed working principle and calibration process of IMUs are explained in Chapter 3. Test results are presented in Chapter 4 and are evaluated in Chapter 5. The conclusions drawn from this study are presented in Chapter 6.

2. LITERATURE REVIEW

The measurement of stress is an indispensable part of the engineering discipline. Especially in the geotechnical engineering, researchers in need of economical, reliable and easy to handle stress measurement solutions.

The prescaled films are used as the stress measurement method, and a pressure transducer is modified to operate under the soil. This study also explores the use of IMUs for the estimation of deflection in geotechnical applications.

2.1. Stress Measurement Techniques

2.1.1. Pressure Transducers

Pressure transducers are the devices that convert pressure into the electrical signal. Although the various type of pressure transducers available in the market, the most common and cost-effective type is the millivolt output transducers. To achieve reliable and robust measurements using these devices, its crucial to properly calibrate it and choose the device according to its purpose of use.

A 500 kPa pressure transducer is modified to operate under the soil. This transducer requires uniform pressure applied to the pressure-receiving surface for reliable measurements. Therefore, the applied pressure will be uneven, and the obtained data will fluctuate if the pressure-receiving area in-contact with soil particles.

Ramirez *et al.* [21] studied three different methods to calibrate pressure transducers. The first one is the deadweight method, in which a pressure transducer was placed on a flat surface, and the corresponding millivolt-per-volt values were recorded for different deadweights. Secondly, the pressure transducer was placed at the bottom of a plastic tube, and the tube was filled with wheat.

Different loads are applied to the top of the tube, and corresponding millivolt-per-volt values were recorded. As the third method, a steel air calibration chamber was designed and manufactured. The air pressure was supplied steadily by a compressor, and millivolt-per-volt values were recorded at different pressure values. The author concluded that the most effective calibration method was using the air calibration chamber because of the ability to continuously apply uniform pressure.

Labuz and Theroux [22] calibrated the pressure transducer in two methods, hydraulic oil and manufactured steel earth pressure cell (EPC). In the first method, the transducer was placed in oil, and corresponding electrical values were obtained for a set of pressure values. In the second method, they have placed the pressure transducer in the bottom of a steel cell and then filled the top of the sensing surface with soil. Also, a fluid chamber was placed on the top of the soil layer and the load was applied to the fluid chamber. They have performed a set of earth pressure tests after the calibration curves were obtained with each method. They concluded that the first method's pressure values are better than the second one due to the occurred arching phenomenon.

Chen and Randolph [23] focused on the calibration of transducers using triaxial and centrifuge tests. They have used a modified caisson for triaxial and centrifuge tests. The caisson was immersed in the water and corresponding electrical values were obtained at varying water pressures in the first triaxial test. At the second triaxial test, the caisson was embedded in kaolin clay and the sample were subjected to drained and undrained pressure changes at 1g. In the centrifuge tests, the pressure transducer was fixed at the bottom of the caisson and was tested in water and in consolidated clay samples while the centrifuge was spinning at 120g. They showed that the obtained values using a triaxial cell at 1g with kaolin clay (undrained) and using the centrifuge test at 120g in water have an average of 98% accuracy.

2.2. Stress Mapping Techniques

2.2.1. Tactile Pressure Sensors

Tactile pressure sensors are thin and flexible devices manufactured by Tekscan Inc. These sensors have several advantages over prescaled stress films by Fujifilm, such as reusability and continuous real-time monitoring. The film's surface is coated with an electrically conductive material in rows and columns and formed a matrix over the surface.

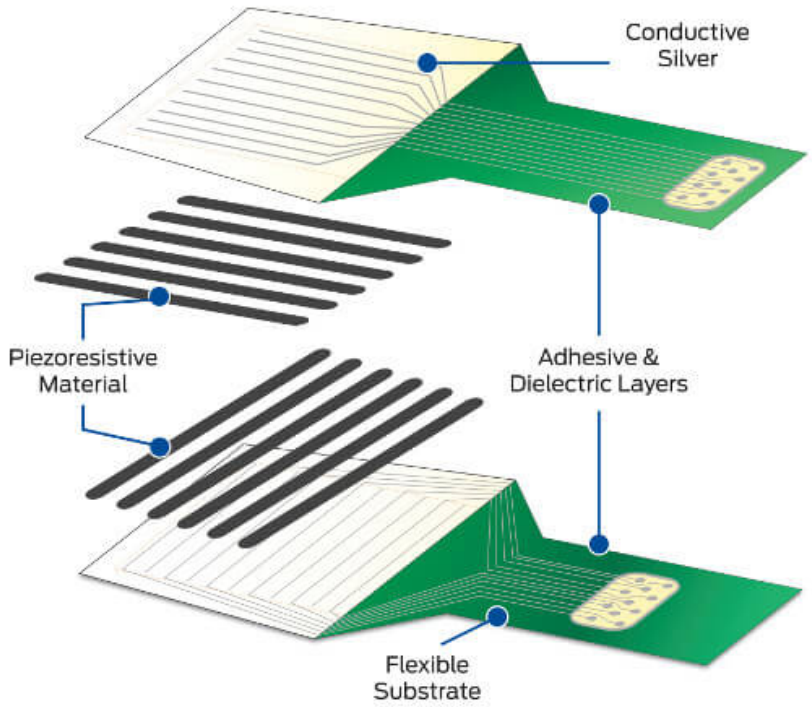

Figure 2.1. Tactile pressure sensors [2].

Paikowsky *et al.* [24] used tactile pressure sensors first-time to visualize and to measure the stress distribution under a rigid strip footing. They draw attention to the usability and accuracy ($\pm 10\%$) of these first-generation tactile pressure sensors.

After this, the author continued to explore usage areas in Paikowsky *et al.* [25] and has used tactile pressure sensors to monitor the effect of grain size on stress distribution and to measure the pressure under the sand heap.

O'Rourke *et al.* [3] studied pipeline systems' response to the ground rupture after an earthquake. They have performed centrifuge tests on pipes which made of high-density polyethylene (HDPE) and steel. The tactile pressure sensors were wrapped around the pipes and soil pressure distribution is obtained.

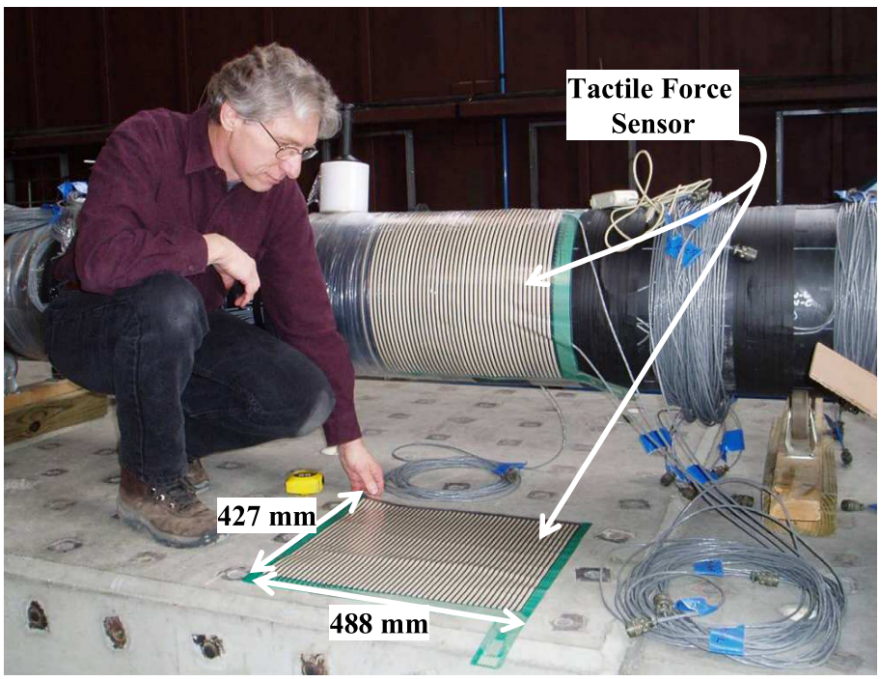

Figure 2.2. Tactile pressure sensors wrapped around the pipe; from O'Rourke *et al.* [3].

Ha *et al.* [26] also studied the response of buried high-density polyethylene (HDPE) during and after an earthquake however they mainly focused on the effects of location of these pipes such as crossing fault zones. As the latter study, tactile pressure sensors were wrapped around the HDPE pipe and measurements were taken. They also placed strain gauges along the pipe and combined the data from the strain gauge and tactile sensor to determine p — y relations of the pipe.

Gao *et al.* [27] explored the change of K_0 in dry sand under different loading conditions. They performed loading tests using oedometer and used tactile pressure sensors to monitor and to measure the horizontal stress changes and obtain K_0 values.

Kokkali *et al.* [28] studied the rocking response of a single degree of freedom (SDOF) system on the sand and conducted several centrifuge tests. Tactile pressure sensors were placed between the square foundation and the dry sand to capture vertical stress distribution and to determine the contact areas.

Zhang and Wang [4] aimed to monitor the change in stress and stiffness to explore the working mechanism of a driven pile in dry sand. They placed tactile pressure sensors in underlying dry soil that is placed in a custom-made pressurized chamber to simulate site conditions fully. They noted that unlike the other measurement techniques, thanks to the flexible nature of a tactile pressure sensor, the soil is not limited by an artificial boundary (shape of a rigid sensor) and soil arching is avoided.

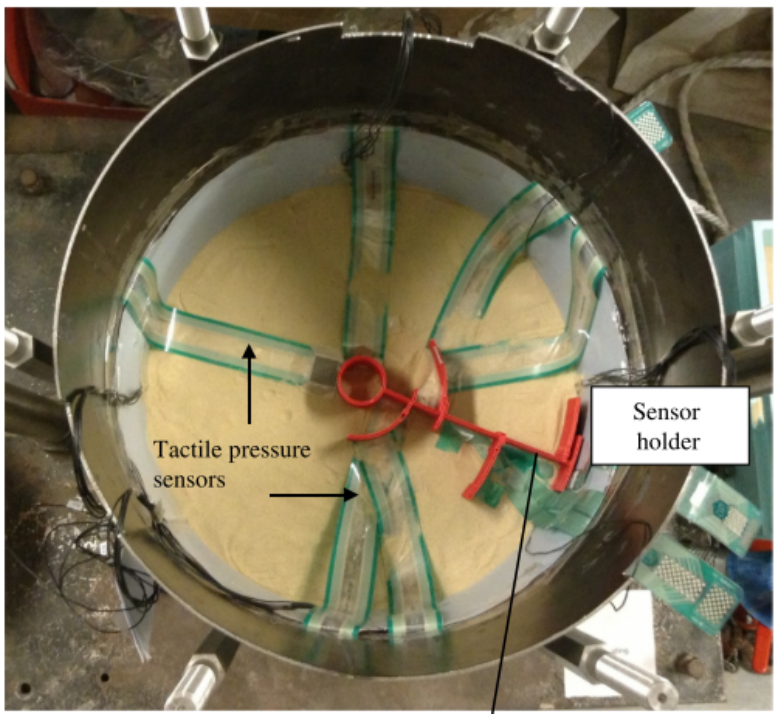

Figure 2.3. Placement of tactile pressure sensors; from Zhang and Wang [4].

El-Sekelly *et al.* [29] used tactile pressure sensors to measure the change in K_0 and aimed to find a link between K_0 and overconsolidation ratio (OCR) in Ottowa Sand under loading/unloading conditions. Also, the sample was subjected to strong shaking to achieve liquefaction conditions and using tactile pressure sensors, lateral earth pressure were measured before and after the shaking. The author observed a significant decrease in K_0 because of the extensive liquefaction.

Nicks *et al.* [30] investigated the lateral earth pressure behind the face of a modular block in mechanically stabilized earth walls (MSE). They used tactile pressure sensors and contact pressure cells and placed the sensors behind the face of the block of two different geosynthetic reinforced soils and obtained measurements. The author concluded that although the results obtained from tactile pressure sensors were not as robust as contact pressure cells, they have advantages over CPC and are very promising for the future.

2.2.2. Prescaled Stress Films

Prescaled films, also known as pressure papers are used to measure the stress distribution and the applied stress value. Prescaled films are offered in nine different ranges from 5 kPa to 300 MPa. The only difference between each product is the supported range and the film type. While some of them are mono-sheet type films, the majority of the product family is a two-sheet type film. Prescaled films are available in rolls and should be cut in needed sizes. Two-sheet type films require A-film and C-film for successful measurement. The A-film consists of a 75μ Polyethylene terephthalate layer and 15μ micro-encapsulated color-forming layer, while C film made of a 15μ color-developing layer. Both of the films are in whitish before the application. Before applying the stress, A and C film must be in contact with each other and should be placed in a thoroughly dry and flat surface. Once the stress is applied, the microcapsules in A-film start to break according to the applied stress value and release a chemical onto C-film's color-developing layer. The released chemical develops a magenta-like color on the C-film.

The intensity of this color has a direct relation with the applied stress, meaning that if the applied stress increases, the intensity of the magenta-color is also increasing.

The dedicated software offers several different options to analyze the films. The applied stress films can be visually analyzed by using the provided charts showing the sample color intensities and their corresponding stress value in different environmental conditions. The second option is the software developed by the manufacturer called FPD-8010E. This software requires a calibration paper which is separately sold. Before scanning the used prescaled film, this calibration paper should be scanned by the software, and then C-film can be scanned and be analyzed using this software. The C-film is scanned with a 200 dots-per-inch resolution, and the corresponding pressure can be measured for each point.

Prescaled films are used in many applications, from engineering to medical applications. Besides the other stress measuring methods (pressure transducers, etc.), it allows to detect each of the contact points even with a visual inspection.

In clinical research, Ralphs *et al.* [31] aimed to investigate the usefulness of prescaled films to determine the plantar pressure and diagnose for foot disorders. Also, Patterson *et al.* [32] searched for methods to measure the pressure between the human joints and investigated the use of prescaled stress films by concentrating on the effect of time and light exposure of the films. They applied different amounts of stresses and lights to prescaled films to determine whether it has a significant impact on the accuracy of measurements.

Sande and Backx [33, 34] used prescaled films to visualize and to measure the soil/tyre contact pressure. They placed prescaled films between the tyre and a metal plate within a tyre testing machine. Both of them conducted their own calibration experiments but followed the same matlab script to analyse the results.

Cirello *et al.* [35] aimed to discover the contact pressure distribution of an off-road tire. They used prescaled films to visualize and measure the stress distribution by placing the film between the tire and the ground. The range of 200 kPa to 500 kPa type (LLLW) film was used and was analyzed by a developed algorithm. This algorithm detects the color code of pixels within the scanned film and then matches these codes with the manufacturer's sample image and charts.

Watanabe *et al.* [5] studied the pressure distribution in sand under impulsive loading. The prescaled films were placed in the inner surface of an cyclindrical container that is filled with sand. The cyclindrical container was placed in a vertical powder gun and the specimen was subjected to impulsive loading.

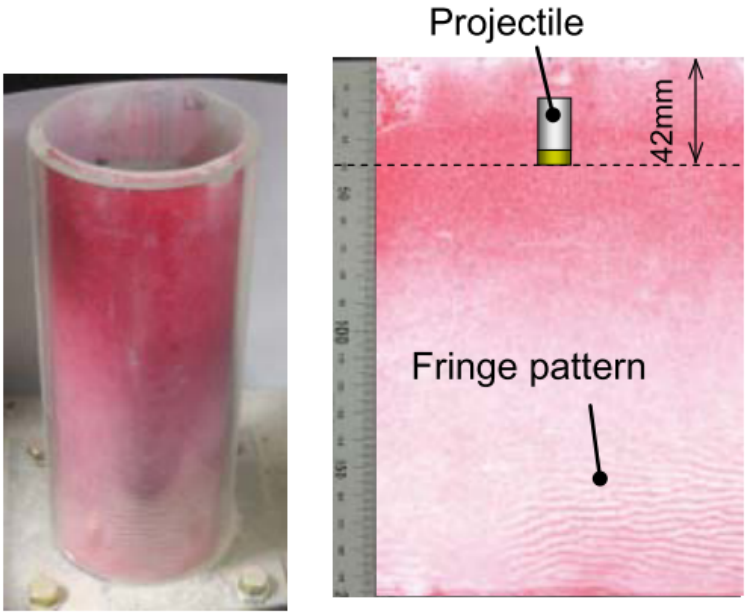

Figure 2.4. The pressure distribution after application; from Watanabe *et al.* [5].

Entacher *et al.* [6] aimed to measure the cutter force on tunnel boring machines (TBM). They used prescaled films to measure stress between casing and inserts, and based on that; they concluded that the irregular stress distribution they have observed was mainly a result of the asymmetric assembly.

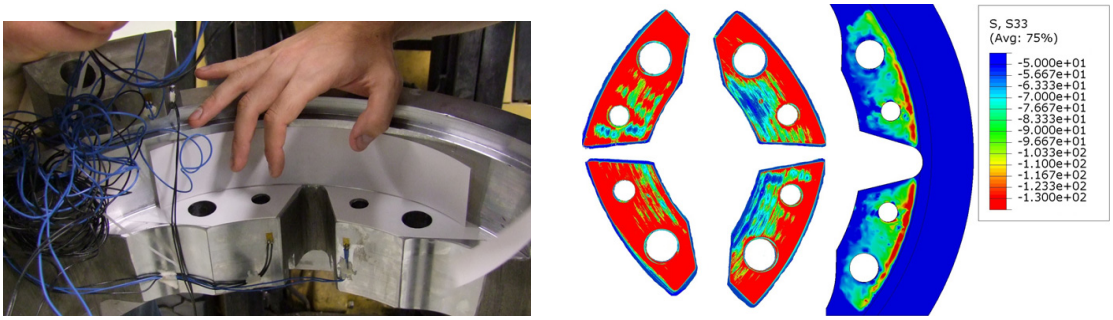

(a) Placement of films. (b) Results.

Figure 2.5. Placement and results of prescaled films; from Entacher *et al.* [6].

Li and Schindler [36] focused on the effects of the degree of compaction of soil on tire mobility. They developed two finite element tire models and conducted experiments to verify their measuremenets. In the experimental part of the study, a single tire with the same geometry and structure of the finite element model was tested by placing prescale films between the tire and a steel plate to measure the stress distribution. These results were compared with those obtained from the finite element model.

Baykal [37] examined three techniques for determining the soil-structure interface properties. One of these techniques is the use of prescaled films in geotechnical applications. The researcher placed prescaled films to obtain the stress distribution between two 50 mm x 50 mm x 20 mm concrete mortar blocks and analyzed the films using the dedicated software. This study concluded that prescaled film technology is suitable for most of the geotechnical applications; however, concrete-like such rough surfaces require in-depth calibration of the stress films since the stress concentrations may result in out-of-range measurements. The films performed best at the average stress level of the range of the film.

Jiang and Shu [38] proposed a probabilistic method to examine the randomness of the contact force and areas between geomembrane and granular material. The proposed method showed that the force is exponentially distributed, and the main factor affecting this distribution is the grain size. To verify this method's outcome, several laboratory experiments were conducted using glass beads and cobbles as granular materials.

They acquired the distribution of forces using the prescaled films and analyzed the scanned film using Matlab by comparing the values with the color densities provided with the product manual.

Yahia [19] under (BAP-11A04D9) research fund conducted an experimental study regarding the behavior of segmental pile with variable flexural rigidity. The researcher employed prescaled films to obtain stress distribution and average stress values. The prescaled films placed between 50 mm x 50 mm x 20 mm concrete mortar blocks. Using the obtained stress values, the moment along the pile is backcalculated.

Giwelli *et al.* [7] focused on to understand the shear behavior of artificial tensile fracture, made from Inada granite, at different sizes and shear displacements. To measure the fracture surface area after shearing, they used prescaled films. To determine the contact areas, a method proposed by Nemoto *et al.* [39] were used. The films were scanned at a 1500-dpi resolution and were converted into the gray-scale image and pixels were filtered according to a specific threshold of brightness.

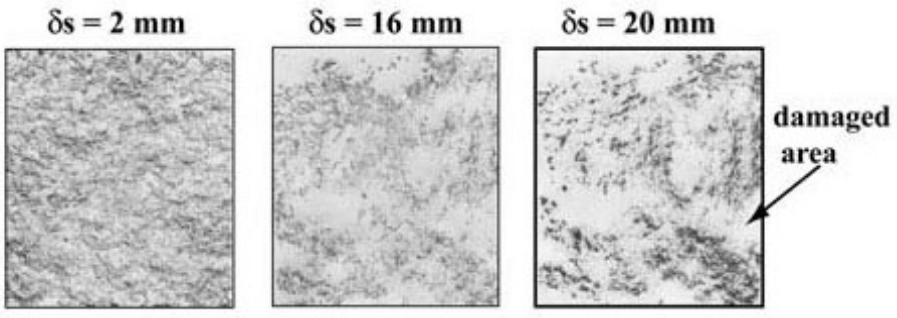

Figure 2.6. Grayscale films showing contact areas; from Giwelli *et al.* [7].

Abadi *et al.* [40] used prescale films to explore the contact areas of the sleeper to ballast particles in railway tracks. They placed stress films in different combinations of locations to understand the contact points, and based on this data, they have proposed several ways to increase the area of contact for the sleeper to ballast interface.

Tabar *et al.* [8] studied the stress distribution within the landfills. They used prescaled films to measure the stress concentration on HDPE (High-Density Polyethylene) pipes by wrapping the film around the pipe. After each application, they removed the pipe to analyze and to replace the stress films. They used charts provided by the manufacturer to estimate the stress applied.

Figure 2.7. Prescaled films wrapped around hdpe pipes; from Tabar *et al.* [8].

Sengez [20] under (BAP-18A04P2) research fund conducted an experimental study regarding the behavior of segmental pile with variable flexural rigidity. Prescaled stress films were placed between the concrete mortar blocks and average stress applied on the pile was determined. The author used the obtained pressure values to determine the moment capacity of the segmental pile.

2.3. IMU Sensors

The inertial motion measurement unit (IMU) is a chipset that consists of many sensors such as but not necessarily magnetometer, accelerometer, and gyroscope. Some IMUs available in the market include temperature and humidity sensors as well. They are used in a wide range of sectors (from medical to astronomy) because they provide cheap and robust measurements. Also, IMUs are small and energy-efficient solutions, and their compatibility with programmable boards such as Arduino and Raspberry Pi makes them unique and highly customizable solutions to the many problems in the various sectors.

Table 2.1. Overall look to studies about prescaled films.

Ref.	**Placement**	**Purpose**	**Analyze Software**
[33, 34]	between tyre and a metal plate	to measure pressure in soil/tyre contact areas	MATLAB
[35]	between tyre and the ground	to measure pressure in soil/ground contact areas	MATLAB
[5]	inner surface of cyclindrical container	to measure pressure in sand under impulsive loading	MATLAB
[6]	between casing and inserts	to measure the cutter force on TBMs	MATLAB

Table 2.1. Overall look to studies about prescaled films (cont.).

Ref.	**Placement**	**Purpose**	**Analyze Software**
[36]	between tyre and a steel plate	effects of degree of compaction of soil on tire mobility	N/A
[37]	between concrete mortar blocks	to assess the usability of this tool for geotechnical applications	FPD-8010E
[38]	b/w geomembrane & granular material	to examine randomness of the contact force	MATLAB
[19]	between concrete mortar blocks	to backcalculate the moment along the pile	FPD-8010E
[7]	within artificial tensile fracture	to measure the fracture surface area after shearing	MATLAB
[8]	wrapped around HDPE pipes	to understand stress distribution within the landfills	FPD-8010E

This chip consists of a 3-axis accelerometer, a 3-axis magnetometer, and a 3-axis gyroscope. In simple terms, an accelerometer gives an idea about the rate of change in velocity while a magnetometer tells the amount of magnetic force deployed on the body. In addition to these sensors, angular velocity measurements can be taken thanks to the gyroscope sensor. Data from an individual sensor may not be enough to describe the whole picture; therefore, using the entire data from above mentioned three sensors are processed with sensor fusion algorithms.

Kim [41] designed a wireless sensor network to solve the problem of early and accurate detection of landslides. They placed IMUs on an artificial slope in the laboratory under constant rainfall. Their study verified the fact that the ground motion has a direct relation with the change in acceleration and the change in inclination angle.

Giri *et al.* [42] proposed a wireless sensor network that consists of multiple IMUs, continuously recording data from the accelerometer, gyroscope, and magnetometer then transmits to the central computer wirelessly for analysis. Experiments were conducted in the laboratory and communication with sensors provided by Bluetooth 4.0 technology. The accelerometer was calibrated by performing a controlled-fall-experiment, basically, an IMU, let free fall from a known distance, then the recorded accelerometer data on the relative axis was compared and verified with the gravity. Also, the gyroscope was calibrated in a similar manner, an IMU was placed on a flat plaque and rotated 30, 45, 60, and 90 degrees to determine the offset to calibrate the sensor. They concluded that the data obtained from IMUs are repeatable, be able to assess the type of slope failure, and it could be useful for early warning systems.

Giri *et al.* [9] used IMUs for landslide movement detection and drew attention to the point that only considering the amount of tilt is not a reliable solution to detect possible landslide since a clear slope might not occur in slow-moving translational slides. They proposed two methods that help to define threshold values and criteria to identify translational slides using the data obtained from a 3-axis accelerometer and a 3-axis gyroscope.

The study showed that by monitoring the noise of sensors, the movement could be detected except if it's not moving in a slow-rate. Also, they concluded that the change in linear acceleration was the essential data to indicate slow-moving translational slides.

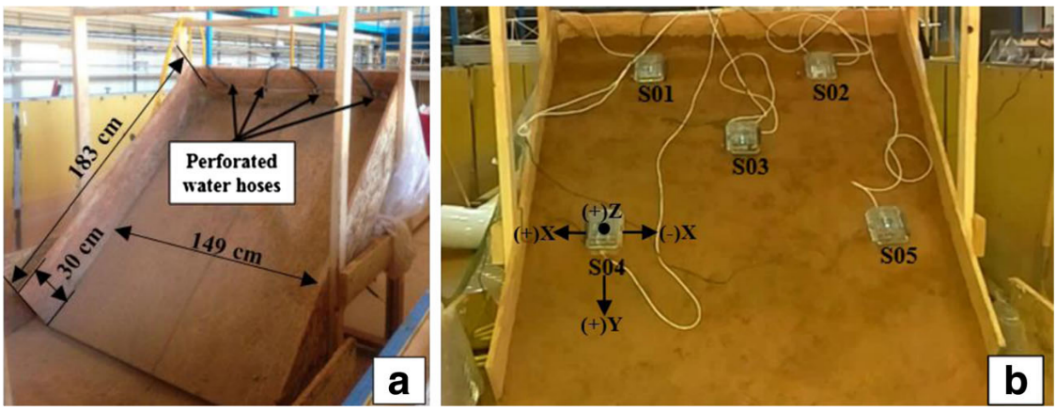

Figure 2.8. Use of IMUs in laboratory experiments; from Giri *et al.* [9].

Weerasinghe *et al.* [43] proposed a method using IMUs to detect the direction and record amount of soil movement real-time to predict the hazard of a possible landslide. They placed equidistance recording stations and put IMUs under the soil. The data recorded by these units were transmitted to a server wirelessly, and then the collected data were analyzed. The amount of movement calculation based solely on the accelerometer was acquired by integrating the accelerometer data to obtain velocity and then integrating again to get the distance in all three axes (x, y, and z). Although the raw data acquired by the accelerometer is filtered by a high pass filter and then a complementary filter in their strategy, the double integration approach accumulates error hence decreases the reliability of the results.

Park *et al.* [44] also used IMUs to determine the angle of internal friction and predict the soil movement. Sensors are placed in a soil box that is able to rotate around to simulate a real slope failure. During the experiments, motion data from the accelerometer and gyroscope were collected and were backsolved to obtain the angle of repose. Also, the same model analyzed on Abaqus. Using the data from numerical analysis and IMU, the angle of friction was determined.

3. METHODOLOGY

Two different stress measurement and IMU-based deflection measurement techniques are investigated.

There are several different types of stress measurement methods available in the literature, as summarized in Chapter 2. Most of these methods require expertise and the availability of costly instruments in the laboratory. To address this problem a wide range of approaches were implemented; a classical high-end data acquisition board connected to miniature stress transducers to measure the stresses in the soil; sensitive films and a dedicated software to measure soil-structure contact stress; Arduino based economic IMU sensors for measuring inclination to calculate corresponding displacements and finally a classical LVDT for verification of calculated displacements.

Additionally, a type of pile called segmental pile with variable flexural rigidity, developed in Bogazici University, was used with low-end IMU sensors that is connected to an low-end data acquisition board.

In this chapter, the metholodolgy of this study is presented in following five main titles.

- Materials
- Segmental Pile
- IMU Sensors
- Prescaled Stress Films
- Transducers

3.1. Materials

3.1.1. Natural Sand

In order to classify the soil and determine the engineering properties such as maximum and minimum void ratio, sieve analysis, and relative density experiments were performed. The grain size distribution of the natural sand is shown in Figure 3.1.

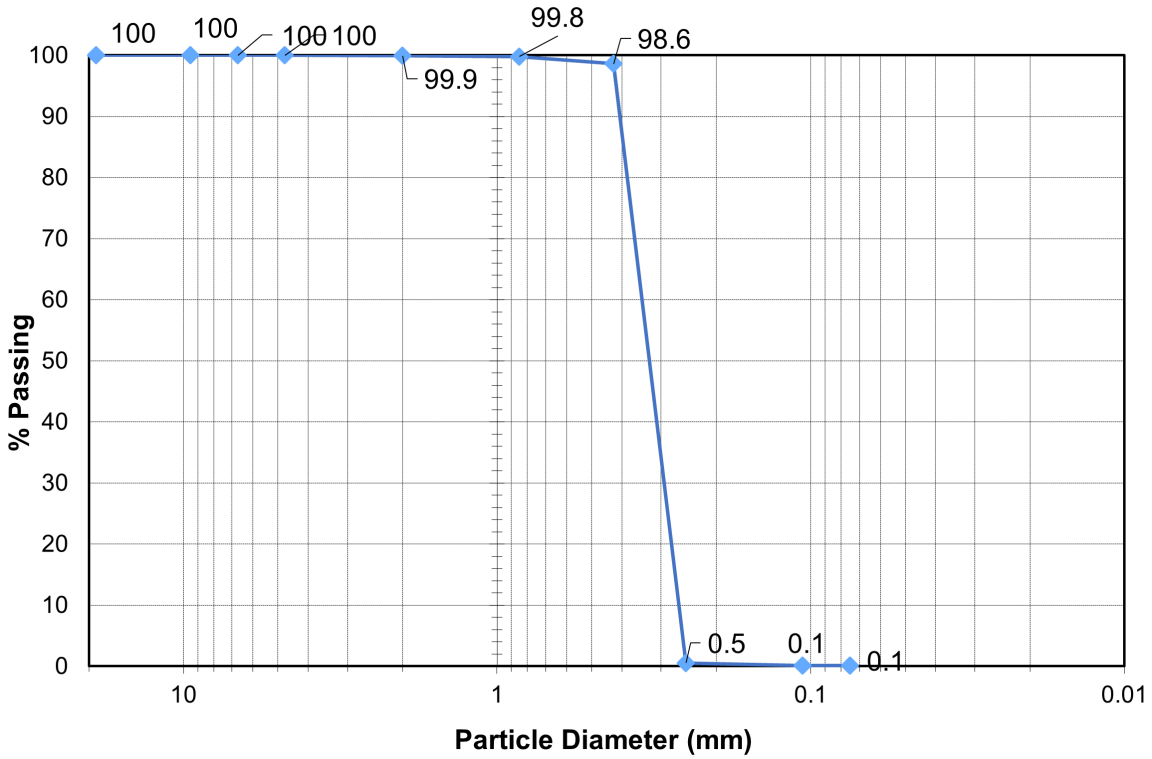

Figure 3.1. The grain size distribution of natural sand.

The specific gravity, minimum and maximum void ratios, coefficient of curvature, coefficient of uniformity, and unit weight of the sand are presented in Table 3.1. According to ASTM D2487, this soil is classified as poorly graded sand in the Unified Soil Classification System (USCS). In all the experiments, the same natural sand is used.

Table 3.1. Engineering properties of natural sand.

G_s	γ (kN/m^3)	C_c	C_u	e_{max}	e_{min}	ϕ_{loose}
2.63	15.6	1.15	1.22	0.68	0.47	30

3.2. Segmental Pile

The segmental pile with variable flexural rigidity is a type of pile proposed by Prof. Baykal, consists of 50 mm x 50 mm x 20 mm concrete blocks and 50 mm x 50 mm x 3 mm rubber membrane between them with an anchor cable passing through each element. The main advantage of this pile is the ability to control the overall rigidity by merely adjusting the tension of the anchor cable.

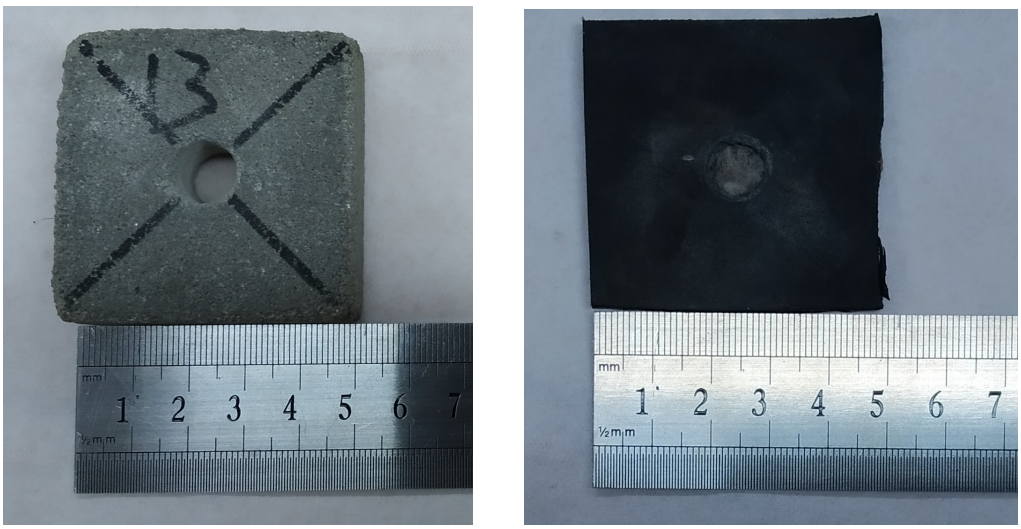

(a) 50 x 50 x 20 mm concrete block (b) 50 x 50 x 3 mm rubber membrane

Figure 3.2. Concrete mortar block and rubber membrane.

The concrete mortar blocks from the previous study of [20], are used to form the modal pile. According to the ASTM C270 standard, the blocks were prepared using Portland Cement I with a ratio of 1:0.5:3 (cement:water:sand). The rubber membrane, known as rubber 60 shore, is an industrial elastic rubber material widely used in the industry. The material properties of the rubber are presented in Table 3.2.

Table 3.2. The material properties of shore 60 rubber membrane. [19].

Rubber Type	Neoprene Rubber 1
General Description	Soft rubber
Style	7797
Color	Black
Tensile Strength (kN/m^2)	$10x10^3$
Elongation at Failure (%)	125
Elastic Modulus (MPa)	3
Thickness (t) (mm)	3-20
Rubber Shore (A)	60

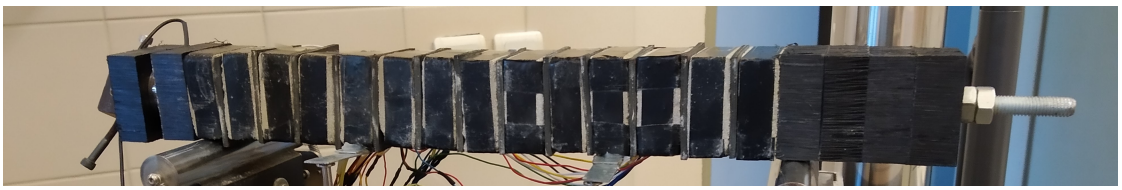

Figure 3.3. Overall look of the segmental pile.

3.3. Prescaled Stress Films

Prescaled stress films were used to measure the stress during the experiments. Prescale films measures the value of the pressure by tracking the change in different magenta intensities. As indicated in Table 3.3, prescaled films offered in nine different pressure ranges and are commercially available in the market.

Table 3.3. Types of prescaled films.

#	**Product Name (Code)**	**Pressure Range (MPa)**	**Type**
1	Ultra Extreme Low Pressure (5LW)	0.005 - 0.05	Two-sheet
2	Extreme Low Pressure (4LW)	0.05 - 0.20	Two-sheet
3	Ultra Super Low Pressure (LLLW)	0.20 - 0.50	Two-sheet
4	Super Low Pressure (LLW)	0.50 - 2.50	Two-sheet
5	Low Pressure (LW)	2.50 - 10.00	Two-sheet
6	Medium Pressure (MW)	10.00 - 50.00	Two-sheet
7	Medium Pressure (MS)	10.00 - 50.00	Mono-sheet
8	High Pressure (HS)	50.00 - 130.00	Mono-sheet
9	Super High Pressure (HHS)	130.00 - 300.00	Mono-sheet

In the two-sheet type films, measurement requires two separate films called A, and C. A-film coated with a layer of micro-encapsulated colour-forming material while C-film laminated with a layer of colour-developing material. The working principle of prescaled films are similar to litmus papers. Once stress applied, the colour developing material in the micro-capsule released to the colour generating layer then forms a magenta-like colour on C-film. The density of this magenta-like colour depends on the stress applied, temperature, and humidity of the room. Therefore, it is essential to prepare the prescale films before use and allow a reasonable amount of time to adapt itself to environmental conditions fully.

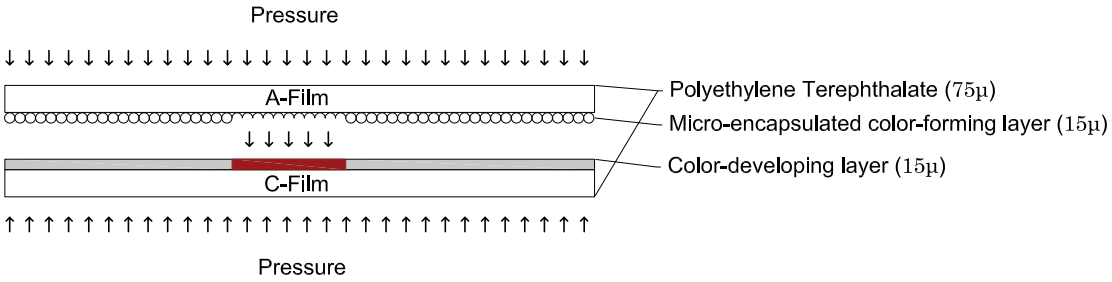

Figure 3.4. Closer look at two-sheet type films [10].

Prescaled films, designed to operate under 10 MPa stresses, require two sheets (A-film and C-film). They should be cut in the same size and placed with care to avoid parasitic measurements. Both of the films have shiny and dull sides. The sheets must be placed on a dry, clean, and a flat surface and only dull sides should be in contact with each other. All the films used classified as continuous pressure type films, implying that the pressure should be applied at least two minutes continuously to acquire a reliable measurement. When the experiment completed, the overlapped films should be removed with extreme care. They must be scanned at least 30 minutes later to be sure that the colour-developing chemical reaction wholly finished and the final colour density is reached. To determine the recorded pressure, C-film should be scanned with a scanner that supports 200 dpi resolution as it's recommended by the manufacturer. It is recommended that films should be analyzed the dedicated software provided by the producer. Alternatively, the following chart can be used to inspect and determine a pressure value visually.

3.4. IMU Sensors

IMU (Inertial Measurement Unit) is an electronic device used to calculate the motion, rotation, and velocity acting on the body. In general, an IMU consist of magnetometer, accelerometer, and gyroscope.

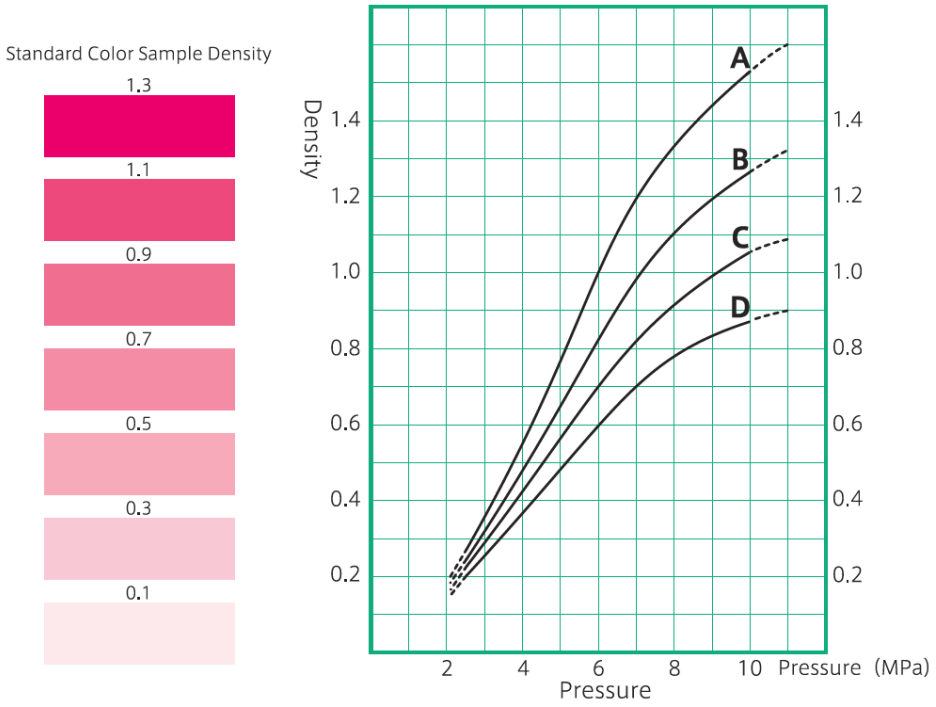

Figure 3.5. Pressure chart for continuous type films [10].

Magnetometers are used to measure the amount of magnetic force exerting on the body in 3-axis (x,y, and z). This operation is based on the earth's magnetic field model, which assumes a big magnet placed in the center of the earth and flux lines go through from south pole to north pole, as illustrated in Figure 3.6. A magnetometer can measure the magnetic flux density of its surrounding environment, and due the proportionality, magnetic flux density can be used to calculate strength and direction of magnetic field.

There are two different types of magnetometers as scalar and vector magnetometers. While scalar magnetometers measure the total strength of the magnetic field that is subjected to the body, vector magnetometers measure the component of magnetic density in a particular direction. [45] A vector magnetometer following the Hall-Effect principle is used.

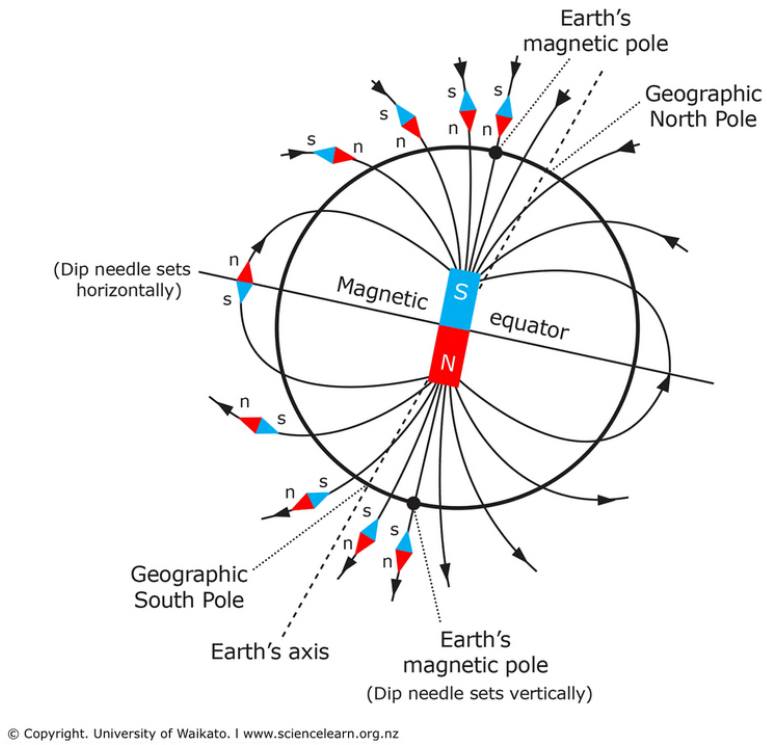

Figure 3.6. Representation of earth's magnetic field. [11]

The Hall-Effect named after Edwin Hall, who discovered to create a measurable voltage by using the magnetic field in the late 19th century. The Hall-Effect principle is based on the Lorentz force. It is known that electrons form a straight line on a semiconducting plate, and their movement on this path will create a magnetic field. If this semiconducting plate would placed between the poles of a permanent magnet, the magnetic field of the plate and the magnet will interact with each other and, due to Lorentz force, make electrons deviate from their straight path, as shown in Figure 3.7. Because of the Lorentz force, one side of the plate will have more electrons than the other side, and this will create the voltage difference between the sides of the plate.

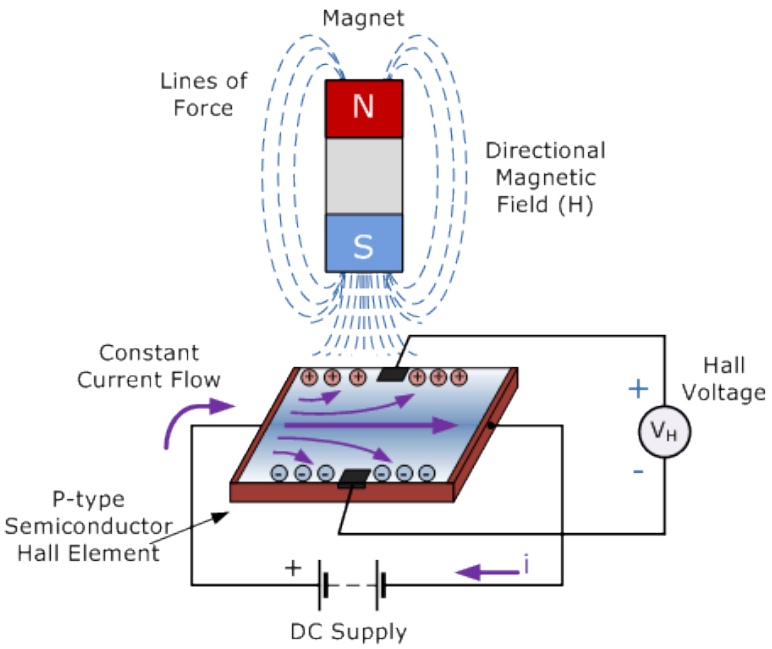

Figure 3.7. The working principle of hall-effect magnetometers [12].

Further, accelerometers are one of the main parts of an IMU sensor. Accelerometers are the devices that measure the rate of change of velocity of the body. In simple terms, the measurement of acceleration based on Newton's second law of motion ($F = m \times a$). The type of accelerometer used in the study also follows the Hall-Effect principle described above.

The most of the IMU sensors also include gyroscopes chips inside. Gyros are cheap sensors that measure the angular velocity (radian-per-second). Consider a mass is moving in a particular direction with a particular velocity. If an external angular rate applied to the body, it will be displaced in the perpendicular direction due to Coriolis force and causes a difference in capacitance. The change in capacitance leads to the angular velocity of the sensing direction.

MPU-9250 chip-set produced by Invensense is used with the Arduino board. MPU-9250 includes a 3-axis magnetometer, a 3-axis accelerometer, and a 3-axis gyroscope inside. The combination of these sensors allows measurements in 9 DoF (degree-of-freedom). The used chip-set is shown in Figure 3.8 and its pin-out description in Table 3.4.

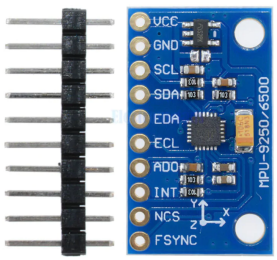

Figure 3.8. The mpu-9250 chip-set. [13]

An MPU-9250 sensor attached to each concrete block on a segmental pile and a total of 14 sensors were controlled by the Arduino Mega 2560 board. Each sensor occupies one SCL and one SDA port; however, the Arduino Mega 2560 board offers only one SDA/SCL port. By using TCA9548A multiplexer, this may be increased up to eight SDA/SCL ports. Both MPU-9250 and TCA9548A chips support I^2C protocol, meaning that each MPU-9250 sensor may be forced to use different factory-defined addresses (b1101000 and b1101001 in this case). Hence, one available TCA9548A port can be used with two MPU-9250 sensors, which have different addresses with each other.

Table 3.4. The pin-out description of mpu-9250 chip-set.

PIN Name	**Pin Description**
VCC	Power supply (voltage)
GND	Ground connection
SCL	I^2C serial clock
SDA	I^2C serial data
EDA	Unused, reserved line.
ECL	Unused, reserved line.
AD0	I^2C slave adress
INT	Interrupt digital output
NCS	Unused, not internally connected
FSYNC	Unused, connected to ground line

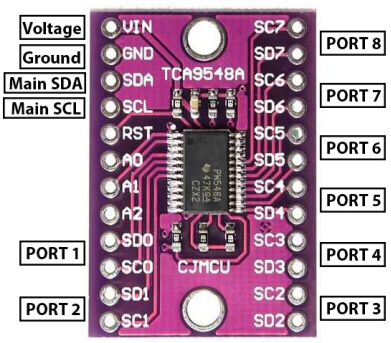

Figure 3.9. TCA9548A multiplexer. [14]

To force the MPU-9250 sensor to use either b1101000 or b1101001 address, the AD0 pin should be used. If the AD0 pin set high (connected to voltage line), the MPU-9250 sensor will communicate through b1101001 or AD0 pin set low (connected to the ground line) sensor will communicate through b1101000 address. Therefore, each port on the multiplexer was occupied by two sensors. While the first sensor's AD0 pin was connected to the voltage line, the second sensor's pin was connected to the ground line.

As with any digital instrument, measurements were taken using the IMU sensor are also error-prone. To reduce the noise in signals and to fuse the magnetometer, accelerometer, and gyroscope data, an algorithm needed. There are several filters available in the literature, such as the Ecompass algorithm, IMU Filter, Complementary Filter, and AHRS (Attitude-Heading-Reference-System) Filter. Each of these methods uses a different combination of parameters to estimate the orientation of the body, as seen in Table 3.5.

Table 3.5. Algorithms/filters for estimating orientation of the body.

Name	**Required Parameters**
Ecompass Algorithm	Magnetometer and Accelerometer
IMU Filter	Accelerometer and Gyroscope
Complementary Filter	Magnetometer, Accelerometer and Gyroscope
AHRS Filter	Magnetometer, Accelerometer and Gyroscope

Since the IMU sensor allows measurement from magnetometer, accelerometer, and gyroscope, the AHRS filter is used to filter the noise and to estimate the orientation and the position of the body. While complementary filter also uses all three sensor data, Kalman based AHRS filter is preferred for more reliable results.

With AHRS Filter, the magnetometer (μT), accelerometer (m/s^2), and gyroscope (rad/s) data can be used to estimate the Euler angles, thus the orientation of the body.

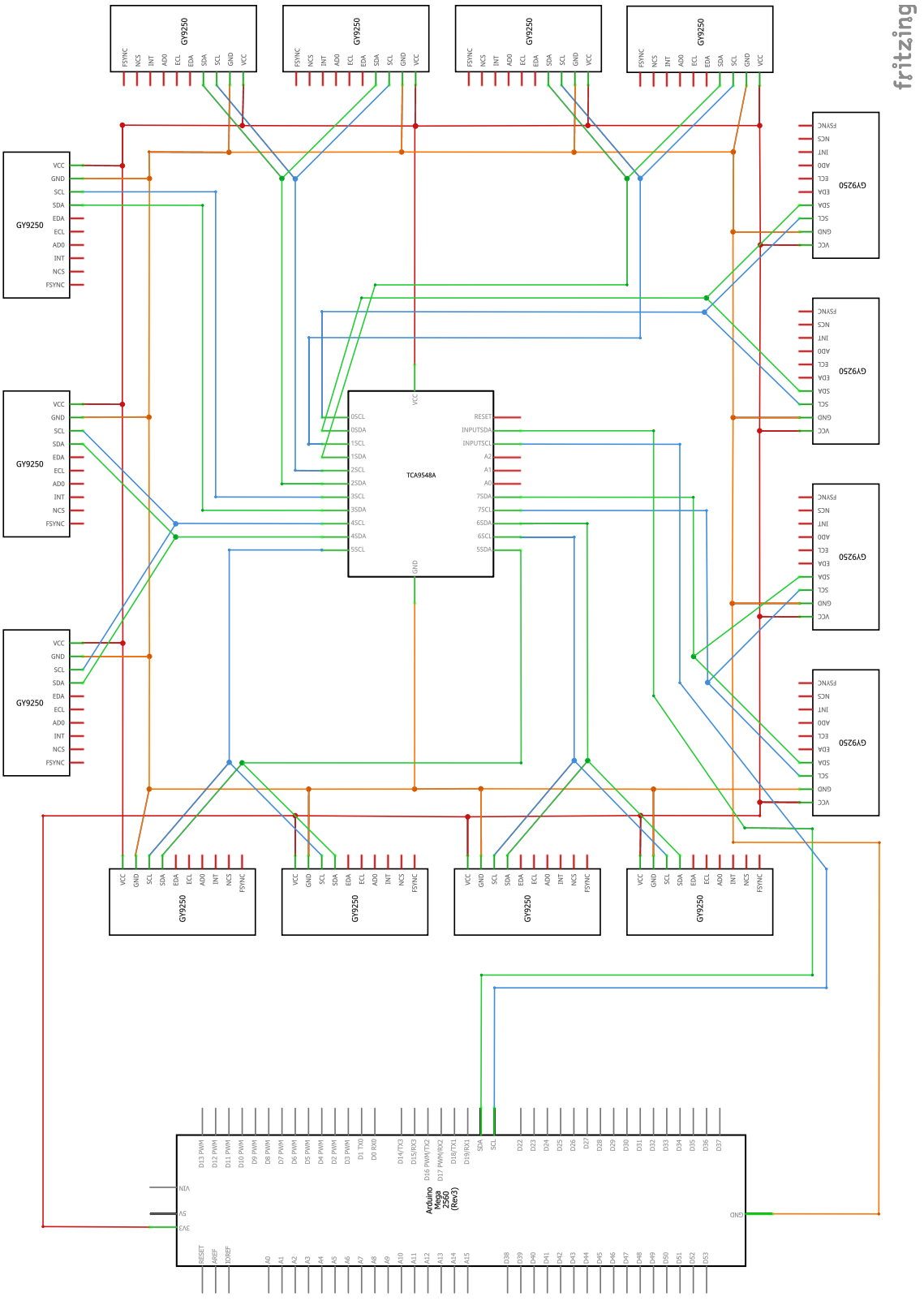

Figure 3.10. The circuit drawing.

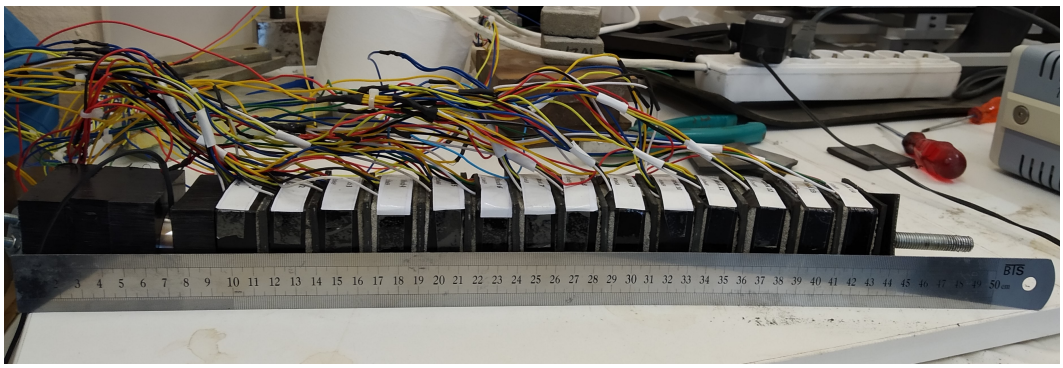

Figure 3.11. The segmental pile with mpu-9250 sensors.

Euler angles, introduced by Leonhard Euler, describes the general rotation of a body by three main coordinates. These coordinates are called Euler angles, as illustrated in Figure 3.12.

Before calculating the degree of rotation, the quaternion or rotation matrix should be constructed. The calibrated magnetometer, accelerometer, and gyroscope data passed into ahrsfilter() function, the built-in function of MATLAB, and the quaternion vectors obtained. This function takes a 3-by-3 magnetometer, 3-by-3 accelerometer, and 3-by-3 gyroscope data as input and returns a vector of quaternions. The overview of the algorithm of ahrsfilter() function is shown in Figure 3.13. Obtained quaternion vectors can be converted to Euler angles by using MATLAB's eulerd() function or Equation 3.1.

Table 3.6. Euler angles.

Axis of Rotation	**Euler Angle**	**Symbol**
x	Roll	ϕ
y	Pitch	θ
z	Yaw	ψ

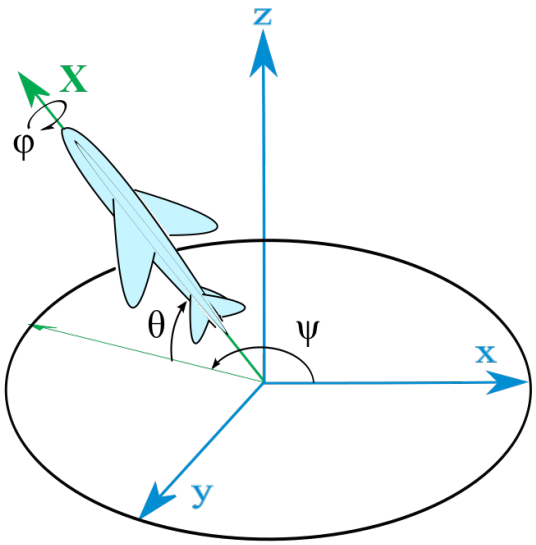

Figure 3.12. Euler angles. [15]

$$\begin{bmatrix} \phi \\ \theta \\ \psi \end{bmatrix} = \begin{bmatrix} atan2(2(q_0q_1 + q_2q_3), 1 - 2(q_1^2 + q_2^2))) \\ asin(2(q_0q_2 - q_3q_1)) \\ atan2(2(q_0q_3 + q_1q_2), 1 - 2(q_2^2 + q_3^2)) \end{bmatrix} \tag{3.1}$$

3.4.1. Calibration of Magnetometer

The magnetometers should be calibrated before using and on a regular basis. The existence of ferromagnetic materials such as iron, nickel, and cobalt close to magnetometers may cause incorrect measurements. The dipoles of ferromagnetic materials align with each other in response to the external magnetic field and become magnetized. Therefore, a magnetometer should be calibrated on its final position on the object and the environment to avert mismeasurements.

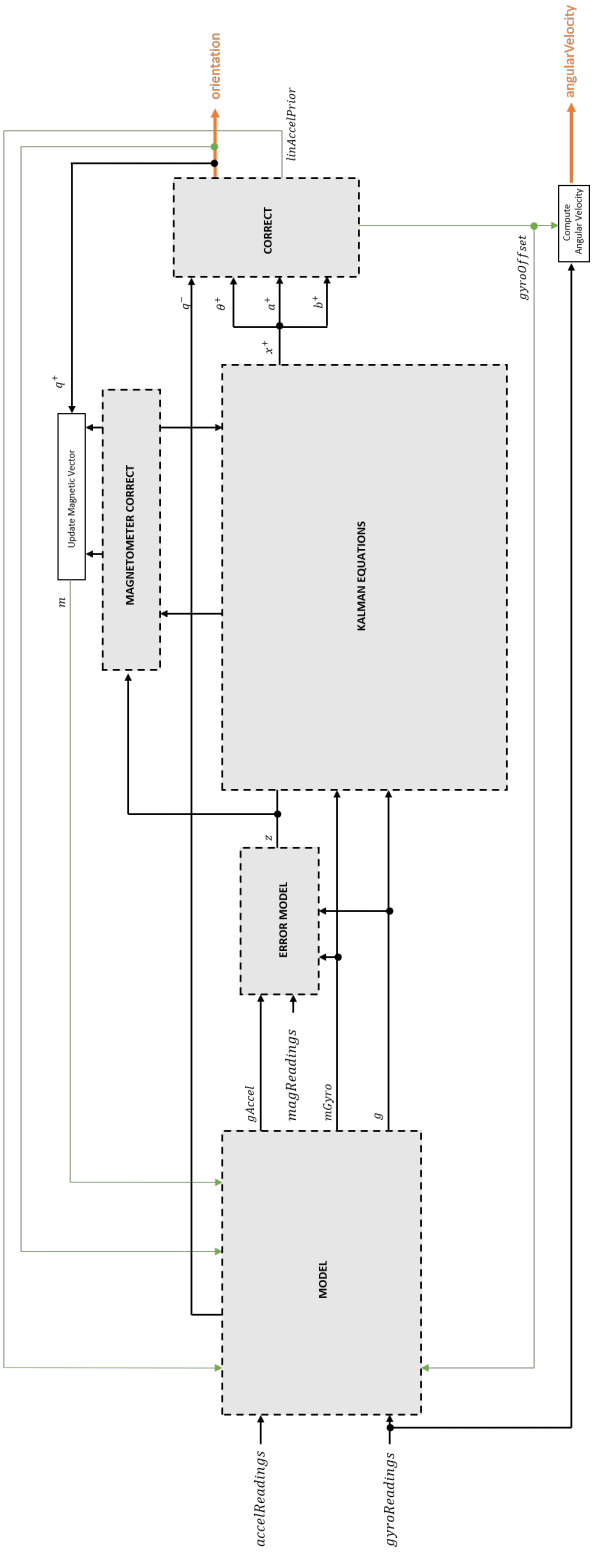

Figure 3.13. The overview of ahrs filter algorithm. [16]

The measurements from an ideal magnetometer should form a perfect sphere centered in origin in order to achieve reliable results. However, due to ferromagnetic materials, the shape or the center of expected sphere distorts. This distortion mainly caused because of hard-iron and soft-iron effects, as shown in 3.14. While the soft-iron effect describes the distortion in the shape of the expected sphere, the hard-iron effect describes the divergence from the origin.

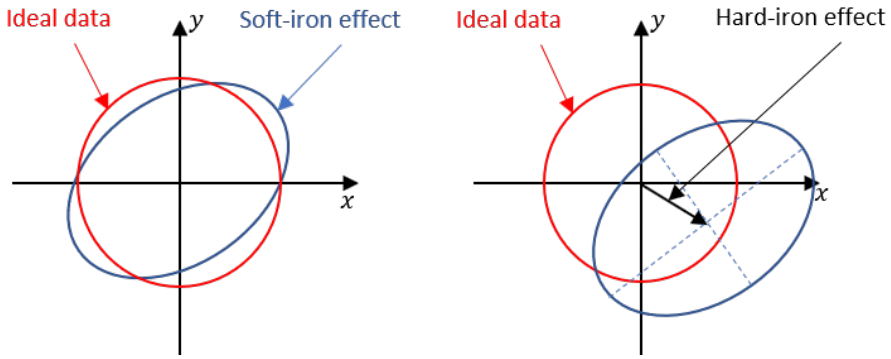

Figure 3.14. The hard-iron and soft-iron effects. [16]

A simple self-made cube was used to calibrate magnetometers. Each IMU sensor was placed on the center of the cube and rotated freely by hand while taking measurements to obtain as much as different x, y, and z points. It is essential to acquire unique data from x, y, and z points because these coordinates will be used to define the boundaries and domain of the sphere.

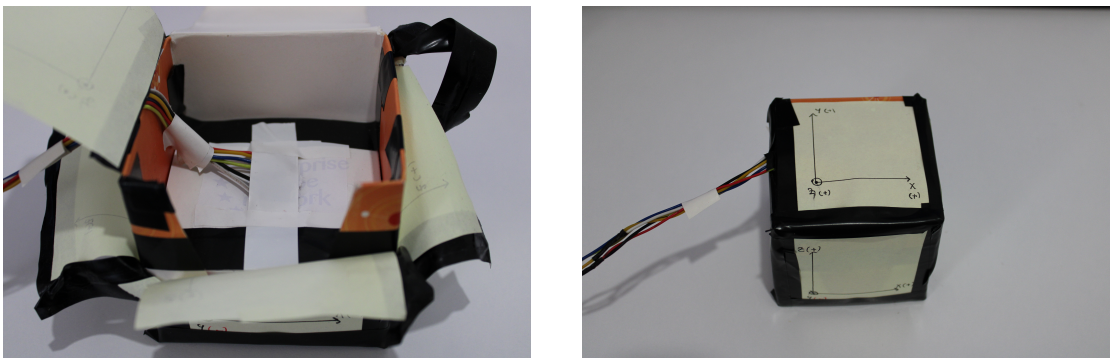

(a) inside (b) outside

Figure 3.15. The inside and outside view of calibration cube.

After obtaining approximately two thousand x, y, and z data, the raw x, y, and z values were filtered to elude conjugate coordinates and obtained entirely unique raw coordinates. These coordinates fitted into a perfect sphere by using the magcal() function of MATLAB. The magcal() function receives N-by-3 raw magnetometer data as input and returns 3-by-3 soft-iron effect correction matrix (transformation matrix) and 3-by-1 hard-iron correction vector (bias matrix). Each IMU sensor has slightly different soft-iron and hard-iron correction matrices. Nevertheless, these correction matrices should be applied separately. The calibrated magnetometer x, y, and z may be computed using Equation 3.2.

$$\begin{bmatrix} X_c \\ Y_c \\ Z_c \end{bmatrix} = \begin{bmatrix} M_{11} & M_{12} & M_{13} \\ M_{21} & M_{22} & M_{23} \\ M_{31} & M_{32} & M_{33} \end{bmatrix} \times \left(\begin{bmatrix} X_r \\ Y_r \\ Z_r \end{bmatrix} - \begin{bmatrix} B_x \\ B_y \\ B_z \end{bmatrix} \right) \tag{3.2}$$

The verification of the calibration can be performed by plotting the calibrated points and inspecting the shape and the origin of the sphere. A representative uncalibrated and calibrated data plot is shown in Figure 3.16.

3.4.2. Calibration of Accelerometer

For applications requiring precise measurements accelerometer should be calibrated. The self-made cube, mentioned above, used to calibrate accelerometers. Before going into the accelerometer calibration procedure, attention should be drawn to the local-axis system of MPU-9250 chipset. MPU-9250 chipset has different axis systems for magnetometer, accelerometer and gyroscope. While z-axis of magnetometer downward when the chipset placed on a flat surface, for accelerometer and gyroscope, z-axis is points upward and x-axis and y-axis are interchanged. The axis-system may be observed in Figure 3.17.

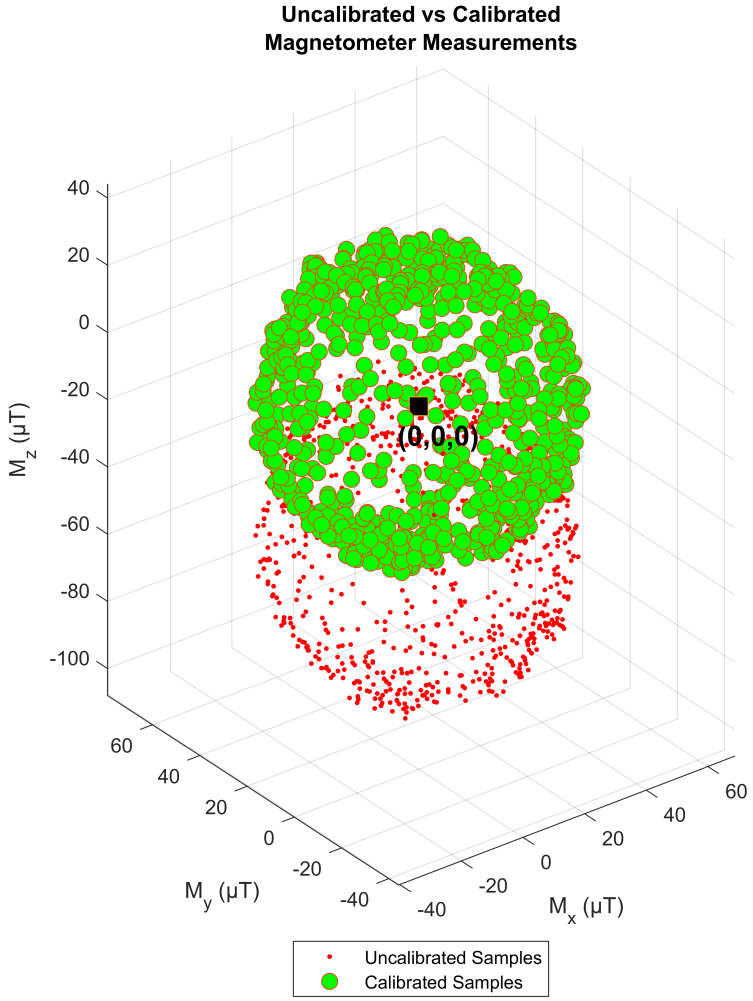

Figure 3.16. Uncalibrated vs calibrated magnetometer measurements.

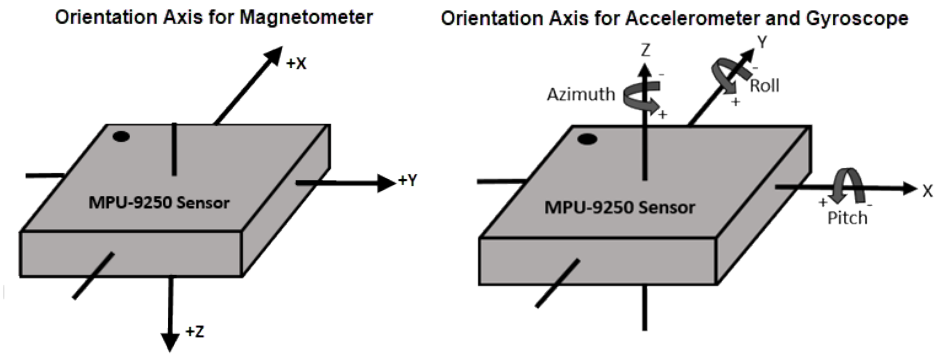

Figure 3.17. Axis orientation of mpu-9250 chipset [17].

An ideal (calibrated) accelerometer should measure the gravity on its corresponding axis. It means that when the MPU-9250 placed on a flat surface, the accelerometer inside the chip should measure $\begin{bmatrix}0 & 0 & 9.81\end{bmatrix}$ on x, y, and z-axis, respectively. However, even the most-expensive or most-reliable accelerometers cannot provide such a linear relationship so that there are always offset and scaling errors. To calibrate the MPU-9250 accelerometer, the latter procedure is followed. During this procedure, the cube placed on a flat surface, and it rotated to the requested axis when it prompted by the developed software.

- Rotate the cube as z-axis pointing upwards.
- Rotate the cube as z-axis pointing downwards.
- Rotate the cube as x-axis pointing upwards.
- Rotate the cube as x-axis pointing downwards.
- Rotate the cube as y-axis pointing upwards.
- Rotate the cube as y-axis pointing downwards.

The accelerometer readings were taken on each rotation and scale factor, and offset values are calculated for each axis based on these readings. To calculate the offset mean of maximum and minimum values from measurements corresponding to each axis are taken. Likewise, the scale factor is computed by dividing gravity (9.81 m/s^2) with the calculated offset.

$$\text{Offset} = \frac{(a_{max} + a_{min})}{2} \tag{3.3}$$

$$\text{Scale Factor} = \frac{G}{\frac{(a_{max}+a_{min})}{2}} \tag{3.4}$$

Subsequently, the calibrated value is achieved using Equation 3.5.

$$a_{calibrated} = (\frac{a_{raw}}{\text{Scale Factor}} + \text{Offset}) \tag{3.5}$$

3.4.3. Calibration of Gyroscope

The calibration of the gyroscope module is relatively easy compared to other modules described above. It is expected from an ideal gyroscope to measure zero on all axes when the sensor placed on a flat surface. To calibrate the gyroscope module, raw gyroscope readings are taken when the sensor completely fixed on a flat surface, and the average drift from the zero for each axis is calculated and then subtracted from the readings. The difference between uncalibrated gyroscope and calibrated gyroscope is shown in Figure 3.18.

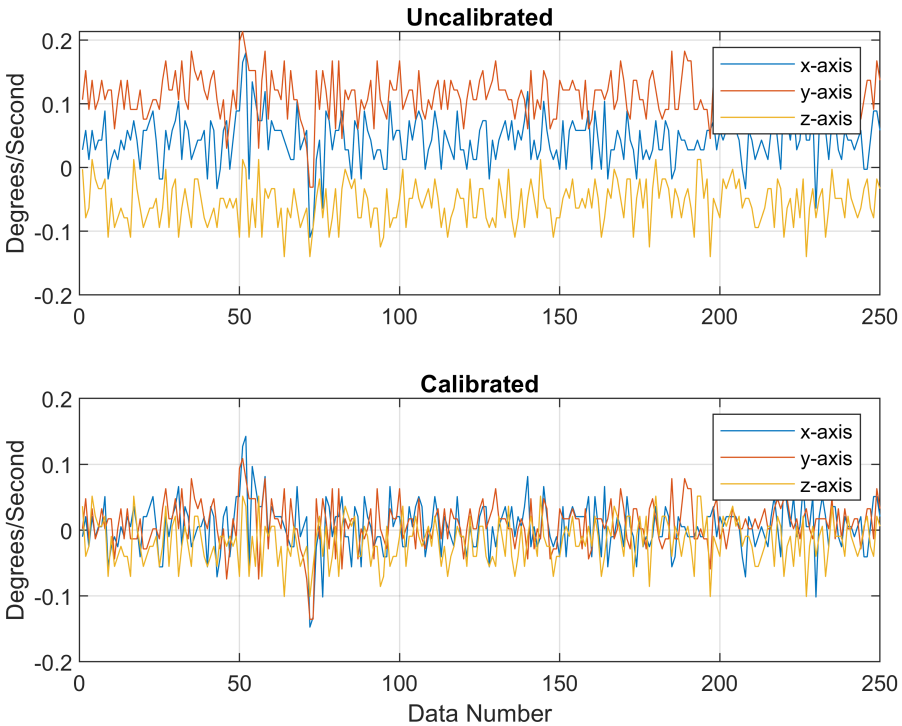

Figure 3.18. Calibrated and uncalibrated gyroscope measurements.

It should be noted that again, as all the calibration factors, acquired drift values slightly different for each IMU sensor, and each gyroscope should be calibrated by its own drift values.

3.5. Transducers

3.5.1. Pressure Transducers

TML's 500 kPa miniature pressure transducers are used for stress measurement. These sensors are designed especially for underwater use; therefore, require a stable uniform pressure to acquire reliable results.

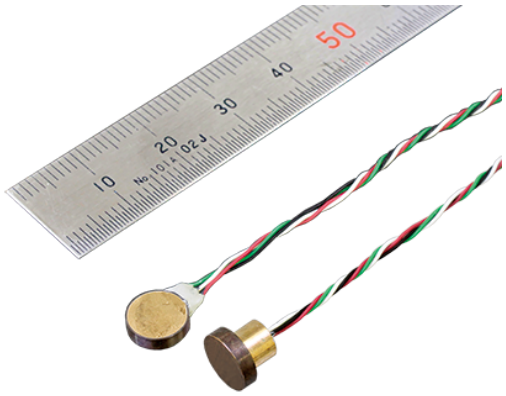

Figure 3.19. The miniature pressure sensor. [18]

The sensing surface of the sensor shouldn't be physically in contact with any particle. Inherently these sensors are not capable of using with soil particles since the sensor requires uniform pressure. Thus, the direct usage of these sensors with soil particles is not possible and requires modification.

A pacifier filled with distilled water and a miniature pressure sensor placed inside the silicon part is used to make this sensor operable with soil. The idea is once the stress is applied to the silicone of the pacifier, the water pressure inside will increase, and the sensor will be able to measure the applied stress.

To be able to record the data during the experiments NI-DAQmx hardware produced by National Instruments is used. The data from the sensor is collected by NI-DAQmx and then using the NI supported libraries the data is stored and analyzed using a developed Matlab script.

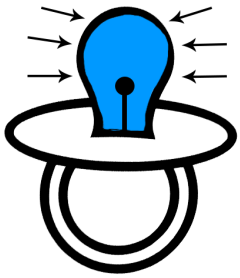

Figure 3.20. Conceptual drawing of pressure transducer inside a pacifier.

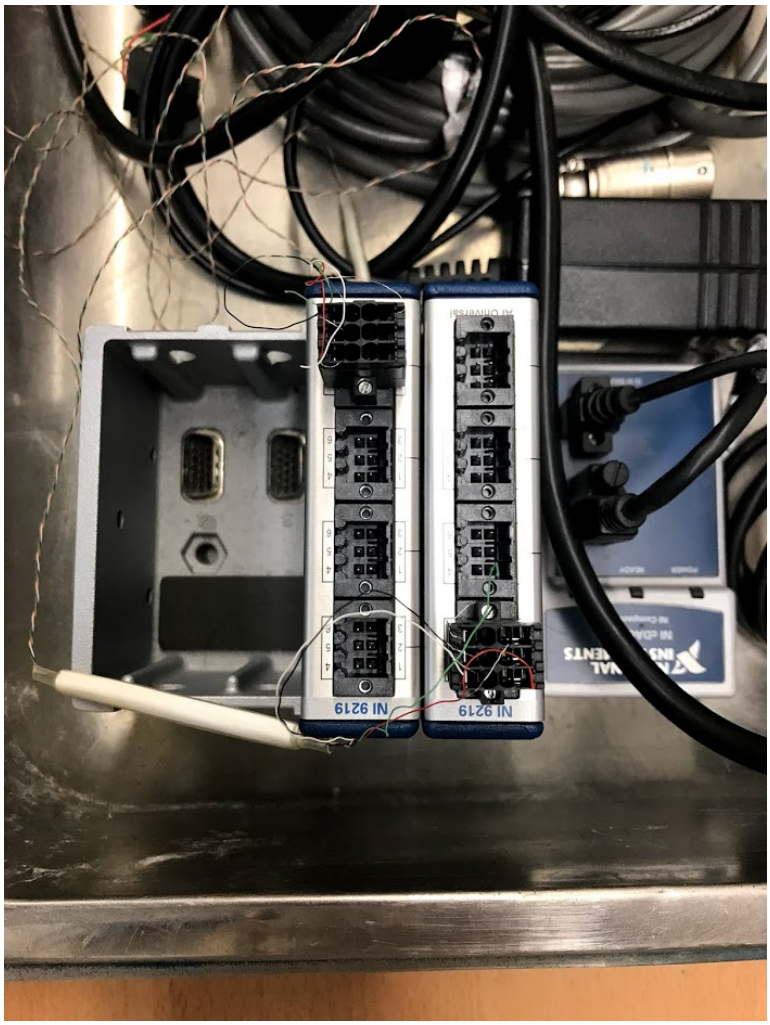

Figure 3.21. NI-DAQMX data acquisition system.

3.5.1.1. Calibration of Pressure Transducers. In order to achieve reliable results and distinguish the raw mV/V values to the corresponding pressure values, miniature pressure sensors need to be calibrated. The sensor taped at the bottom of a bucket, and the bucket is started to gradually filled with water. After each increment, the water level and mV/V values are recorded. As the water level in the bucket increases, the pressure at the bottom where the sensors are taped also increases. Using this relation and the data, an equation is constructed to convert mV/V to pressure (kPa).

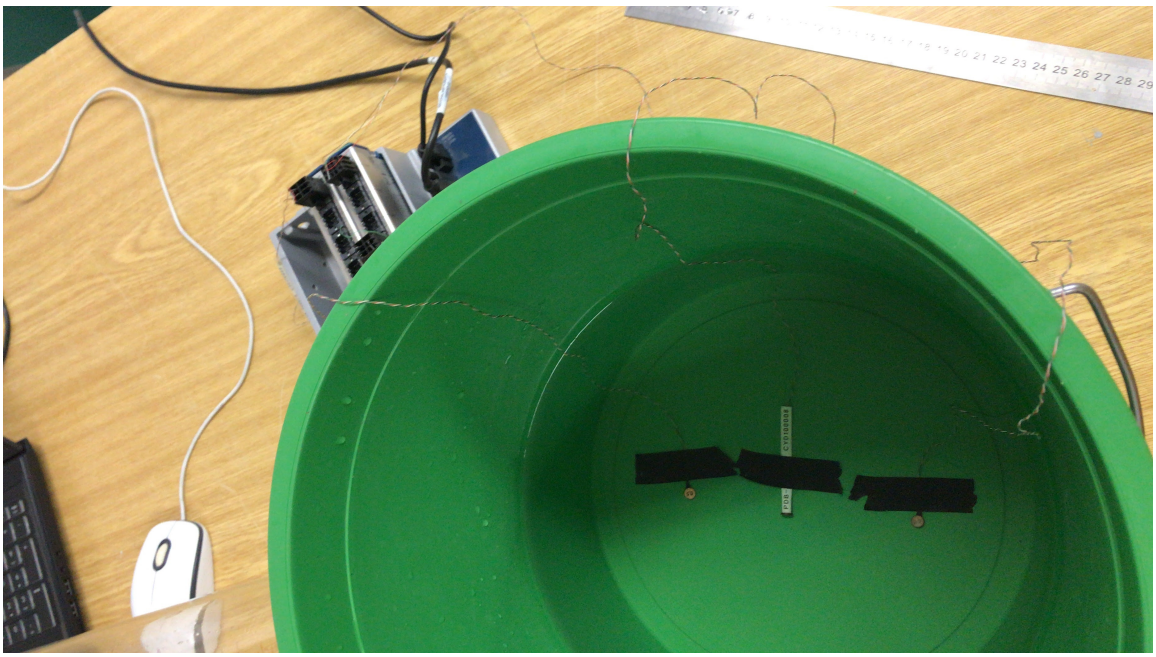

Figure 3.22. Calibration method of miniature pressure sensors.

3.5.2. Vertical Displacement Transducers

The vertical displacement transducers are used to measure the displacement of concrete blocks at specific locations and compared with the measurements taken from the magnetometer. SDP-100C high-sensitivity transducers produced by TML is selected for this purpose.

3.5.2.1. Calibration of Vertical Displacement Transducers. A big-scale direct-shear machine is used to calibrate the displacement transducers.

The transducer fixed on wood with a laser meter and placed carefully on the top of the soil, as shown in Figure 3.23. The machine set to displace at a rate of 1 mm per minute. To assure the displacement rate, a Bosch Dle 40 professional laser meter used and readings are taken at one-minute intervals.

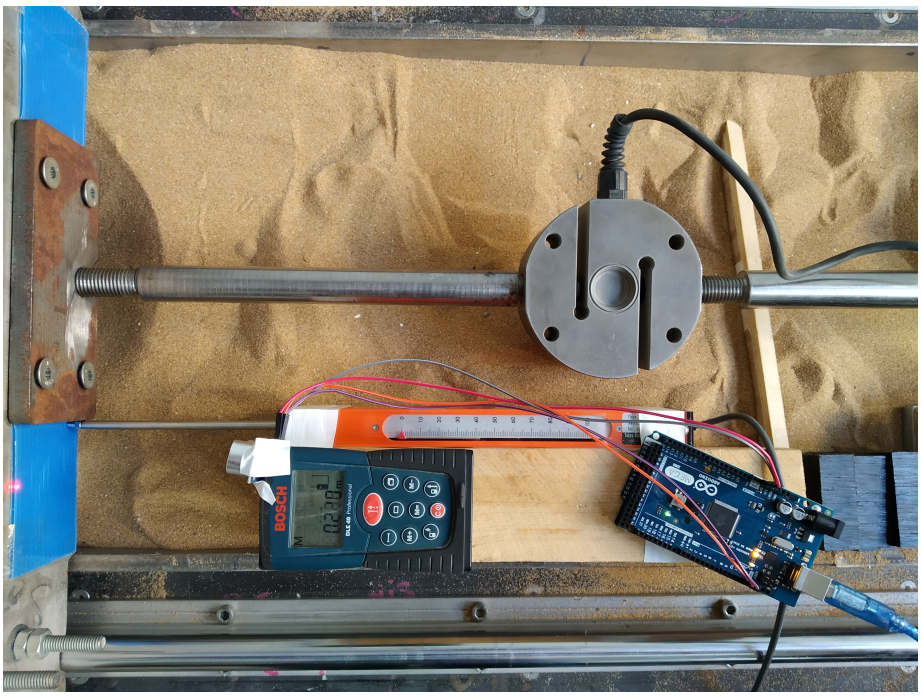

Figure 3.23. LVDT calibration setup.

The recorded data is used formulate the relationship between the electrical value given by LVDT and the recorded displacement. Several different type of regression analysis done and their sum of squares due to error (SSE), R-square, degrees of freedom (DFE), adjusted R-square and root mean square error (RMSE) parameters are summarized in Table 3.7.

The decision of which regression type will be used made based on by considering the lower RMSE value which describes the less error thereby the more accurate prediction.

Table 3.7. Summary of fits.

Fit Type	**SSE**	**R-square**	**DFE**	**Adj R-sq**	**RMSE**
Linear Fitting	3.29	0.99	22	0.99	0.39
Polynomial (1st)	19.94	0.99	23	0.99	0.93
Smoothing Spline	0.30	0.99	8.84	0.99	0.65

4. TEST RESULTS & ANALYSIS

4.1. Miniature Stress Transducer Enclosed in Pacifier

A 500 kPa miniature pressure transducer is tested, whether it will be able to measure soil pressure. The transducers' manufacturer recommends no physical touching to the sensing area during the measurement; therefore, it needs to be modified to use with soil particles. To overcome this problem, the pressure transducer was placed into a silicone pacifier that was filled with distilled and de-aired water. A gap was opened to place the sensor inside the pacifier and then it was sealed with Sugru, a waterproof moldable glue. The main idea is that once the pressure is applied over the soil, it will be transmitted to the pacifier. The applied pressure will increase the water pressure inside the pacifier, and the transducer would be able to measure the change.

Figure 4.1. The miniature stress transducer enclosed in pacifier.

For loading-unloading and to test the setup, a large-scale direct shear machine was used. This device mainly consists of a large shear box (two parts as the lower and upper box) and pneumatic muscles for normal loading. The upper box has dimensions of 0.30x0.30x0.20 m, and the lower box 0.90x0.30x0.60 m. The system offers several advantages, such as the application of static and cyclic loading with precise stress-strain control in the same device. Also, its large box allows placing an individual or group of piles to simulate piles' behavior under the soil.

Figure 4.2. Overall view of large-scale direct shear device.

The modified pacifier was tested under different loading-unloading conditions using the machine, as mentioned above. The pacifier was placed at the bottom of the upper box, as shown in Figure 4.3, and the box was filled with natural sand. The soil was exposed vertically to 2 kPa, 4 kPa, 8 kPa, 16 kPa, 32 kPa, 50 kPa, and 75 kPa of pressures and mV/V values for each, were recorded from the pressure transducer.

The corresponding mV/V values for each pressure is shown in Table 4.1, 4.2, 4.3, and 4.4 for group A, B, C, and D experiments.

4.2. Prescaled Stress Films

The 5LW type prescaled stress films, which supports range between 5 kPa to 50 kPa, were used to examine the lateral pressure exerted on the segmental pile. Experiments were performed using the large-scale direct shear device. The prescaled stress films were attached to the front face of selected blocks of the segmental pile.

Figure 4.3. Placement of pacifier inside the box.

Table 4.1. Corresponding mv/v values from 4 experiments in group a.

Pressure (kPa)	**A1 (mV/V)**	**A2 (mV/V)**	**A3 (mV/V)**	**A4 (mV/V)**
2.00	725.49	726.77	727.55	727.35
4.00	726.02	727.17	727.84	727.87
8.00	726.73	727.76	728.50	728.54
16.00	727.50	729.32	730.46	730.91
32.00	729.34	734.56	736.30	737.00
50.00	733.51	740.99	742.97	743.97
75.00	741.78	749.83	752.22	752.79

Table 4.2. Corresponding mv/v values from 4 experiments in group b.

Pressure (kPa)	**B1 (mV/V)**	**B2 (mV/V)**	**B3 (mV/V)**
2.00	737.09	737.66	737.11
4.00	737.19	738.12	737.23
8.00	738.75	740.48	740.91
16.00	745.20	746.78	746.89
32.00	756.74	755.99	755.61
50.00	765.99	764.89	763.54
75.00	778.84	775.66	774.94

Table 4.3. Corresponding mv/v values from 4 experiments in group c.

Pressure (kPa)	**C1 (mV/V)**	**C2 (mV/V)**	**C3 (mV/V)**
2.00	727.05	733.37	733.07
4.00	728.44	733.45	733.65
8.00	729.39	733.79	733.95
16.00	731.04	734.50	734.63
32.00	733.47	735.61	735.57
50.00	735.51	736.85	736.46
75.00	737.86	738.42	738.05

Table 4.4. Corresponding mv/v values from 4 experiments in group d.

Pressure (kPa)	**D1 (mV/V)**	**D2 (mV/V)**	**D3 (mV/V)**	**D4 (mV/V)**
2.00	729.31	735.12	735.73	735.69
4.00	730.40	735.24	735.85	735.90
8.00	731.39	735.58	736.14	736.22
16.00	732.40	736.18	736.66	736.80
32.00	733.64	737.02	737.43	737.60
50.00	735.04	737.78	738.21	738.34
75.00	737.11	739.10	739.45	739.60

The segmental pile was placed vertically into the container that has dimensions of 0.60 x 0.30 x 0.40 m, and the top head of the pile was fixed. The box was then filled with natural sand in the loose state ($D_r = 33\%$). The fixed pile head and the direction of movement of the upper box is shown in Figure 4.4.

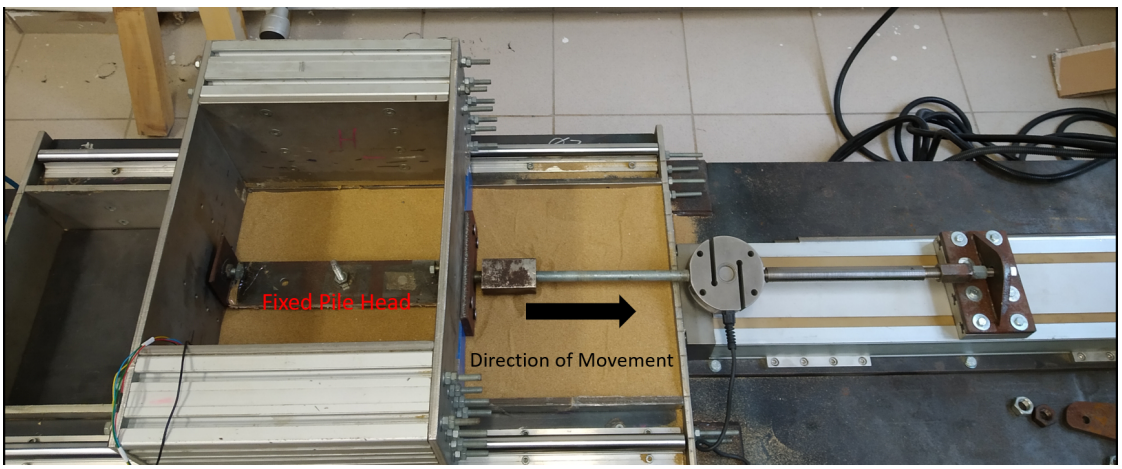

Figure 4.4. The fixed pile head and direction of movement of the upper box.

The segmental pile used in these experiments has 11 concrete mortar blocks and 10 shore 60 rubber between the blocks. The prescaled films were placed on Block 11, Block 9, Block 7, Block 5, Block 3, and Block 1, as illustrated in Figure 4.5.

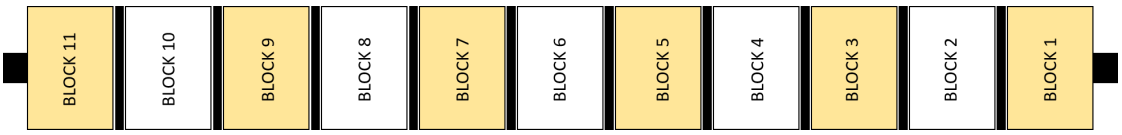

Figure 4.5. The segmental pile and locations of prescaled films (colored blocks).

A total of three experiments were performed. In all three experiments, the cable tension of the segmental pile was set to 750 N, and the upper box of the machine where the pile head is fixed on, was allowed to displace up to 5 cm with a rate of 1 mm per minute. The tension of the cable was verified using a load-cell that is placed between two of the blocks. The horizontal load vs. displacement chart is shown in Figure 4.6.

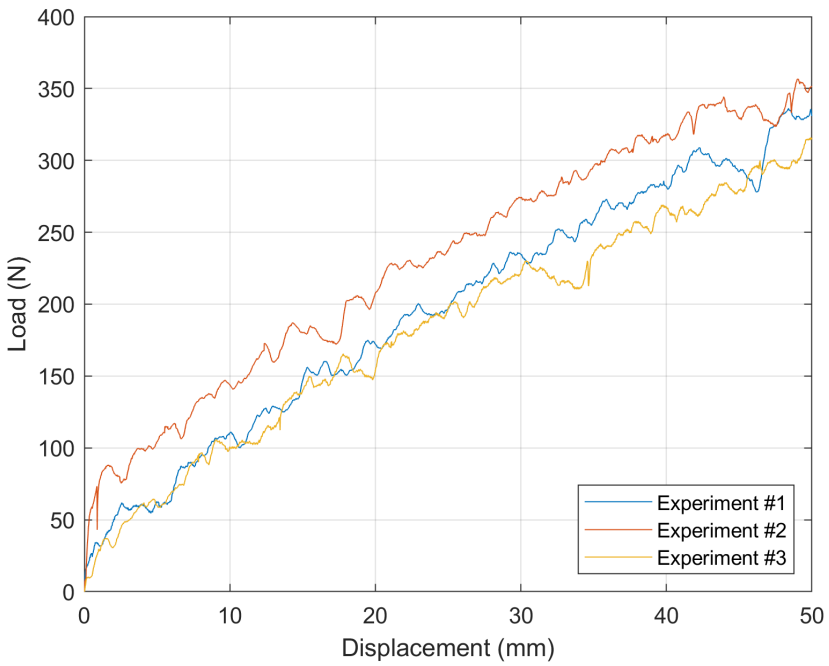

Figure 4.6. The horizontal load vs. displacement chart.

After the experiments are done, the prescaled films were removed carefully and were analyzed using the dedicated software. The average and the maximum pressures from each experiment shown in Table 4.5, Table 4.6, and Table 4.7 for experiments 1, 2, and 3, respectively.

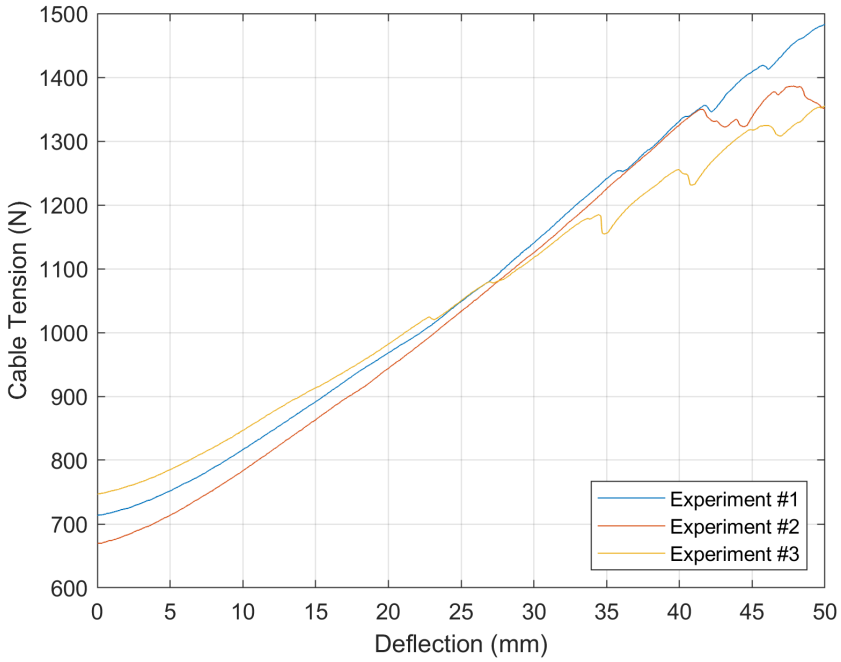

Figure 4.7. Cable tension vs. displacement chart.

Also, the calculated inclination angles from IMU sensors are presented in Table 4.8, Table 4.9, and Table 4.10 for experiments 1, 2, and 3, respectively. The corresponding blocks are shown in Figure 4.8, Figure 4.9, and Figure 4.10.

4.3. Three-Point Bending Test

Three-point bending experiments were performed using MTS 370 Load Frame. The segmental pile was placed into a span and both of the ends were fixed. The normal load was applied in the middle of the pile, as shown in Figure 4.11.

In order to measure the post-tension on the pile, a load cell was placed between the concrete mortar blocks. Before starting all of the experiments, the tension on the cable in the segmental pile was adjusted to 750 N. The experimental data collected from four different sources, are presented in Table 4.11.

Table 4.5. The results obtained from dedicated software for experiment 1.

Range (kPa)	**Pressed Area (%)**	**Average P. (kPa)**	**Maximum P. (kPa)**
$p < 15$	6.45	14.00	15.00
$15 \leq p \leq 19$	5.00	17.00	19.00
$19 < p \leq 24$	15.97	22.00	23.00
$24 < p \leq 28$	43.87	26.00	28.00
$28 < p \leq 33$	18.70	30.00	32.00
$33 < p \leq 37$	10.00	34.00	36.00
$37 < p \leq 41$	0.00	0.00	0.00
$41 < p \leq 46$	0.00	0.00	0.00
$50 < p$	0.00	0.00	0.00

Table 4.6. The results obtained from dedicated software for experiment 2.

Range (kPa)	**Pressed Area (%)**	**Average P. (kPa)**	**Maximum P. (kPa)**
$p < 15$	7.84	14.00	15.00
$15 \leq p \leq 19$	10.45	17.00	19.00
$19 < p \leq 24$	13.54	22.00	23.00
$24 < p \leq 28$	38.96	26.00	28.00
$28 < p \leq 33$	19.72	30.00	32.00
$33 < p \leq 37$	9.50	34.00	36.00
$37 < p \leq 41$	0.00	0.00	0.00
$41 < p \leq 46$	0.00	0.00	0.00
$50 < p$	0.00	0.00	0.00

Table 4.7. The results obtained from dedicated software for experiment 3.

Range (kPa)	**Pressed Area (%)**	**Average P. (kPa)**	**Maximum P. (kPa)**
$p < 15$	2.89	14.00	15.00
$15 \leq p \leq 19$	12.86	18.00	19.00
$19 < p \leq 24$	19.16	22.00	23.00
$24 < p \leq 28$	42.26	26.00	28.00
$28 < p \leq 33$	19.42	30.00	32.00
$33 < p \leq 37$	3.31	33.00	35.00
$37 < p \leq 41$	0.00	0.00	0.00
$41 < p \leq 46$	0.00	0.00	0.00
$50 < p$	0.00	0.00	0.00

Table 4.8. Degree of change in y-axis from experiment 1.

Block/Displacement (cm)	**1 cm**	**2 cm**	**3 cm**	**4 cm**	**5 cm**
Block 1	4.42	3.40	5.68	5.29	6.48
Block 2	-3.91	-2.25	-3.39	-3.80	-0.92
Block 3	0.65	2.30	1.26	0.10	-1.03
Block 4	2.72	1.72	2.13	-1.09	0.50
Block 5	-0.80	-3.42	-6.08	-7.21	-7.87
Block 6	1.54	0.89	1.84	1.87	1.63
Block 7	-0.54	-0.32	-0.08	-3.24	-4.23
Block 8	-4.41	-7.54	-9.32	-6.77	-6.94
Block 9	6.22	5.79	9.84	5.67	8.73
Block 10	5.73	0.96	-2.40	-3.18	-3.63
Block 11	7.86	5.46	8.20	17.49	24.55

Table 4.9. Degree of change in y-axis from experiment 2.

Block/Displacement (cm)	**1 cm**	**2 cm**	**3 cm**	**4 cm**	**5 cm**
Block 1	2.80	2.94	6.54	10.10	6.92
Block 2	5.41	10.18	8.06	9.77	9.48
Block 3	-0.50	0.48	-0.66	-1.55	0.82
Block 4	2.58	-2.85	-4.57	-4.00	-4.62
Block 5	3.75	-1.18	-1.35	-2.36	-4.28
Block 6	1.80	1.17	0.89	4.19	0.79
Block 7	-0.74	-5.82	-5.88	-9.14	-7.77
Block 8	-1.77	-4.69	-6.07	-8.47	-11.38
Block 9	2.06	-0.33	2.25	4.00	-0.04
Block 10	-5.89	0.01	-8.41	-6.28	-14.70
Block 11	6.43	2.59	-0.35	7.77	20.55

Table 4.10. Degree of change in y-axis from experiment 3.

Block/Displacement (cm)	**1 cm**	**2 cm**	**3 cm**	**4 cm**	**5 cm**
Block 1	-1.43	0.96	3.65	0.90	0.03
Block 2	1.33	2.11	2.10	3.84	4.81
Block 3	1.45	2.38	-0.60	1.73	-0.47
Block 4	-0.77	-1.72	-1.91	-2.63	-3.09
Block 5	0.34	0.30	-0.18	-4.20	-4.05
Block 6	-2.77	-2.55	-3.79	-4.02	-0.33
Block 7	-5.39	-5.44	-5.62	-5.78	-8.11
Block 8	-3.65	-6.28	-9.96	-7.34	-10.00
Block 9	-0.75	2.86	1.18	2.83	1.89
Block 10	-0.97	3.77	-2.57	-4.43	-8.74
Block 11	0.78	1.88	2.70	8.31	13.72

Figure 4.8. Blocks at specificied deflections from experiment 1.

Figure 4.9. Blocks at specificied deflections from experiment 2.

Figure 4.10. Blocks at specificied deflections from experiment 3.

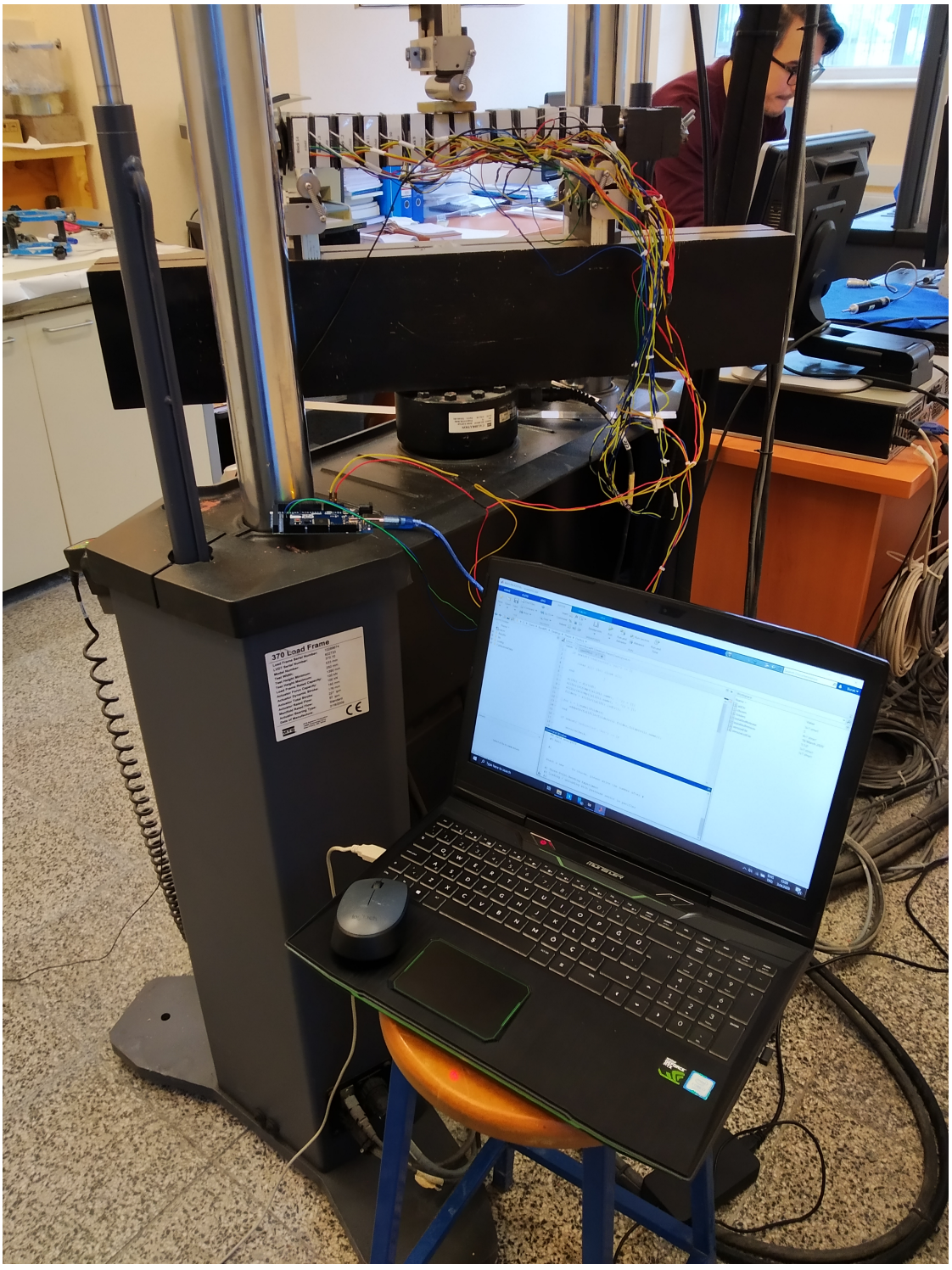

Figure 4.11. Three-point bending experiment setup.

Table 4.11. Experiment data sources.

Source	**Data**
MTS 370 Load Frame	Load and Displacement at Mid-Point
NI-DAQmx	Post-Tension Force
Arduino Board	IMU Data
External LVDTs	Displacement at Block 5 and Block 11

A total of 9 three-point flexural tests were conducted in two different groups. The first group includes three experiments, while the second group includes six experiments. The differences between these experiments are summarized in the following Table 4.12. While deflection at the first group of experiments was only measured on Block 8 (by MTS), two external LVDTs were placed in the second group of experiments to measure the deflection on Block 5 and Block 11.

Table 4.12. Overview of three-point bending experiments.

Experiment #	**Group Number**	**Number of Blocks**	**LVDT on Blocks**
Experiment 1	Group 1	13	Block 8
Experiment 2	Group 1	13	Block 8
Experiment 3	Group 1	13	Block 8
Experiment 4	Group 2	14	Block 5,8,11
Experiment 5	Group 2	14	Block 5,8,11
Experiment 6	Group 2	14	Block 5,8,11
Experiment 7	Group 2	14	Block 5,8,11
Experiment 8	Group 2	14	Block 5,8,11
Experiment 9	Group 2	14	Block 5,8,11

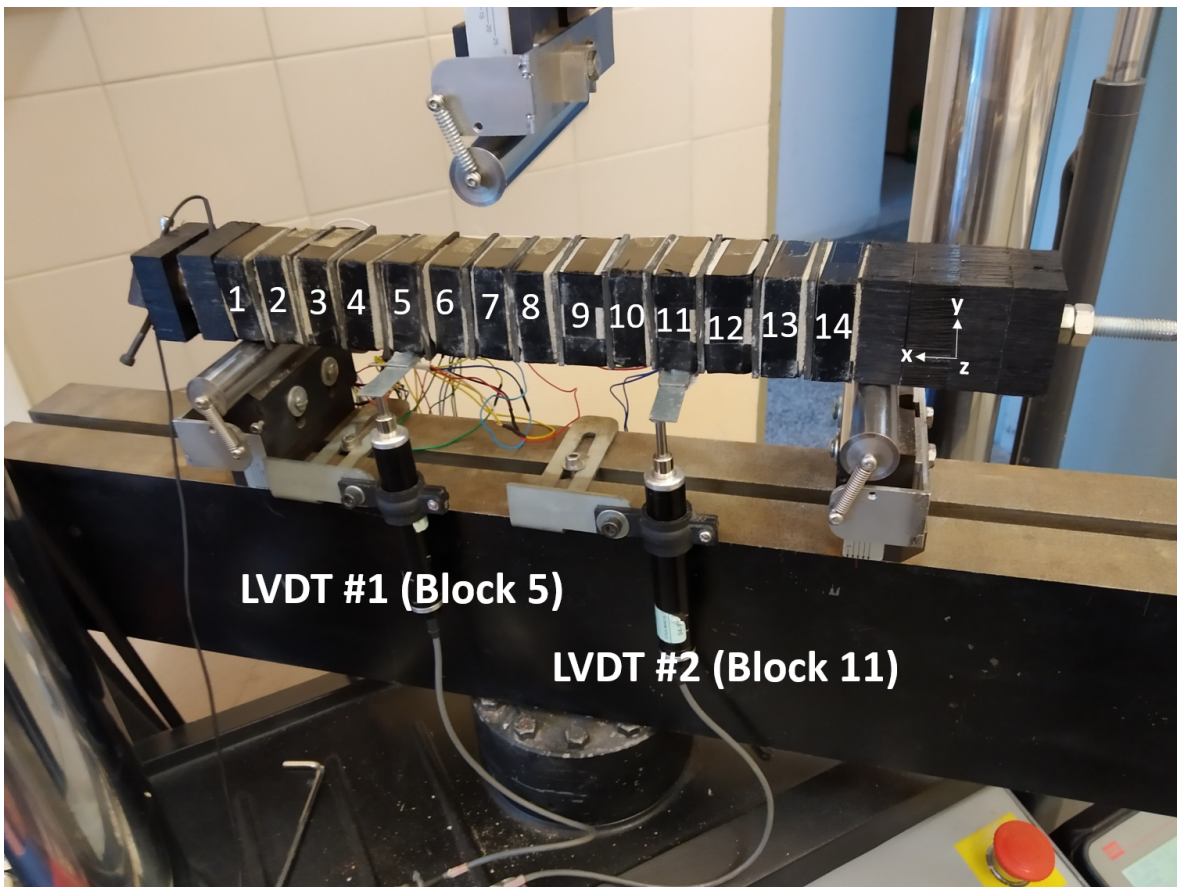

Figure 4.12. External lvdts on block 5 and block 11 (group 2 experiments).

4.3.1. Inclination Angles

The data obtained from the accelerometer, magnetometer, and gyroscope sensors via IMU chips were used to construct the sensor body on the space by sensor fusion. The degree of rotation on three axes (x, y, and z) were calculated based on that estimation. After that, the deflection of each block was formulated on the degree of rotation of these blocks. Therefore, the degree rotation of the body in three axes is the base and most accurate information. The derivation of deflection from this information requires certain assumptions which leads to propagation of error. Therefore, the degree of rotation in three axes from all experiments is presented at selected mid-point deflections. (Table A.1 to Table 4.16) In several rows, "N/A" indicates data was not available for that block due to technical problems (i.e: short circuit occurred at moment).

4.3.2. Flexural Rigidity of Segmental Pile

The flexural rigidity of the segmental pile was determined using the results of the three-point flexural test. In all three-point bending experiments performed according to ASTM D790, and the segmental pile was allowed to displace up to 20 mm.

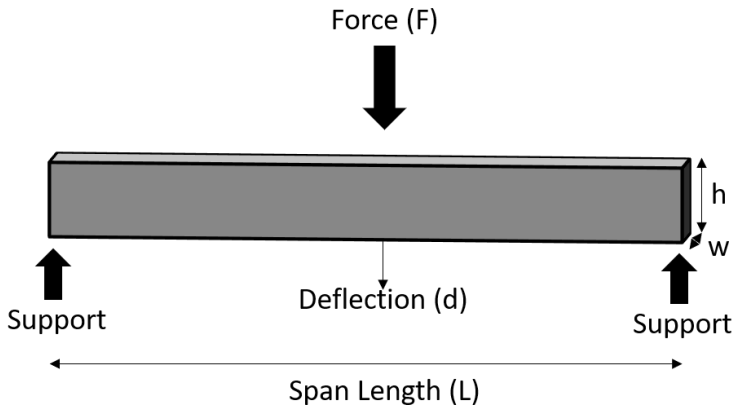

Figure 4.13. Three-point bending theory.

Table 4.13. Degree of change in x, y and z axes from experiment 6.

Deflection at Mid Point (cm)	**X (Degree)**	**Y (Degree)**	**Z (Degree)**
Block 2			
0.50	0.64	0.71	-0.91
1.00	0.55	0.19	-0.00
1.50	0.64	0.67	-0.11
2.00	0.04	0.40	-0.83
Block 3			
0.50	-0.83	-0.53	-1.55
1.00	-0.93	1.38	-3.52
1.50	-1.10	0.70	-5.40
2.00	-1.28	-0.73	-0.10
Block 4			
0.50	0.17	0.38	-1.99
1.00	-0.26	0.51	-3.99
1.50	-0.41	2.70	-5.68
2.00	-0.46	0.22	-0.62
Block 5			
0.50	-2.98	-6.19	-5.77
1.00	-3.42	-6.26	-3.98
1.50	-3.57	-5.62	-2.32
2.00	-3.79	-6.84	-7.03
Block 6			
0.50	-2.65	-9.45	3.83
1.00	-3.24	-7.19	2.57
1.50	-3.69	-6.62	1.23
2.00	-2.96	-9.52	4.88

Table 4.13. Degree of change in x, y and z axes from experiment 6 (cont.).

Deflection at Mid Point (cm)	**X (Degree)**	**Y (Degree)**	**Z (Degree)**
Block 7			
0.50	1.93	3.31	7.16
1.00	1.69	4.03	6.20
1.50	1.49	5.28	5.06
2.00	1.89	4.12	7.08
Block 8			
0.50	6.04	3.13	6.09
1.00	7.06	5.84	5.12
1.50	7.96	7.79	4.29
2.00	5.63	2.09	6.20
Block 9			
0.50	6.81	5.35	4.48
1.00	6.82	5.86	3.48
1.50	6.95	6.77	2.16
2.00	6.27	6.15	5.54
Block 10			
0.50	N/A	N/A	N/A
1.00	N/A	N/A	N/A
1.50	N/A	N/A	N/A
2.00	N/A	N/A	N/A
Block 11			
0.50	5.10	9.08	2.97
1.00	5.73	7.55	0.70
1.50	5.88	7.53	1.18
2.00	4.85	6.45	4.40

Table 4.13. Degree of change in x, y and z axes from experiment 6 (cont.).

Deflection at Mid Point (cm)	**X (Degree)**	**Y (Degree)**	**Z (Degree)**
Block 12			
0.50	1.65	2.95	5.25
1.00	2.04	2.85	3.05
1.50	2.63	2.51	0.82
2.00	1.51	3.29	6.61
Block 13			
0.50	-0.73	1.33	4.99
1.00	-0.46	1.01	2.80
1.50	-0.14	0.58	0.62
2.00	-0.80	1.01	6.40
Block 14			
0.50	0.07	0.22	0.12
1.00	0.53	0.27	0.78
1.50	0.95	0.93	0.70
2.00	0.97	0.51	0.55

Table 4.14. Degree of change in x, y and z axes from experiment 7.

Deflection at Mid Point (cm)	**X (Degree)**	**Y (Degree)**	**Z (Degree)**
Block 2			
0.50	0.70	0.13	-0.30
1.00	0.80	0.77	-0.10
1.50	0.47	0.79	-0.22
2.00	0.50	0.68	-0.18
Block 3			
0.50	-0.61	-0.64	-1.30
1.00	-0.77	-0.11	-3.44
1.50	-0.92	0.28	-5.43
2.00	-0.84	-0.16	-2.34
Block 4			
0.50	0.10	0.13	-1.91
1.00	-0.10	0.52	-3.90
1.50	-0.34	1.21	-5.85
2.00	-0.13	0.03	-2.86
Block 5			
0.50	-3.29	-6.72	-5.85
1.00	-3.50	-6.31	-4.34
1.50	-3.63	-6.28	-2.59
2.00	-3.11	-6.67	-5.37
Block 6			
0.50	-2.77	-9.91	4.05
1.00	-3.15	-9.24	2.58
1.50	-3.65	-6.69	1.42
2.00	-3.12	-8.71	3.47

Table 4.14. Degree of change in x, y and z axes from experiment 7 (cont.).

Deflection at Mid Point (cm)	**X (Degree)**	**Y (Degree)**	**Z (Degree)**
Block 7			
0.50	1.99	2.87	7.32
1.00	2.02	4.01	6.42
1.50	1.75	4.91	5.24
2.00	2.26	4.02	6.90
Block 8			
0.50	8.03	8.26	4.00
1.00	8.89	9.26	3.38
1.50	9.15	8.35	3.28
2.00	8.24	8.40	3.60
Block 9			
0.50	6.95	5.44	4.76
1.00	6.59	5.35	3.84
1.50	6.87	6.27	2.55
2.00	6.27	5.74	4.81
Block 10			
0.50	N/A	N/A	N/A
1.00	N/A	N/A	N/A
1.50	N/A	N/A	N/A
2.00	N/A	N/A	N/A
Block 11			
0.50	5.32	8.21	3.14
1.00	5.86	7.45	1.04
1.50	6.14	7.69	1.09
2.00	5.78	8.86	2.13

Table 4.14. Degree of change in x, y and z axes from experiment 7 (cont.).

Deflection at Mid Point (cm)	**X (Degree)**	**Y (Degree)**	**Z (Degree)**
Block 12			
0.50	1.93	2.48	5.29
1.00	2.51	3.73	3.17
1.50	2.99	3.73	0.91
2.00	2.23	2.90	4.40
Block 13			
0.50	-0.36	2.11	5.20
1.00	-0.02	1.68	2.98
1.50	0.19	1.67	0.84
2.00	-0.29	1.45	4.21
Block 14			
0.50	0.36	0.97	0.18
1.00	0.89	0.41	0.86
1.50	0.24	0.04	0.76
2.00	0.74	0.22	0.11

Table 4.15. Degree of change in x, y and z axes from experiment 8.

Deflection at Mid Point (cm)	**X (Degree)**	**Y (Degree)**	**Z (Degree)**
Block 2			
0.50	0.06	0.00	-0.46
1.00	0.16	0.25	-0.19
1.50	0.17	0.13	-0.12
2.00	0.20	0.85	-0.51
Block 3			
0.50	-0.46	0.22	-1.35
1.00	-0.52	0.69	-3.45
1.50	-0.69	1.02	-5.31
2.00	-0.50	0.58	-2.07
Block 4			
0.50	0.35	1.20	-1.74
1.00	0.28	1.62	-3.83
1.50	-0.02	2.53	-5.72
2.00	0.36	2.96	-2.45
Block 5			
0.50	-2.74	-4.60	-6.08
1.00	-3.01	-4.54	-4.54
1.50	-3.29	-3.32	-2.90
2.00	-2.55	-4.38	-5.85
Block 6			
0.50	-2.59	-9.18	4.21
1.00	-2.90	-6.85	2.96
1.50	-3.45	-4.94	1.59
2.00	-2.65	-7.12	3.80

Table 4.15. Degree of change in x, y and z axes from experiment 8 (cont.).

Deflection at Mid Point (cm)	**X (Degree)**	**Y (Degree)**	**Z (Degree)**
Block 7			
0.50	2.56	4.40	7.43
1.00	2.78	5.28	6.31
1.50	2.28	6.43	5.27
2.00	2.68	5.15	7.14
Block 8			
0.50	8.91	0.32	3.72
1.00	9.03	0.94	3.74
1.50	9.27	0.91	3.86
2.00	9.41	1.36	3.17
Block 9			
0.50	6.72	6.38	5.40
1.00	6.58	7.52	4.47
1.50	6.89	8.65	2.91
2.00	6.76	7.51	5.08
Block 10			
0.50	N/A	N/A	N/A
1.00	N/A	N/A	N/A
1.50	N/A	N/A	N/A
2.00	N/A	N/A	N/A
Block 11			
0.50	6.03	9.90	3.20
1.00	6.57	7.49	0.99
1.50	7.09	8.08	-1.14
2.00	6.23	9.97	2.66

Table 4.15. Degree of change in x, y and z axes from experiment 8 (cont.).

Deflection at Mid Point (cm)	**X (Degree)**	**Y (Degree)**	**Z (Degree)**
Block 12			
0.50	2.57	4.59	5.38
1.00	3.29	5.54	3.12
1.50	3.83	4.97	0.74
2.00	2.92	4.92	4.61
Block 13			
0.50	0.17	2.37	5.12
1.00	0.59	2.85	2.96
1.50	0.75	2.48	0.77
2.00	0.38	2.60	4.48
Block 14			
0.50	0.10	0.83	0.18
1.00	0.51	0.00	0.82
1.50	0.95	0.44	0.70
2.00	0.14	0.61	0.62

Table 4.16. Degree of change in x, y and z axes from experiment 9.

Deflection at Mid Point (cm)	**X (Degree)**	**Y (Degree)**	**Z (Degree)**
Block 2			
0.50	0.21	0.12	-0.47
1.00	0.53	0.00	-0.64
1.50	0.32	0.15	-0.51
2.00	0.25	0.91	-0.34
Block 3			
0.50	-0.26	-0.45	-1.43
1.00	-0.67	-0.53	-3.48
1.50	-0.76	0.42	-5.30
2.00	-0.56	0.31	-4.67
Block 4			
0.50	0.37	0.64	-1.79
1.00	-0.05	0.79	-3.80
1.50	-0.20	1.57	-5.65
2.00	-0.21	1.91	-4.81
Block 5			
0.50	-2.92	-5.54	-6.43
1.00	-2.92	-4.93	-4.58
1.50	-3.18	-3.73	-2.90
2.00	-3.05	-4.93	-3.66
Block 6			
0.50	-2.53	-8.60	4.15
1.00	-3.05	-7.23	2.98
1.50	-3.47	-5.80	1.61
2.00	-3.20	-5.93	2.12

Table 4.16. Degree of change in x, y and z axes from experiment 9 (cont.).

Deflection at Mid Point (cm)	**X (Degree)**	**Y (Degree)**	**Z (Degree)**
Block 7			
0.50	2.81	3.54	7.29
1.00	2.59	4.48	6.42
1.50	2.20	5.67	5.31
2.00	2.41	5.39	5.64
Block 8			
0.50	8.36	8.48	4.55
1.00	9.39	9.16	3.53
1.50	9.34	9.19	3.92
2.00	9.89	9.83	3.10
Block 9			
0.50	6.64	7.66	5.71
1.00	6.90	8.52	4.33
1.50	6.87	9.44	3.12
2.00	6.73	7.87	3.87
Block 10			
0.50	N/A	N/A	N/A
1.00	N/A	N/A	N/A
1.50	N/A	N/A	N/A
2.00	N/A	N/A	N/A
Block 11			
0.50	6.26	9.88	3.33
1.00	6.53	7.40	1.09
1.50	7.18	7.67	1.07
2.00	7.03	7.15	0.22

Table 4.16. Degree of change in x, y and z axes from experiment 9 (cont.).

Deflection at Mid Point (cm)	**X (Degree)**	**Y (Degree)**	**Z (Degree)**
Block 12			
0.50	2.68	4.43	5.41
1.00	3.17	4.74	3.29
1.50	3.89	5.21	0.96
2.00	3.73	5.11	1.86
Block 13			
0.50	0.25	2.91	5.42
1.00	0.69	3.40	3.14
1.50	0.99	2.89	0.91
2.00	1.03	2.93	1.69
Block 14			
0.50	0.23	0.81	0.26
1.00	0.52	0.58	0.06
1.50	0.97	0.32	0.81
2.00	0.90	0.03	0.73

The flexural stress (σ_f) and the flexural strain (ϵ_f) were calculated using the Equation 4.1, and Equation 4.2, respectively. It should be noted that these equations assumes the pile is continuous. In these equations, F denotes for load at the mid-point (N), L is the pile length (0.325 m), b width of the beam (0.05 m), d depth of the beam (0.05 m), and D is the deflection at the center of the beam (m). The stress vs strain curve for experiments is shown in Figure 4.14, 4.15, and 4.16.

$$\sigma_f = \frac{3FL}{2bd^2} \tag{4.1}$$

$$\epsilon_f = \frac{6Dd}{L^2} \tag{4.2}$$

The flexural rigidity (EI) was calculated using the Equation 4.3. In the equation, P denotes for load at the mid-point (N), L is the pile length (0.325 m), D is the deflection at the center of the beam (m), and EI (N/m^2) is the flexural rigidity. The EI vs strain curve for experiments is shown in Figure 4.17, 4.18, and 4.19.

$$D = \frac{PL^3}{48EI} \tag{4.3}$$

4.3.3. Estimation of Deflection (with IMUs) in Blocks

As mentioned in previous chapters, IMUs were attached on each concrete mortar block, and data from the accelerometer, magnetometer, and gyroscope were recorded during the three-point-bending tests. The raw data were processed to obtain the degree of rotation, and the deflection in each block was estimated based on this data. To accomplish this task, an assumption was made. As may be noticed in Tables 4.13-4.16, the degree of rotation in z-axis is turning out to positive after Block 7 or Block 8. Based on this observation, it can be said that if a block has a positive degree in the z-axis, then it's left lower corner coincides with the left top corner of the lower block.

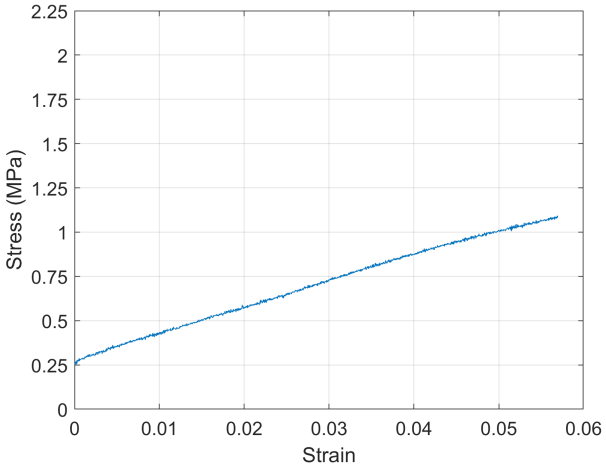

(a) experiment 1

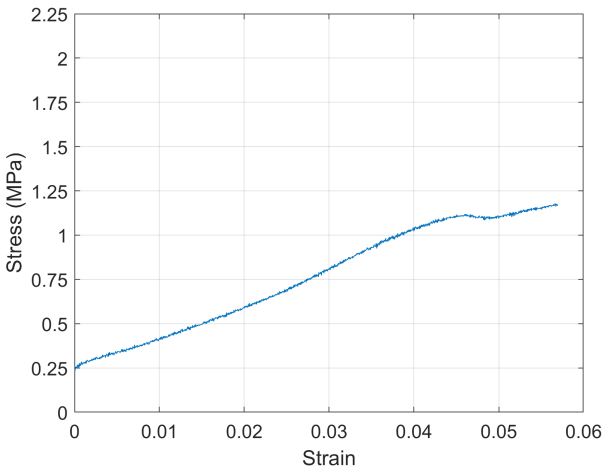

(b) experiment 2

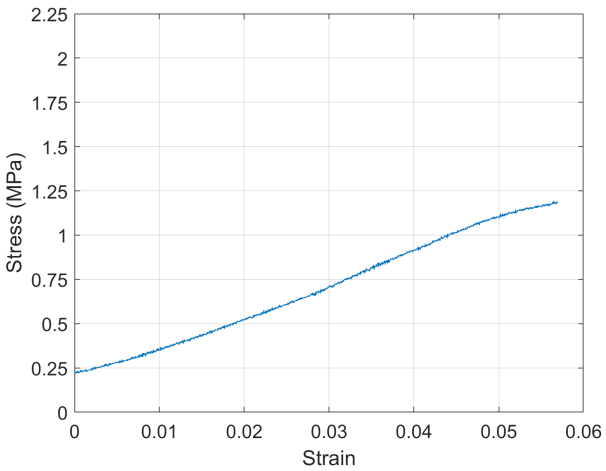

(c) experiment 3

Figure 4.14. Stress-strain curve for experiments in group 1.

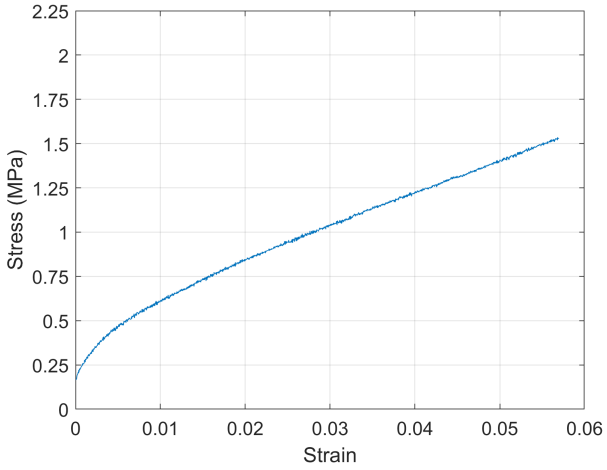

(a) experiment 4

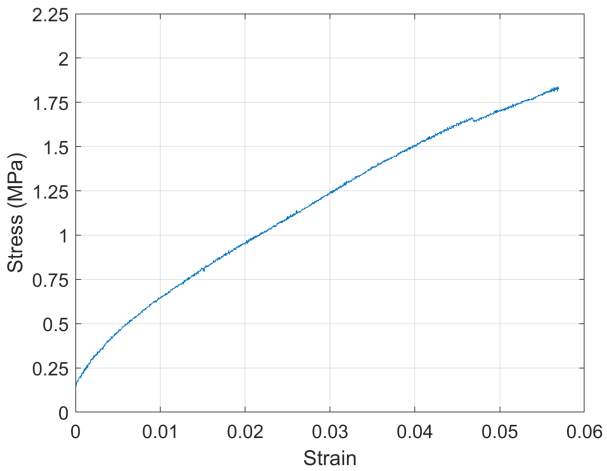

(b) experiment 5

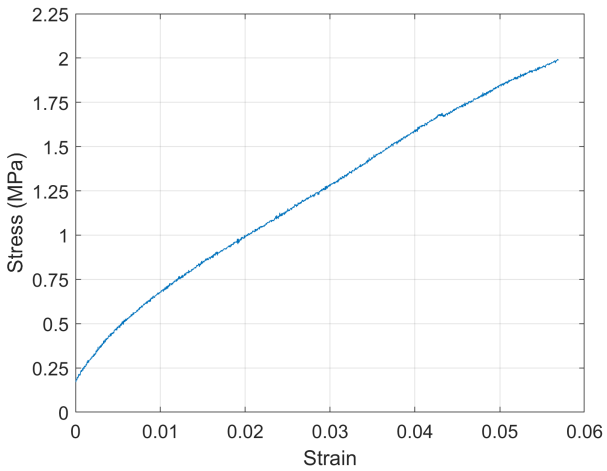

(c) experiment 6

Figure 4.15. Stress-strain curve for experiments 4, 5 and 6 in group 2.

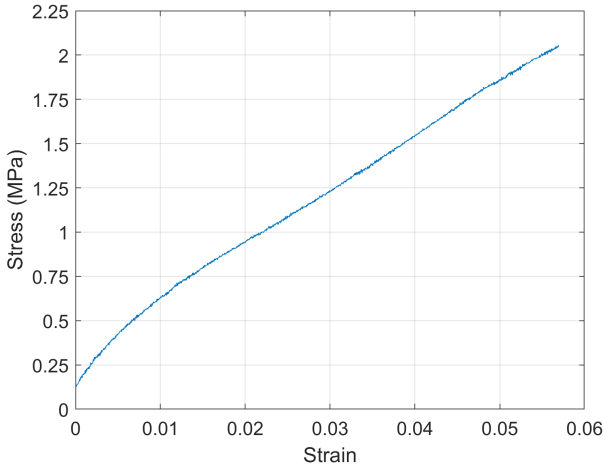

(a) experiment 7

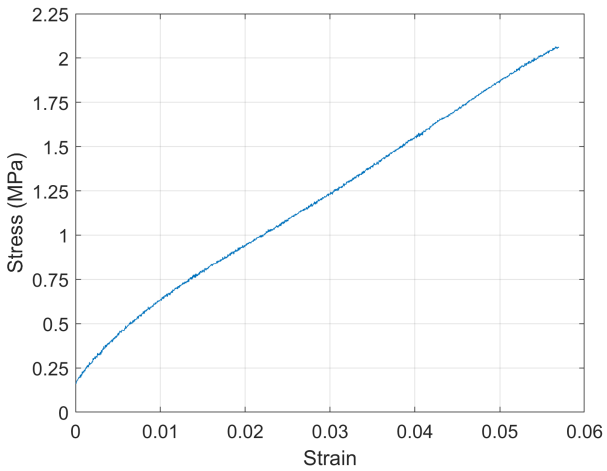

(b) experiment 8

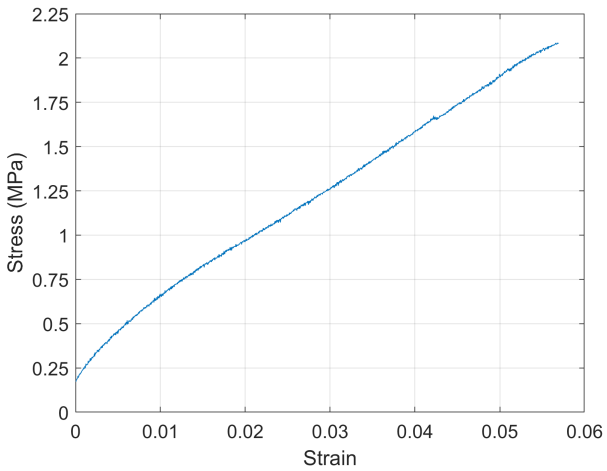

(c) experiment 9

Figure 4.16. Stress-strain curve for experiments 7, 8 and 9 in group 2.

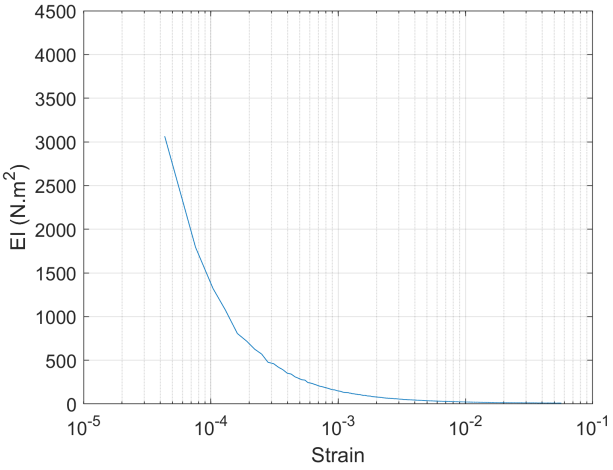

(a) experiment 1

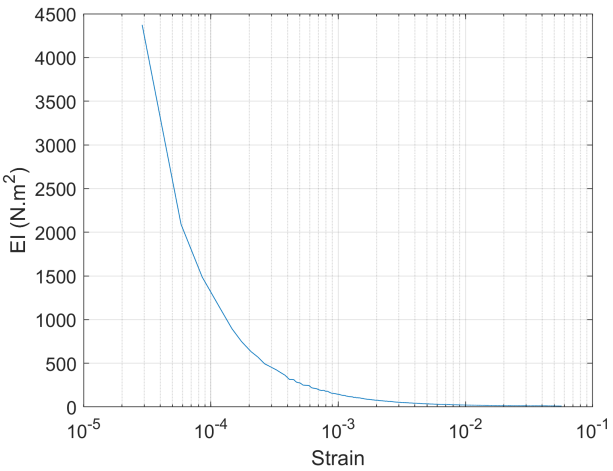

(b) experiment 2

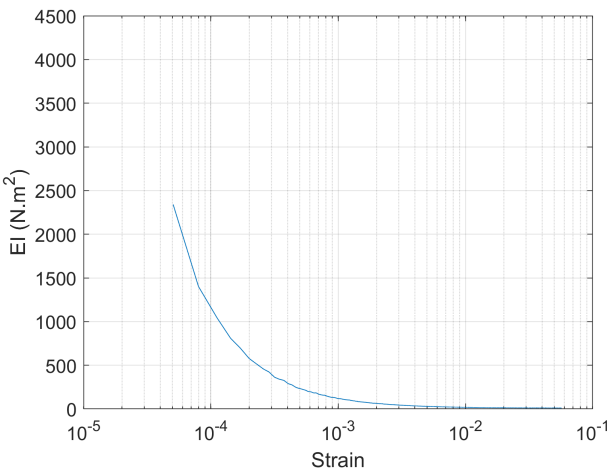

(c) experiment 3

Figure 4.17. EI-strain curve for experiments in group 1.

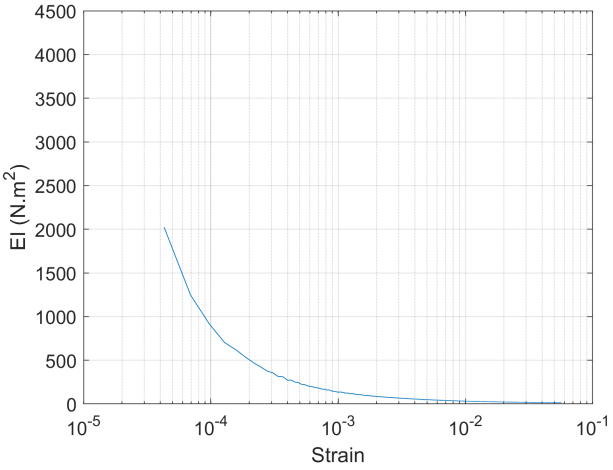

(a) experiment 4

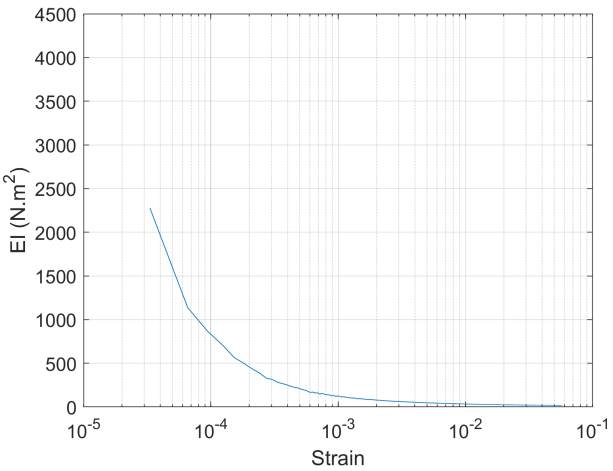

(b) experiment 5

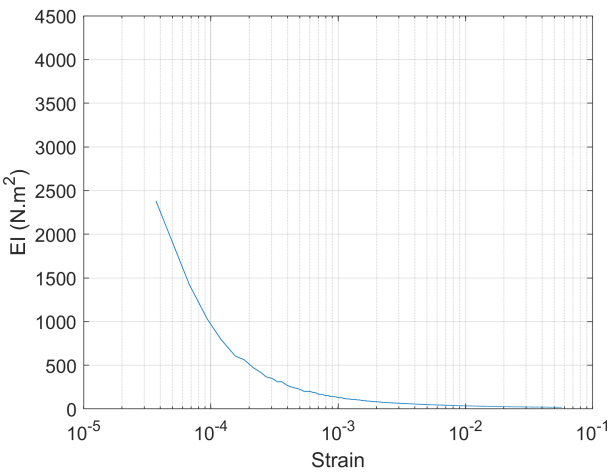

(c) experiment 6

Figure 4.18. EI-strain curve for experiments 4, 5 and 6 in group 2.

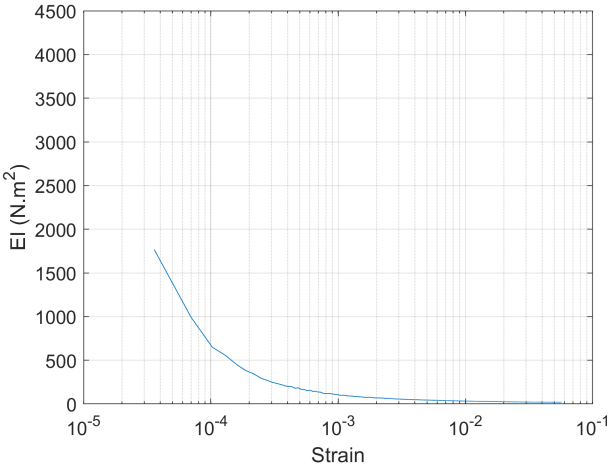

(a) experiment 7

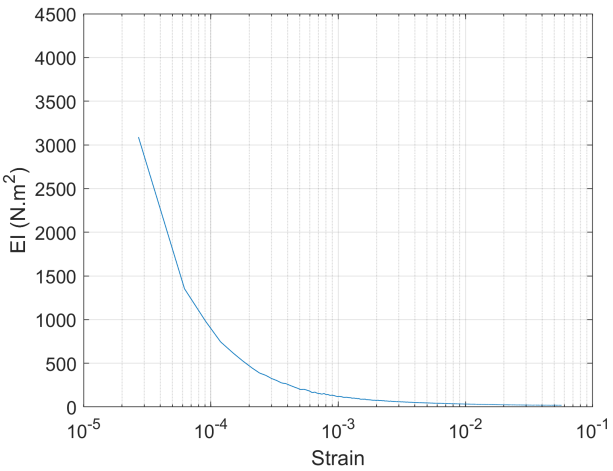

(b) experiment 8

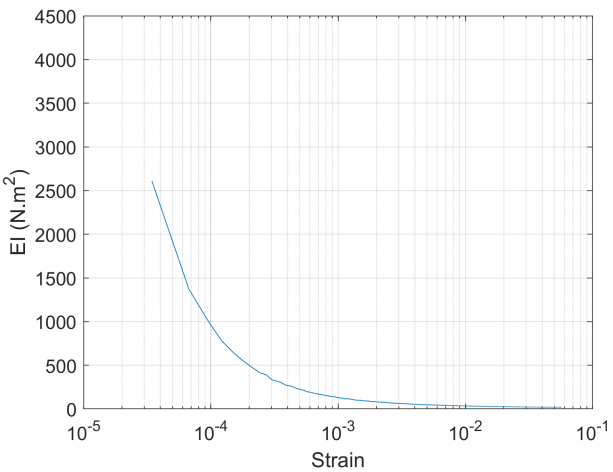

(c) experiment 9

Figure 4.19. EI-strain curve for experiments 7, 8 and 9 in group 2.

It means that a block coincides with the lower block either at the right or left point and turns around a certain degree.

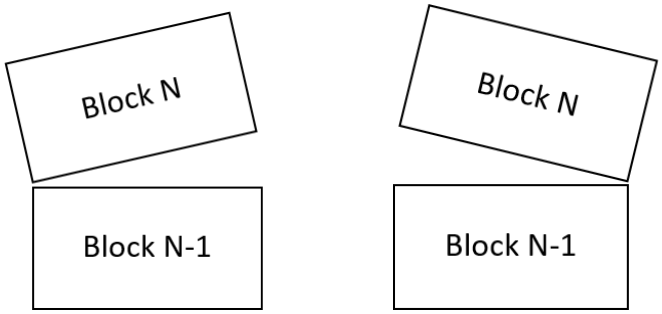

(a) if the degree is positive (b) if the degree is negative

Figure 4.20. Assumption to estimate the deflection.

To estimate the deflection, the MATLAB plot function was used. After deciding the rotating point based on the assumption mentioned above, the rectangle block was rotated with the angle obtained from IMU- around that point. After all the blocks plotted, the selected block's deflection was calculated using the difference between the x-coordinate of the right bottom of the selected rectangular block and the support. The following results are taken from experiment 6, experiment 7, experiment 8, and experiment 9 at the specified deflections (0.5, 1.00, 1.50, and 2.00 cm). The blue values on the following charts denotes for the real-deflection obtained from external LVDTs, while the red values beside each block denotes for estimated deflection.

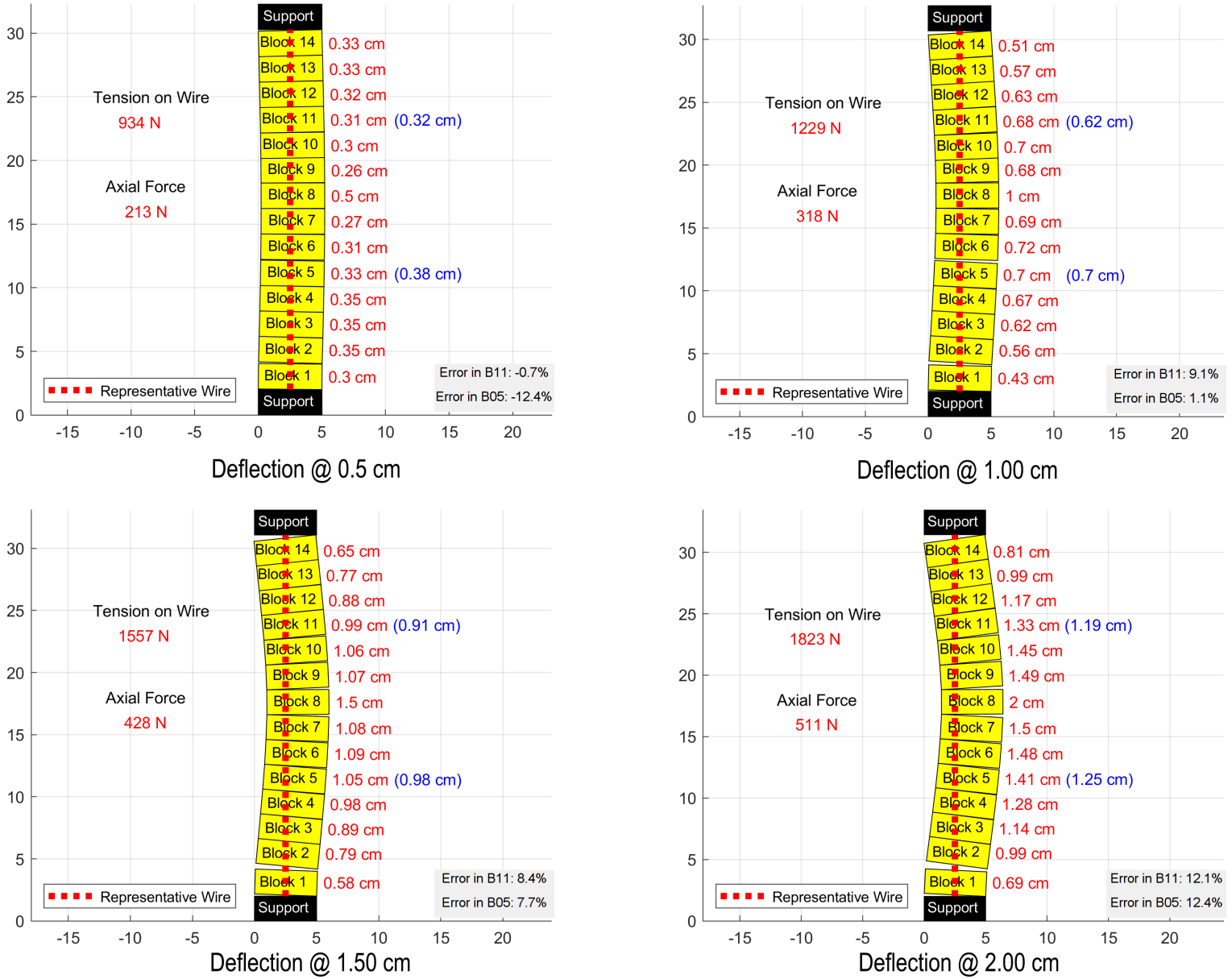

Figure 4.21. Estimation of deflection in blocks using the proposed algorithm in experiment 6.

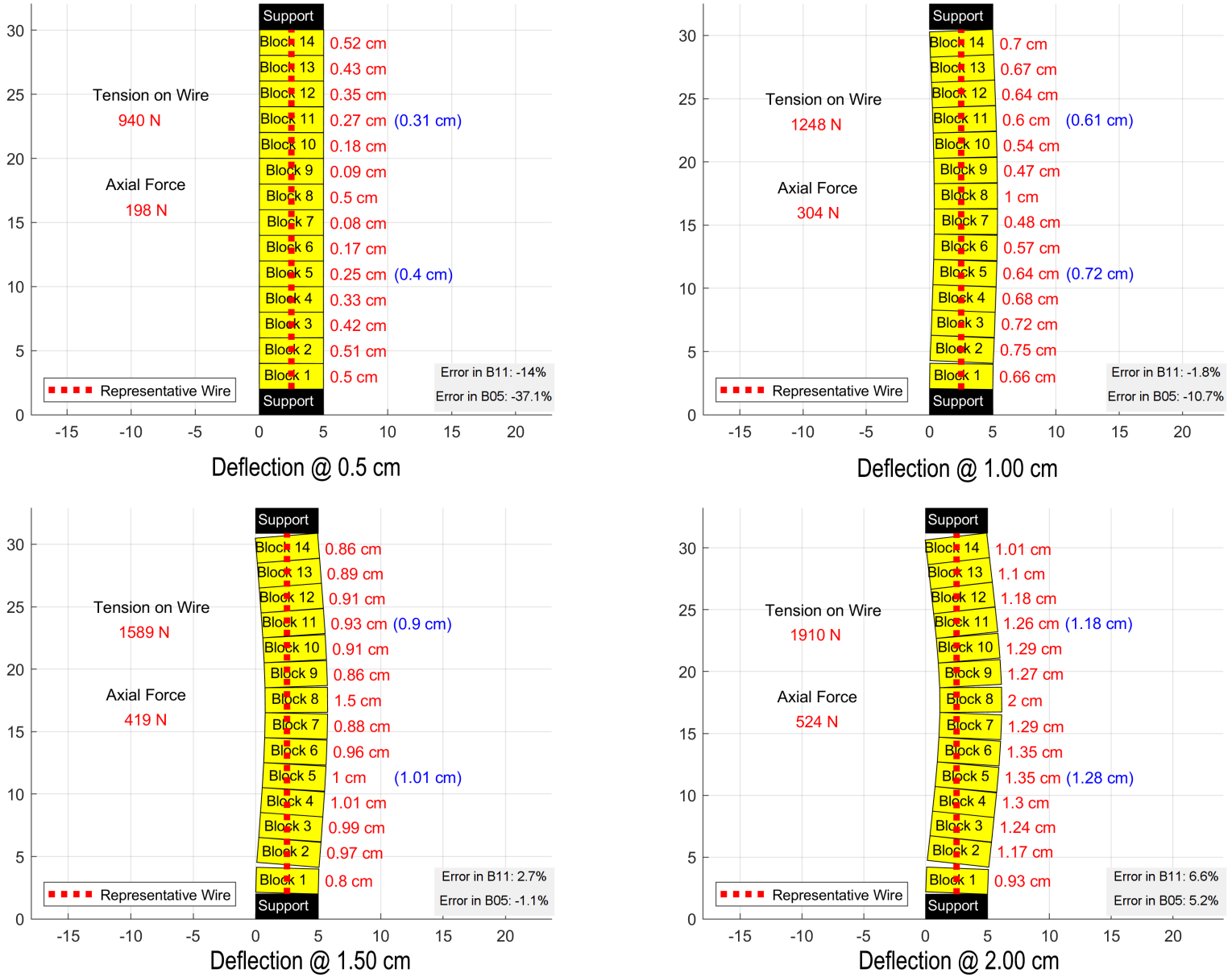

Figure 4.22. Estimation of deflection in blocks using the proposed algorithm in experiment 7.

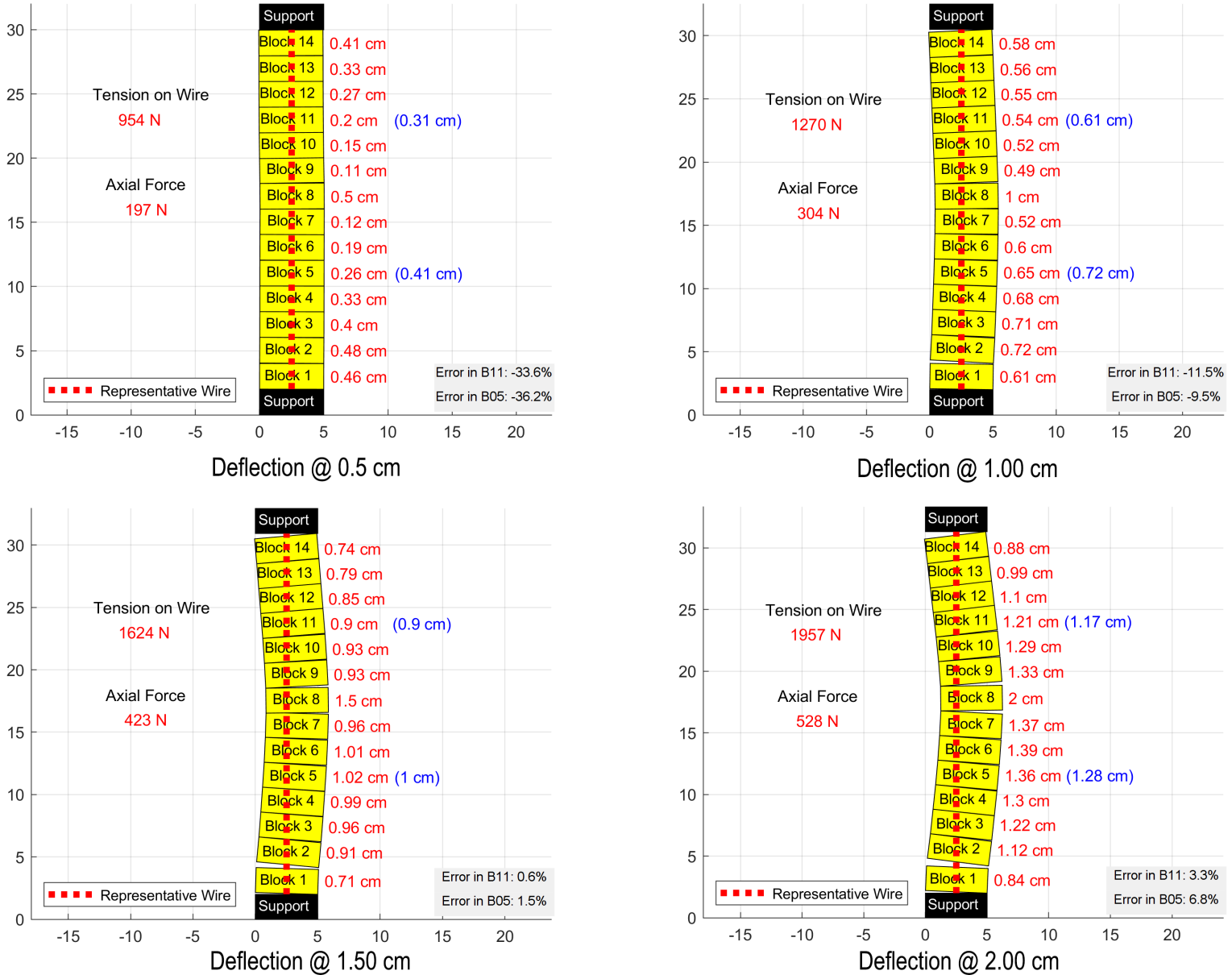

Figure 4.23. Estimation of deflection in blocks using the proposed algorithm in experiment 8.

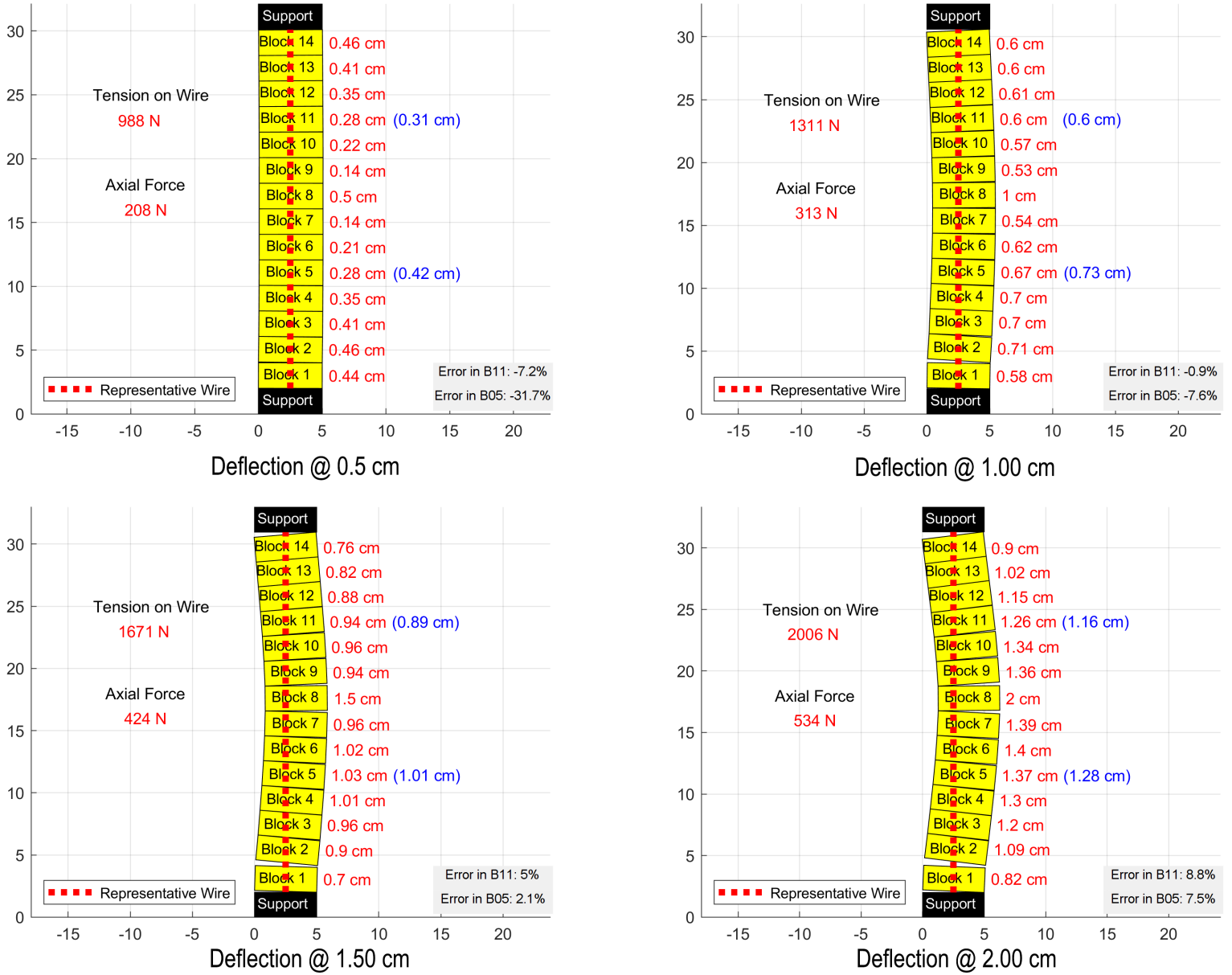

Figure 4.24. Estimation of deflection in blocks using the proposed algorithm in experiment 9.

5. DISCUSSION

5.1. Stress Measurement and Mapping Techniques

5.1.1. Stress Measurement Using Stress Transducer Enclosed in Pacifier

A 500 kPa miniature pressure transducer is modified to be able to be used with soil particles. The manufacturer recommends using the transducer in liquids such as water or oil, meaning that the sensor requires continuous uniform pressure for successful measurements. In this part of the study, the transducer was placed into a silicone pacifier, filled with de-aired and distilled water, and then sealed with a water-proof industrial glue called Sugru. The idea behind this modification is that when pressure is applied to the silicone pacifier, the inside water pressure will increase, and the transducer in the pacifier will measure the change.

To examine the pattern, the modified pacifier was loaded to 2 kPa, 4 kPa, 8 kPa, 16 kPa, 32 kPa, 50 kPa, and 75 kPa, consequently and then mV/V values were recorded. These experiments were performed in four groups A, B, C, and D and each group of the test was held on different dates. The weather and laboratory conditions for each date are listed in Table 5.1. The obtained mV/V vs. pressure values plotted in Figure 5.1, 5.2, 5.3, and 5.4 for group A, B, C and D, respectively.

Table 5.1. Humidity, temperature and pressure values for groups of experiments

Group	**Lab. Humidity (%)**	**Lab. Temperature (°C)**	**Pressure (hPa)**
Group A	32	26	1014
Group B	33	25	1009
Group C	35	27	1020
Group D	34	27	1018

As shown in Figure 5.1 to Figure 5.4, it is clear that the first experiment in all four groups diverges from the other experiments in the same group. Even though the transducer was placed into the pacifier meticulously and the water inside was de-aired and distilled water, there may be a tiny air bubble left inside. It is another possibility that the glue which was used to seal the transducer inside the pacifier, was not able to hold the water inside and a part of water may have leaked. Although water loss inside the pacifier was not seen during these experiments, it is observed that after a few months the water level is lowered. It maybe due to the poor performance of the glue that was used which could not seal the pacifier properly or the water diffused from the silicon; hence led to the error.

If a tiny air bubble was left inside, it moderately explains the behavior of the first experiments in each group. After the first experiment done, since the pacifier was already exposed to a load up to 75 kPa, the air bubble inside would be dissolved due to high pressure. This proposition can be supported by comparing overall, and first-experiment deducted root mean square error (RMSE) and R^2 values for Group A in Figure 5.7 and Figure 5.8, Group C in Figure 5.10 and Figure 5.11 and Group D in Figure 5.12 and Figure 5.13. Although each of these experiments are coherent inside if the first experiments are ignored, the beginning and final millivolt-per-volt values still do not match with other groups. Also; considering that air bubbles dissolve in water at a pressure of 200 kPa and above, it seems to be a weak possibility to dissolve under 75 kPa. Therefore, it can be concluded that either the way of application in this study or the characteristics of the silicon or glue material has led to the error, and it is not suitable to use under pressure. The calculated root mean square errors for each group of experiments are shown in Table 5.2, 5.3, 5.4 and 5.5.

5.1.2. Stress Mapping Using Prescaled Films

5LW type prescaled stress films (able to record pressure between 5 kPa to 50 kPa) used to measure lateral earth pressure exerted on the segmental pile. A total of three experiments were performed.

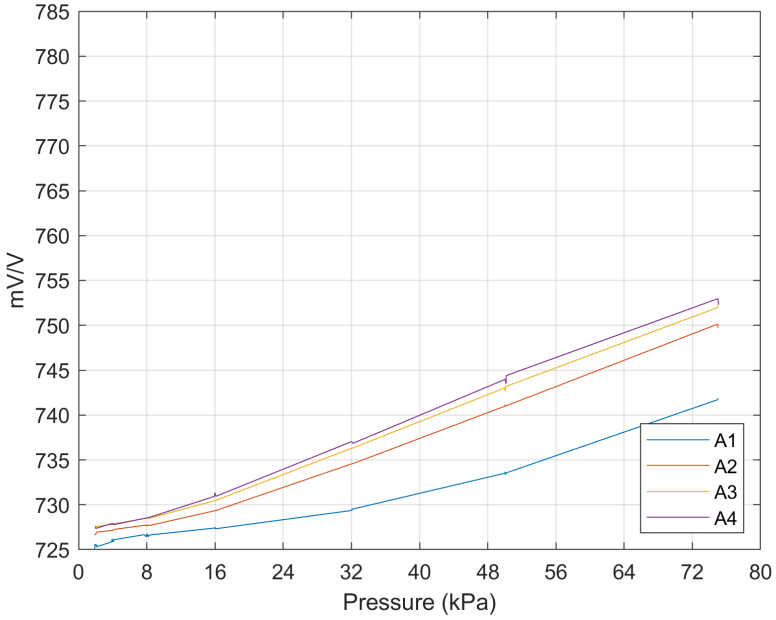

Figure 5.1. Pressure vs. mv/v values from experiment group a.

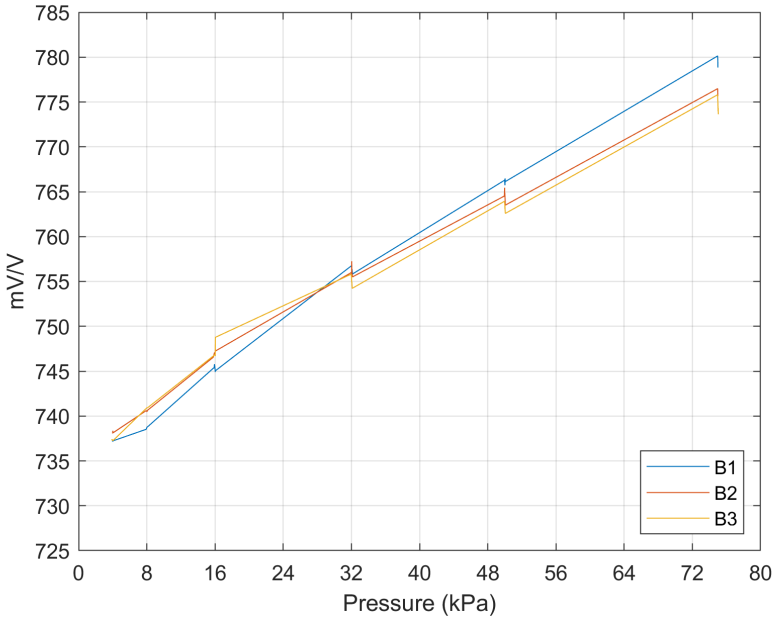

Figure 5.2. Pressure vs. mv/v values from experiment group b.

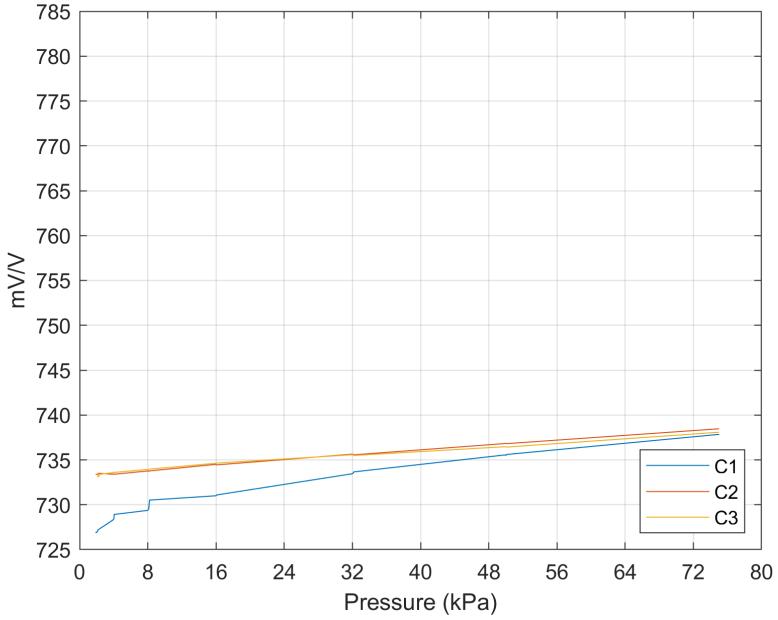

Figure 5.3. Pressure vs. mv/v values from experiment group c.

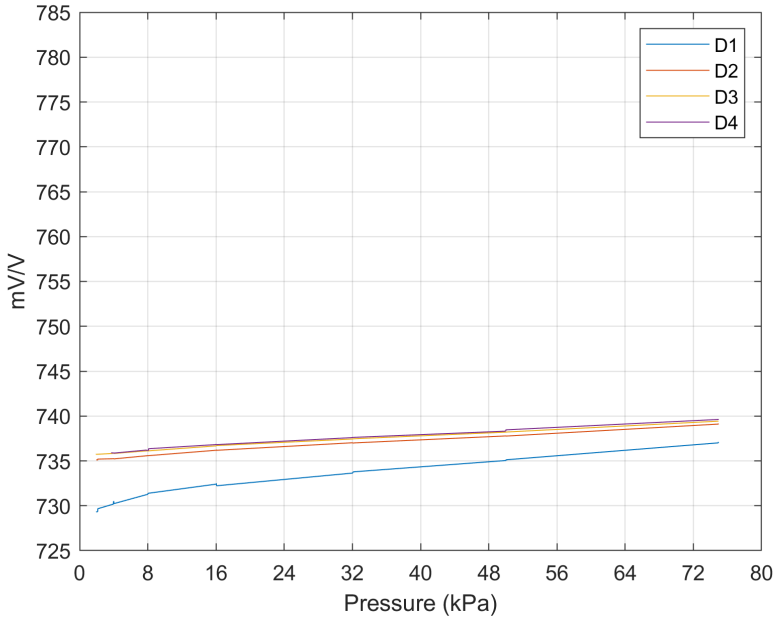

Figure 5.4. Pressure vs. mv/v values from experiment group d.

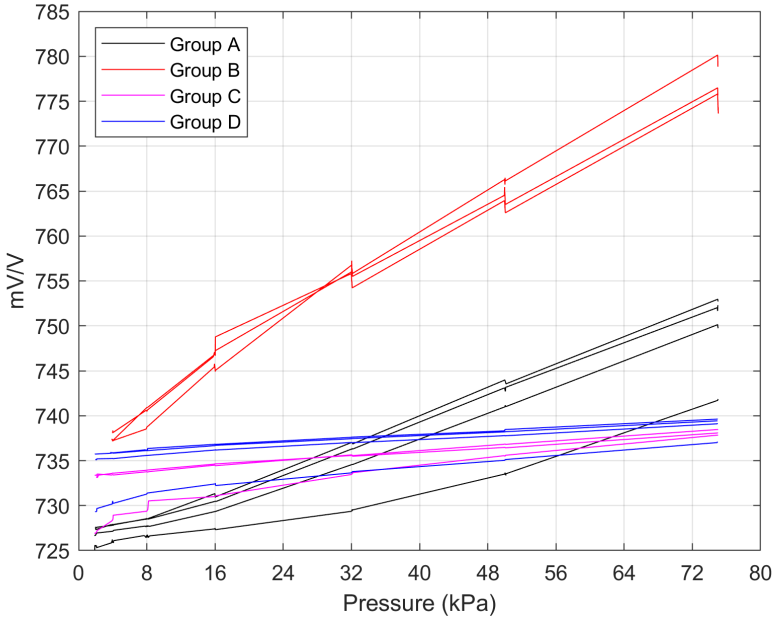

Figure 5.5. Merged results from all pacifier experiments.

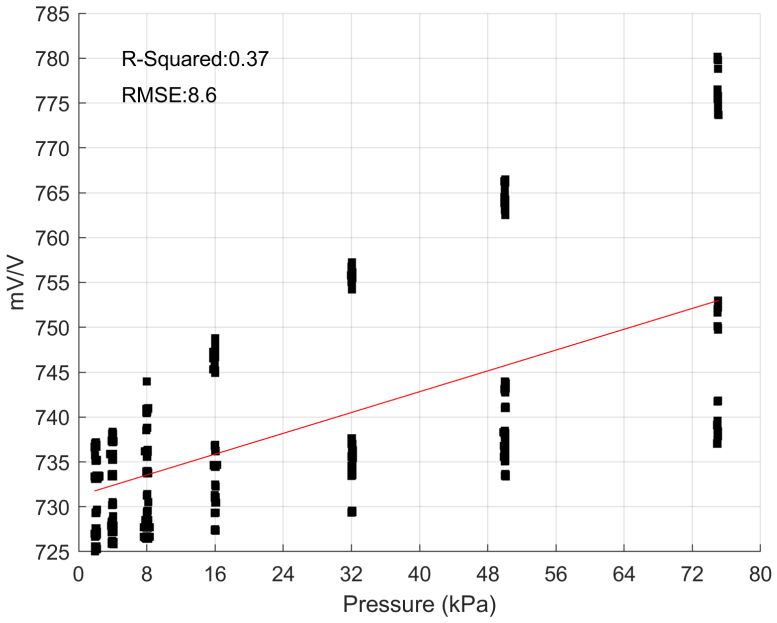

Figure 5.6. Linear fit of all pacifier experiments.

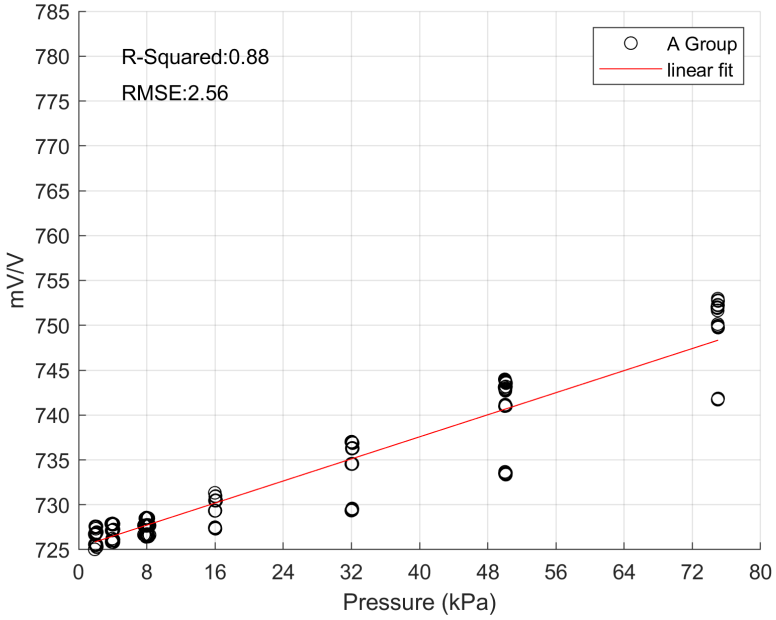

Figure 5.7. Linear fit of group a (a1, a2, a3, a4) experiments.

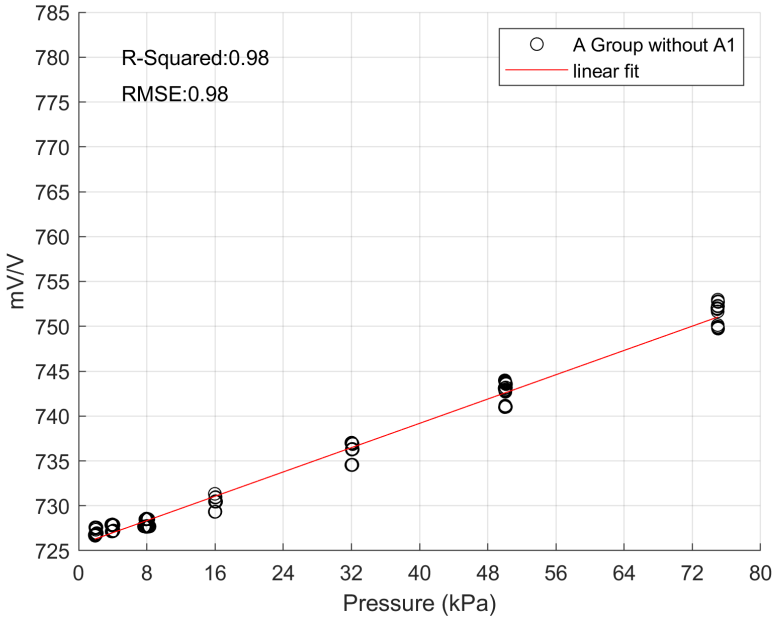

Figure 5.8. Linear fit of group a without a1 (a2, a3, a4) experiments.

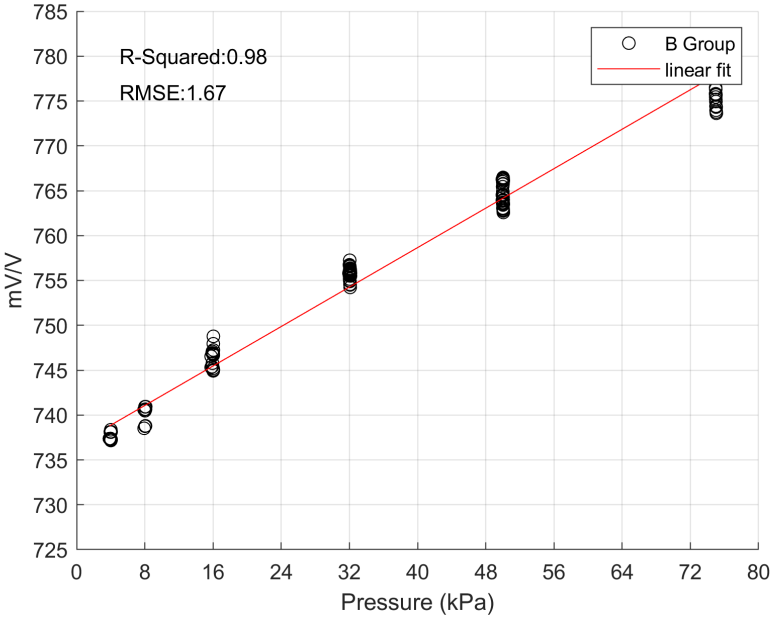

Figure 5.9. Linear fit of group b (b1, b2, b3) experiments.

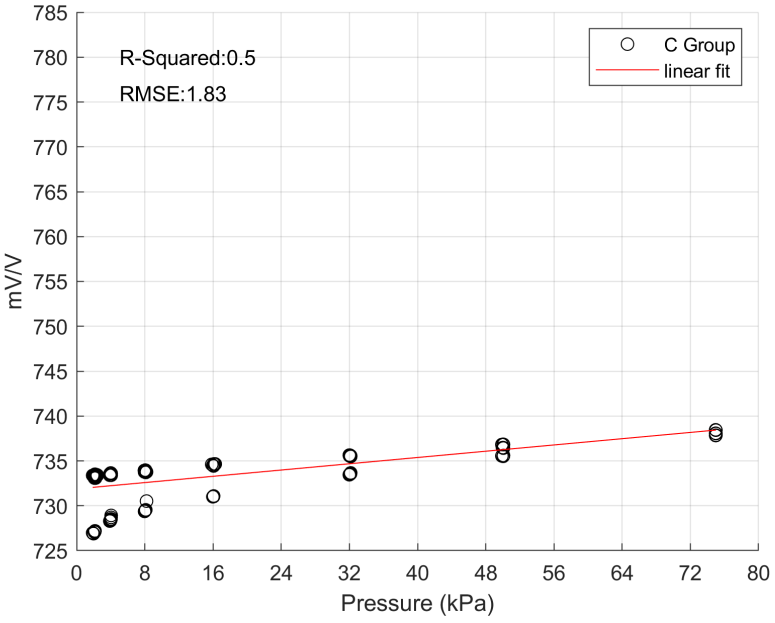

Figure 5.10. Linear fit of group c (c1, c2, c3) experiments.

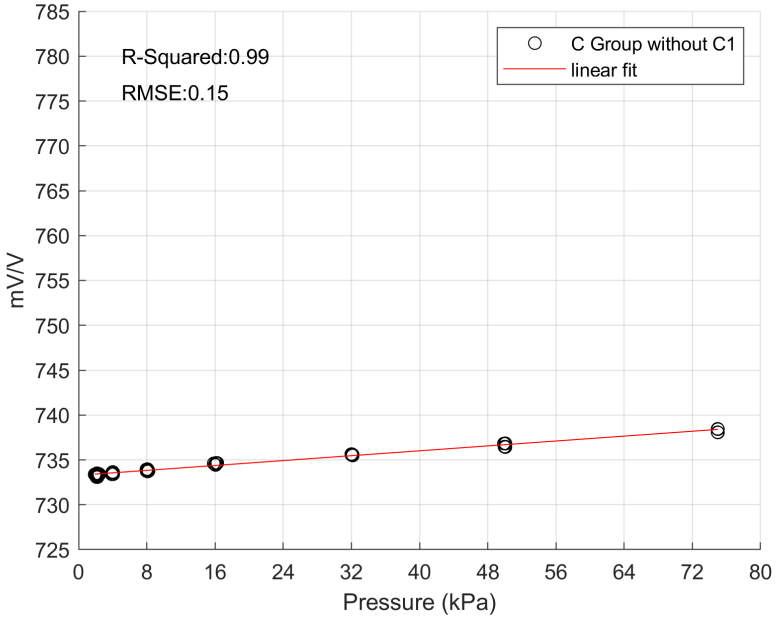

Figure 5.11. Linear fit of group c without c1 (c2 and c3) experiments.

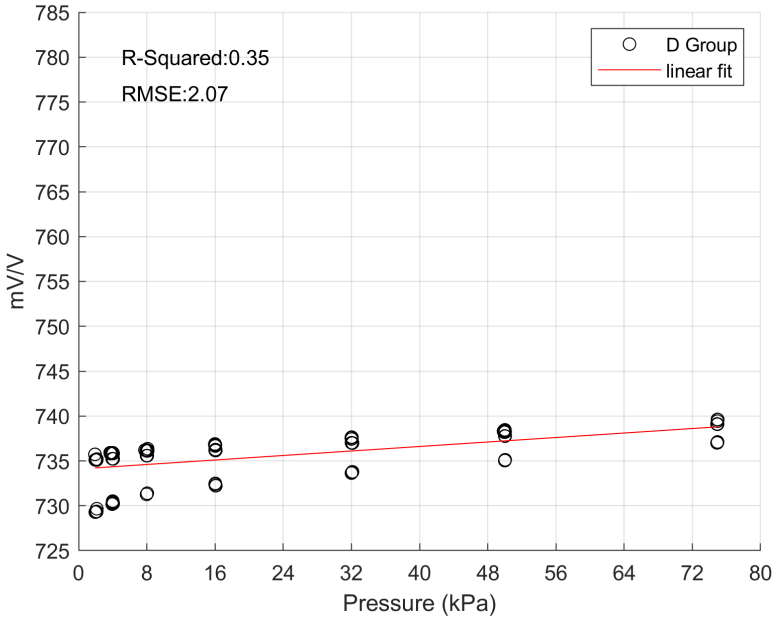

Figure 5.12. Linear fit of group d (d1, d2, d3, d4) experiments.

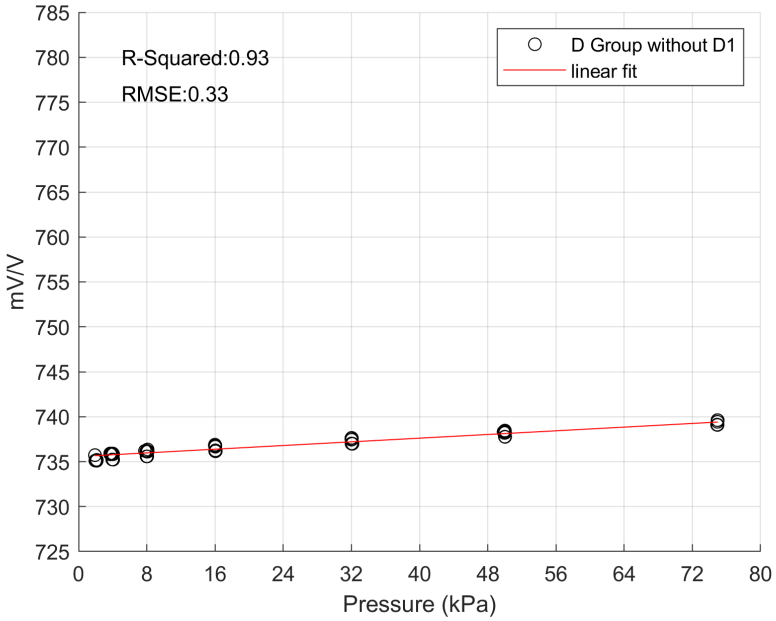

Figure 5.13. Linear fit of group d without d1 (d2, d3, d4) experiments.

Table 5.2. Root mean square error (rmse) in group a.

Experiment A#	**A1**	**A2**	**A3**	**A4**
A1	-	4.21	5.93	7.13
A2	4.21	-	1.32	2.05
A3	5.93	1.32	-	0.57
A4	7.13	2.05	0.57	-

Table 5.3. Root mean square error (rmse) in group b.

Experiment B#	**B1**	**B2**	**B3**
B1	-	1.71	2.55
B2	1.71	-	0.89
B3	2.55	0.89	-

Table 5.4. Root mean square error (rmse) in group c.

Experiment C#	**C1**	**C2**	**C3**
C1	-	3.87	4.38
C2	3.87	-	0.24
C3	4.38	0.24	-

Table 5.5. Root mean square error (rmse) in group d.

Experiment D#	**D1**	**D2**	**D3**	**D4**
D1	-	4.13	4.13	4.51
D2	4.13	-	0.52	0.60
D3	4.13	0.52	-	0.13
D4	4.51	0.60	0.13	-

In all three experiments, the cable tension of the segmental pile was set to 750 N, and the upper box of the machine where the pile head is fixed on, was allowed to displace up to 5 cm with a rate of 1 mm per minute. The stress films were placed on the front face of 6 concrete blocks in the direction of movement. The tension of the cable was verified using a load-cell that is placed between two of the blocks. After the experiments are done, the prescaled films were removed carefully and were analyzed using the dedicated software.

The raw and processed images obtained from the dedicated software is shown in Figure 5.14 and Figure 5.15. The green areas on these images denote for pressures less than 5 kPa, and no yellow regions are present on them, meaning that no pressure was recorded above 50 kPa.

In Figure 5.15, although there are a few green areas, it can be noticed that almost all the regions are in red shade.

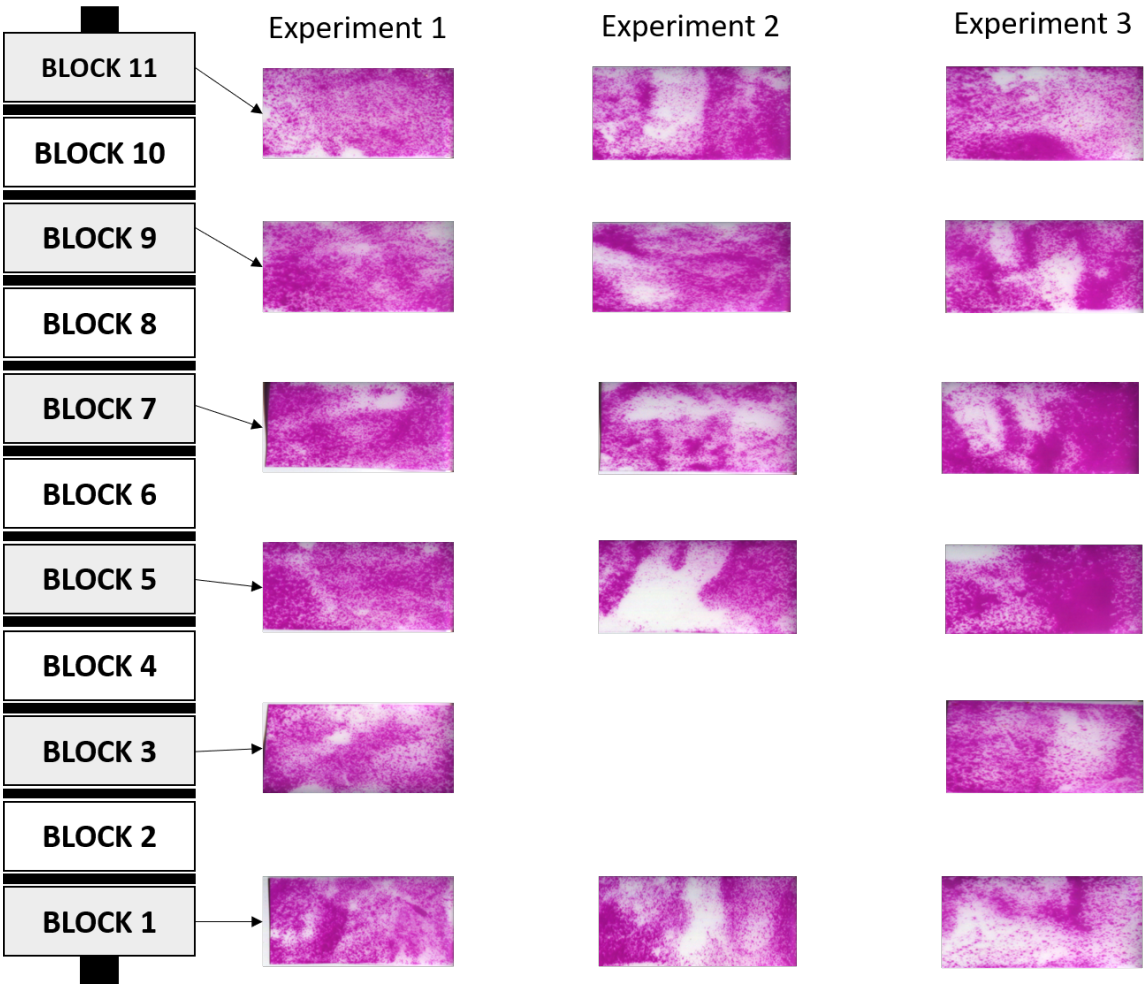

Figure 5.14. Raw images of prescaled films.

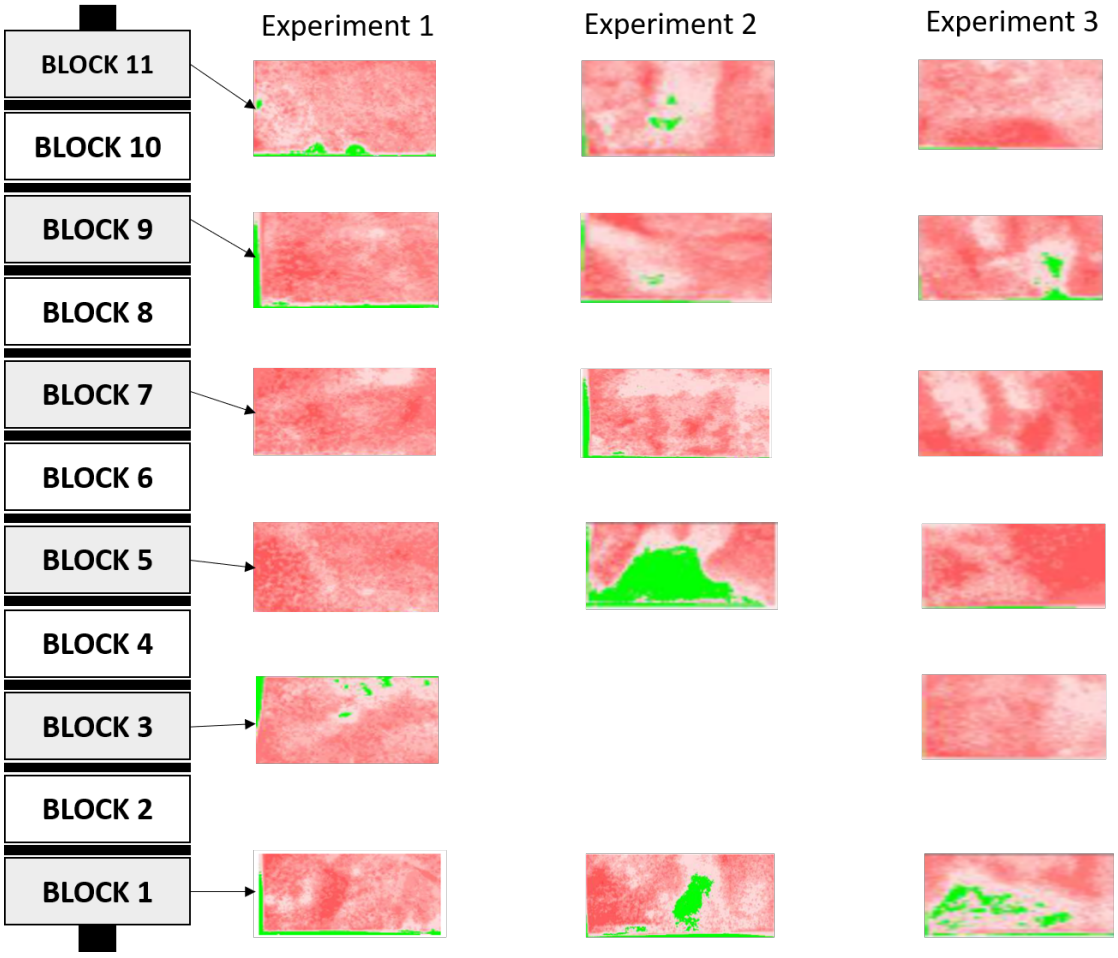

Figure 5.15. Processed images of prescaled films.

It means that the exerted lateral pressure during the experiments are between 5 kPa and 50 kPa. The green areas indicate that no pressure was received in the present area. These sensitive stress films require perfect alignment of the dull sides of both A and C films. Since the segmental pile was embedded in the soil, a solution has been developed to prevent sand particles from getting in between the sheets. After sheets were aligned with each other, both ends were fixed using staples, and finally, they were placed inside a sheet protector, as shown in Figure 5.16. These green areas could be the result of not well-stretched sheet covers. The detailed breakdown of pressure distributions are presented in Table 4.5, Table 4.6, and Table 4.7 for experiments 1, 2 and 3, respectively. Almost half of the pressed area corresponds to an average of 26 kPa and a maximum of 28 kPa pressure.

Figure 5.16. Stress film inside sheet cover.

The lateral load on the segmental pile is measured as 350 N, which is the maximum value shown in Figure 4.6. This is the load experienced by the pile's front face, which corresponds to 125 cm^2 area, in the movement direction. Employing the relation between load and area, laterally exerted pressure on the segmental pile can be calculated as 28 kPa. However, it should be considered that the horizontal load of 350 N also includes frictional forces. Hence, by considering the effect of friction, it can be said that the real pressure on the segmental pile should be less than 28 kPa. It is clear that the average and maximum pressure value, 26 kPa, and 28 kPa, obtained from prescaled films, are close to the above-calculated value.

5.2. Deflection Measurement Techniques

5.2.1. Estimation of Deflection Using Proposed Algorithm

An IMU sensor was attached to each concrete block of the segmental pile and data from the accelerometer, magnetometer, and gyroscope was processed using the sensor fusion to estimate each block's deflection in real-time. Each of the accelerometer, magnetometer, and gyroscope inside the IMU chip calibrated by means of several methods.

For the magnetometer's calibration, the sensor was placed into the center of a cube and rotated freely by hand to obtain x, y, and z data points. This data were then filtered to clean the same data points and then were used to construct the sensor's domain. Subsequently, using MATLAB's magcal() function, the transformation and bias matrices obtained to transform the shape of this sensor's domain into a perfect sphere. Similarly, the accelerometer was calibrated using the same cube-method. The cube was placed as the z-axis point upward/downward, x-axis point upward/downward, and y-axis point upward/downward, and then obtained data was used to calculate the scale factor and offset of each sensor. The calibration of the gyroscope sensor was comparatively straight forward than the others. The sensor placed on the flat surface and obtained data used to calculate drift values in x,y, and z-axes.

After all the calibration processes completed for each sensor, each was attached to per concrete block on the segmental pile. The data were collected through the Arduino board and processed in MATLAB to obtain the degree of changes in all axes. Using the inclination angles of blocks, the deflection was estimated. The estimated deflection was verified through externally placed LVDT's on Block 5, and Block 11. The change of percent error in Block 5, and Block 11 is shown in Figure 5.17, and 5.18, respectively. The percent error in both blocks starts with ± 60%, and after the deflection reached approximately 1 mm, start to decrease swiftly and stabilized within the range of ± 10% percent error.

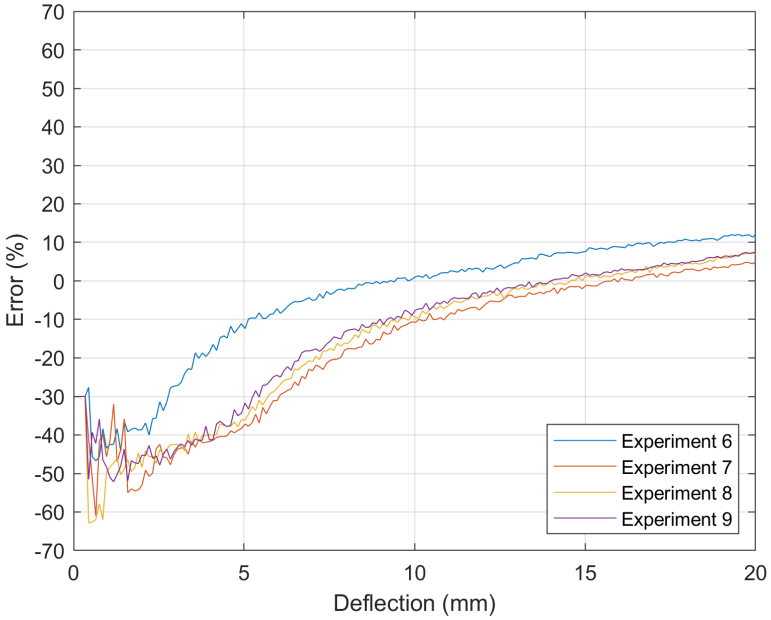

Figure 5.17. Change of percent error in block 5.

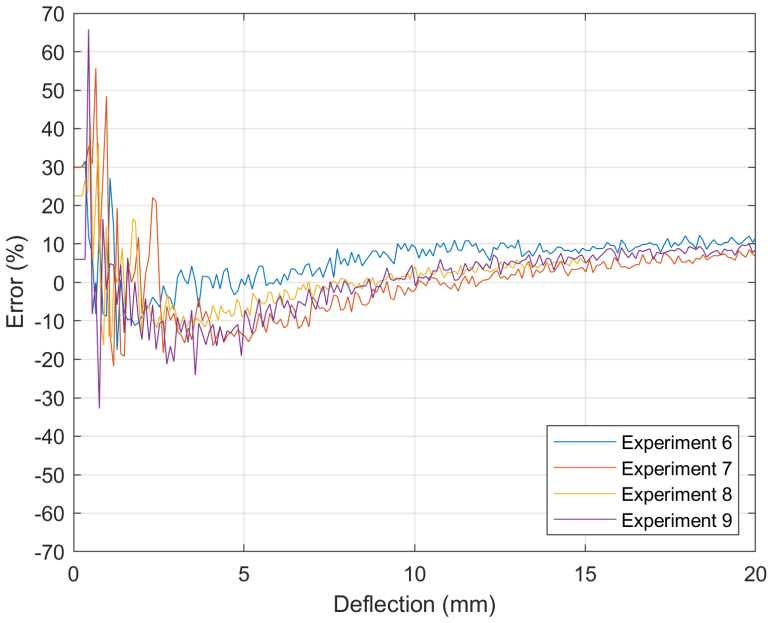

Figure 5.18. Change of percent error in block 11.

It should also be considered that the anchor cable passing through the segmental pile creates a magnetic distortion, resulting in mismeasurements of the sensors. The error in both blocks approaches the zero at approximately 0.7 cm deflection and then increases slightly by the end of the experiment. Once the anchor cable reached the boundary of the hole (10 mm) start to prevent the movement of blocks; thus, the error increases. It can also be seen in the change of cable's tension in Figure 5.19. Since the experiments were held in consecutive order, after the first two experiments, the initial value of wire tension looks almost stabilized for the rest of the experiments.

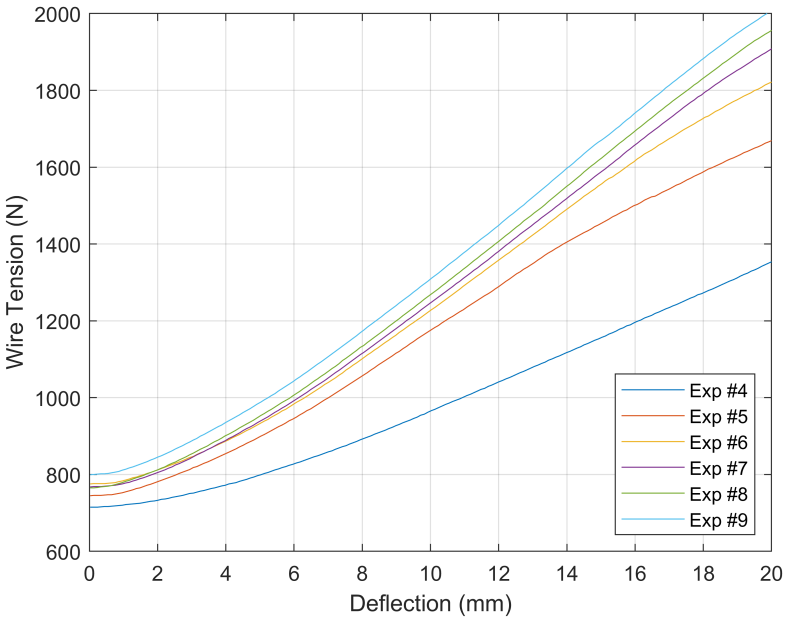

Figure 5.19. Wire tension vs. deflection chart.

5.2.2. Flexural Rigidity of Segmental Pile

The flexural rigidity of the segmental pile is examined using three-point bending test results, and EI is determined. These experiments were held in two different piles. The first group of experiments (a total of 3 experiments) were performed using a segmental pile consisting of 13 concrete blocks. The second group of experiments (a total of 6 experiments) were conducted using a segmental pile composed of 14 concrete blocks and two external LVDTs placed on block 5 and block 11.

In all of the experiments, the segmental pile was post-tensioned to 750 N.

The failure of the segmental pile occurred at the point where the flexural stress is 1 MPa and the strain is 0.45, in experiment 1. Similarly, the failure happened in experiment 2 when the flexural stress is 1.1 MPa and strain is 0.05. For experiment 3, it fails when flexural stress is 0.7 MPa and strain is equal to 0.03, as shown in Figure 5.20. Also, it is noteworthy that while all three experiments end up with similar flexural strain values, flexural stress values show an increasing trend.

The flexural strain peak in the first experiment is 1.08 MPa increased to approximately 1.16 MPa in experiments 2 and 3. This pattern indicates that the segmental pile was completing a rearrangement process in the first few experiments.

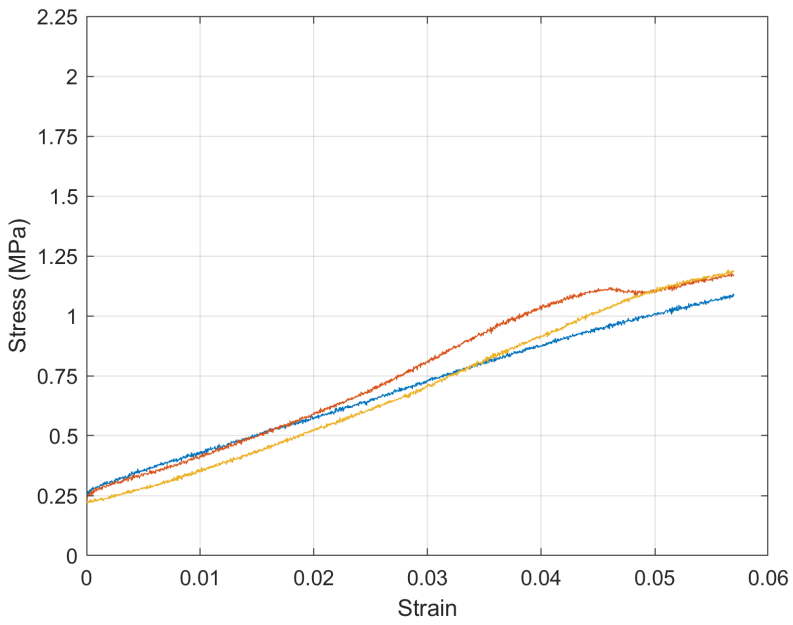

Figure 5.20. Stress-strain curve for group 1 experiments.

In the second group of experiments, this rearrangement process is noticed more clearly. While all six experiments ended up with 0.057 flexural strain, the flexural stress values increased in the first three experiments and stabilized for the rest. The main reason for this behavior is the structure of the segmental pile.

As mentioned beforehand, the anchor cable, which is passing through each element of the segmental pile, was centered at the beginning of the experiments. After the loading and unloading process completed in the first three-point bending test, the post-tension adjusted again as 750 N, and the next experiment initiated consecutively. Hence, in the first three of these experiments, the anchor cable was free, meaning no physical contact with any of these blocks. It explains the fact shown in Figure 5.21, the flexural stress is increased due to the anchor cable reached the limit (diameter of the hole) and started to hold the pile.

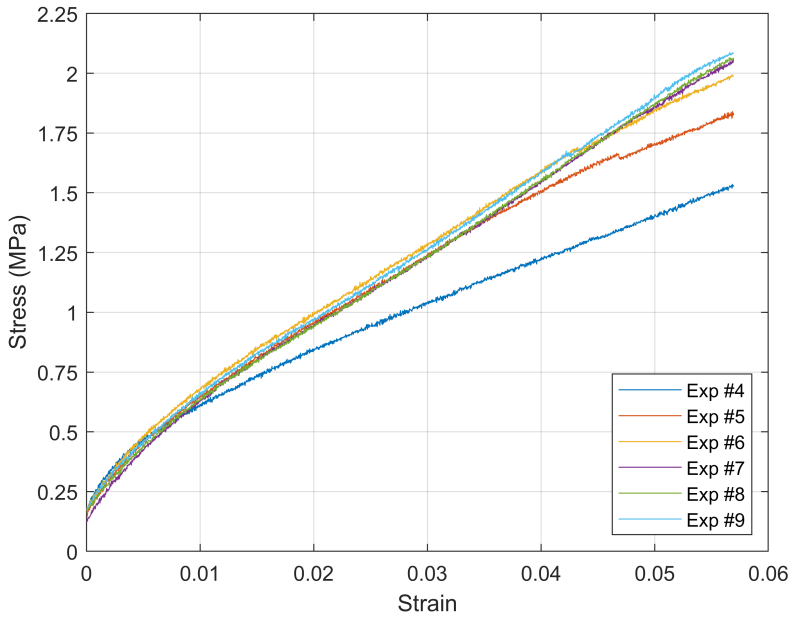

Figure 5.21. Stress-strain curve for group 2 experiments.

In order to determine the flexural rigidity of the segmental pile, the following general deflection equation was used. It should be noted that this equation assumes that the pile is continuous; therefore, it does not consider the segmental structure of this pile.

$$\delta = \frac{PL^3}{48EI} \tag{5.1}$$

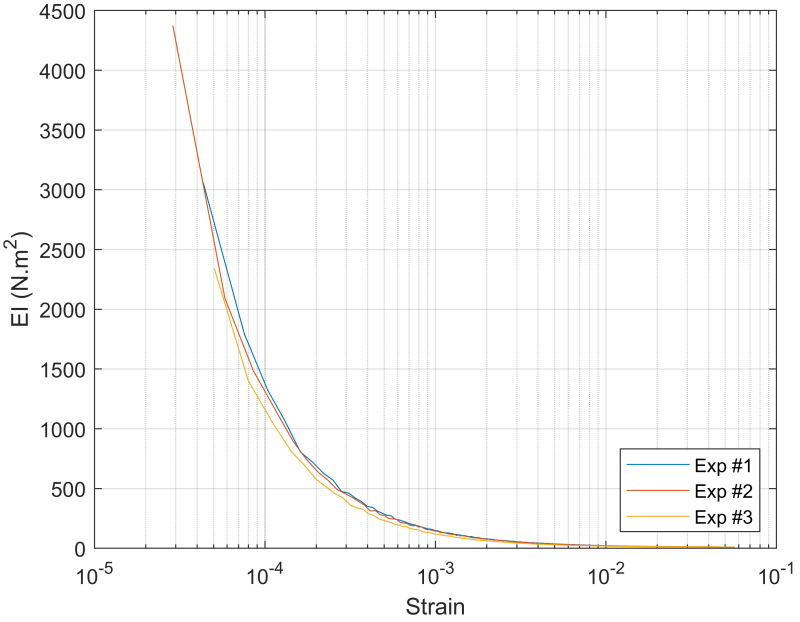

Figure 5.22. EI-strain curve for group 1 experiments.

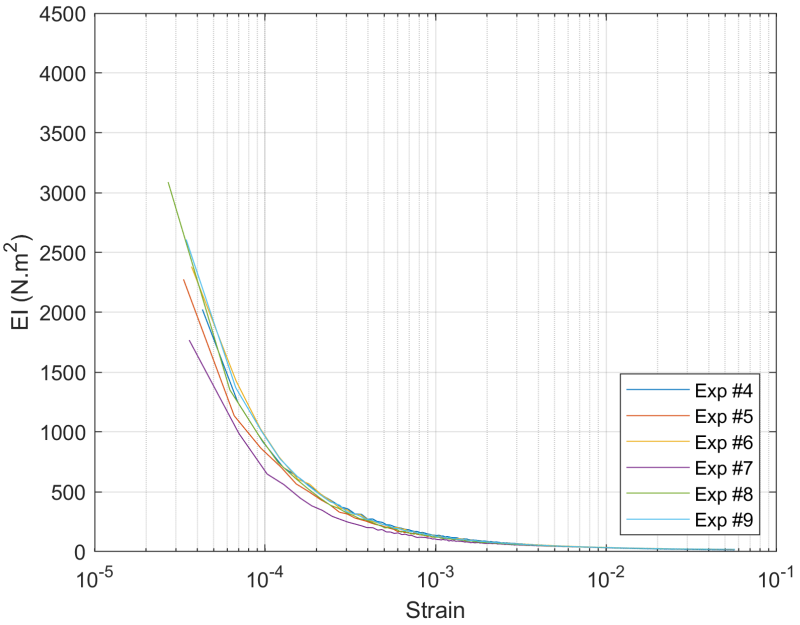

Figure 5.23. EI-strain curve for group 2 experiments.

Table 5.6. Numerical values for flexural rigidity of the segmental pile.

Force, P (N)	**Deflection, δ (mm)**	**Beam Length, L (mm)**	**EI ($N.m^2$)**
Experiment 5			
198.58	5.00	325.00	28.38
306.53	10.00	325.00	21.91
400.60	15.00	325.00	19.09
Experiment 6			
210.26	5.00	325.00	30.05
316.82	10.00	325.00	22.65
426.77	15.00	325.00	20.34
Experiment 7			
196.29	5.00	325.00	28.05
304.22	10.00	325.00	21.74
417.61	15.00	325.00	19.90
Experiment 8			
198.09	5.00	325.00	28.32
305.90	10.00	325.00	21.87
420.13	15.00	325.00	20.03
Experiment 9			
204.74	5.00	325.00	29.26
311.31	10.00	325.00	22.26
424.15	15.00	325.00	20.22
$\boldsymbol{EI_{average}}$			**23.60**

The numerical values regarding the flexural rigidity of the segmental pile are presented in Table 5.6. The $EI_{average}$ for the segmental pile with the assumption that it is continuous, was determined as 23.60 $N.m^2$. In the previous studies, the flexural rigidity of the concrete mortar beam and the segmental pile examined at 750 N, 1500 N, and 2250 N.

As expected, the determined EI value is much less than the mortar concrete beam since the segmental piles' flexible structure, as shown in previous studies from (Yahia, 2014) on Figure 5.24, and from (Sengez, 2019) on Figure 5.25.

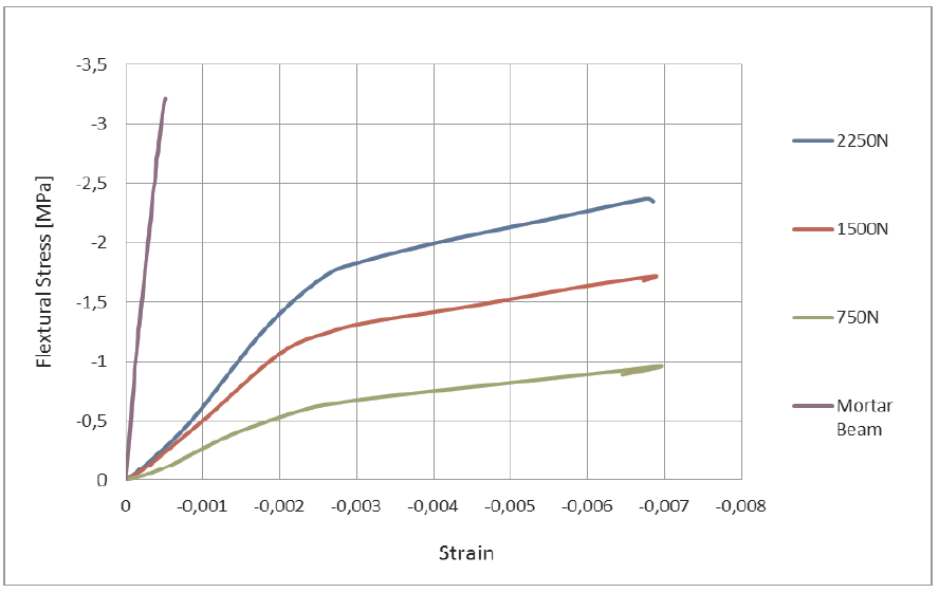

Figure 5.24. Stress-strain curve from Yahia [19].

5.2.3. Inclination Angles

The deflection estimation is based on the degree of change in the z-axis in the proposed algorithm. It was also observed that some blocks are rotating around as much as 5 to 7 degrees in the x-axis. The peak point of the y-degree was reached at the middle point. This behavior can be explained with the following. Since the load was applied through the middle of the pile in the three-point bending experiment, the loading unit could be forced the block to rotate around itself. Once the blocks at the middle twisted, the connected blocks effected, but due to friction between the blocks and the rubber, this rotation force absorbed, and the degree of change in the x-axis decreased as getting away from the middle.

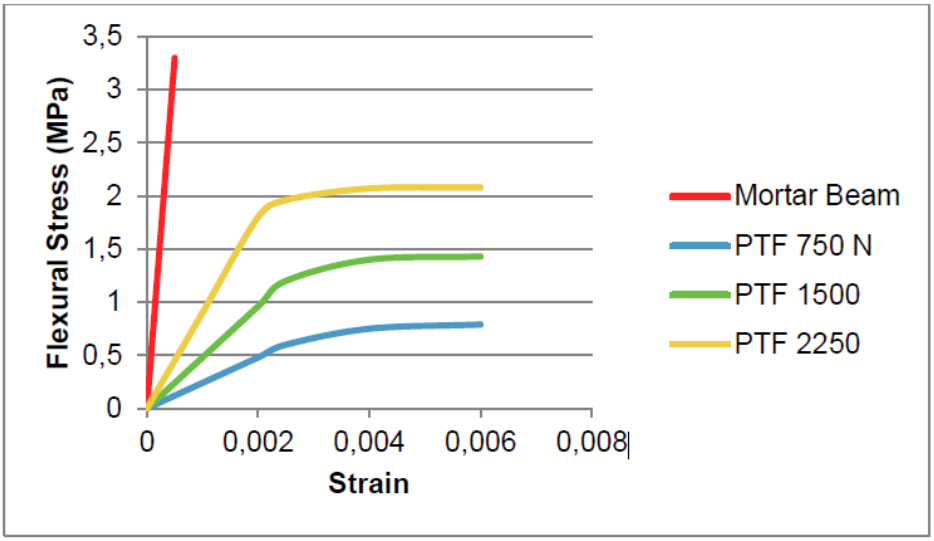

Figure 5.25. Stress-strain curve from Sengez [20].

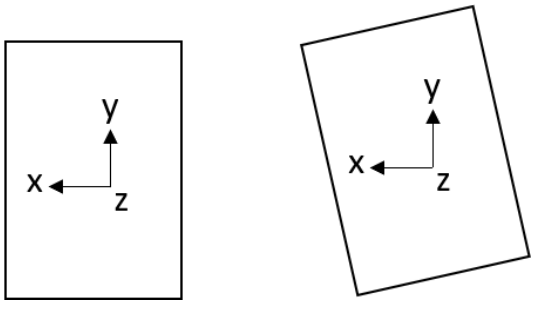

Figure 5.26. Position 1 (at left), position 2 (at right).

6. CONCLUSIONS

Stress and displacement measurements have critical importance to model the behavior of the soil. Although a wide range of techniques are available in the literature, none of them guarantees robust measurements due to the heterogenetic and anisotropic nature of the soil. This problem creates a significant challenge for the researchers to plan the equipment and, consequently, the budget needed for their research. The use of costly sensors with a high-end data acquisition board may be seen as a reliable way to obtain measurements at a single point. However, considering a constant state of flux behavior of the soil, which highly depends on the location of the sample taken, and orientation of the measurement, it is clear that measurements from multiple points are needed to understand the overall response. Using cost-effective, large number of low-end sensors with an open platform data acquisition board may help researchers to obtain measurements from multiple data points to reveal relative changes. This study demonstrated that the combination of different measurement methods has the potential to satisfy several of them.

The IMU chips consist of an accelerometer, magnetometer, and gyroscope which can measure an object's degree of change of motion in all axes are used. IMUs are connected to the open platform Arduino board for data acquisition purposes, and the obtained data are processed with MATLAB's sensor fusion algorithms. This study has shown that by measuring inclination of each block of the segmental pile, the deflection of the pile can be calculated.

Prescaled sensitive films also have the potential as a stress measurement technique in geotechnical applications. It is shown that prescaled films are a strong candidate among other methods to measure the average stress value and to visualize the overall stress distribution within the soil. These films are placed on the segmental pile's front face, and the lateral pressure exerted on the pile is measured.

It was observed that the obtained values match with the expected lateral load, which was calculated using the relation between the measured force and the area of the front side of the pile.

A miniature pressure transducer which was designed to operate in the fluid medium is modified in order to be used in the soil. The transducer was placed in a silicone pacifier, which is then filled with de-aired and distilled water, and it was sealed. Several measurements were made on different dates. The first pressure measurement on each day was an outlier. Consecutive measurements gave reliable results. Measurements at different dates shared similar trend; however the pressure value measured at different dates were not repeatable. One reason for this maybe the selection of the wrong sealing glue.

Overall, each of these methods used has different advantages and disadvantages. The use of a high-end data acquisition board has an advantage over an open-platform Arduino board that the sampling rate could be adjusted, such as low-resolution speed sampling and high-resolution slow sampling, according to the purpose of the study. The high-end data acquisition board used in this study could sample up to 100MHz, while the low-end board supports sampling up to 20 MHz. On the other hand, it is clear that by using cost-effective IMUs at multiple points, the relative deflection at all desired points can be determined without requiring expensive LVDT's if the $\pm 10\%$ error margin is reasonable for the purpose. Hybrid utilization of various level sensors may be the optimal solution in terms of cost-effectiveness and to achieve reliable and robust measurements. Considering the fact that the cheap IMU sensors used in the smartphones can achieve high repeatability and accuracy, the software should be developed by a professional multidisciplinary group.

REFERENCES

1. Dipova, N., "Use of Open Source Development Platforms in Geotechnical Laboratory Solutions", Vol. 8, No. 2, pp. 153–160, 2017.

2. SunFounder, *Tactile Pressure Sensor Solutions*, 2018, `https://www.tekscan.com/tactile-pressure-sensors`, accessed at September 2020.

3. O'Rourke, T. D., J. M. Jezerski, N. A. Olson, A. L. Bonneau, M. C. Palmer, H. E. Stewart, M. J. O'Rourke and T. Abdoun, "Geotechnics of pipeline system response to earthquakes", *Geotechnical Special Publication*, , No. 181, pp. 1–38, 2008.

4. Zhang, Z. and Y. H. Wang, "Examining setup mechanisms of driven piles in sand using laboratory model pile tests", *Journal of Geotechnical and Geoenvironmental Engineering*, Vol. 141, No. 3, pp. 1–12, 2015.

5. Watanabe, K., K. Tanaka, K. Iwane and S. Fukuma, "Sand Behavior Induced by High-Speed Penetration of Projectile", *AFOSR report*, Vol. AOARD-0940, 2011.

6. Entacher, M., G. Winter, T. Bumberger, K. Decker, I. Godor and R. Galler, "Cutter force measurement on tunnel boring machines - System design", *Tunnelling and Underground Space Technology*, Vol. 31, pp. 97–106, 2012.

7. Giwelli, A. A., K. Sakaguchi, A. Gumati and K. Matsuki, "Shear behaviour of fractured rock as a function of size and shear displacement", *Geomechanics and Geoengineering*, Vol. 9, No. 4, pp. 253–264, 2014.

8. Tabar, N. K., *Experimental and Numerical Simulation of Stress Distribution in Landfills*, Ph.D. Thesis, Carleton University, 2015.

9. Giri, P., K. Ng and W. Phillips, "Laboratory simulation to understand translational soil slides and establish movement criteria using wireless IMU sensors", *Landslides*,

Vol. 15, No. 12, pp. 2437–2447, 2018.

10. FujiFilm, *Pressure Measurement Film Prescale Products Guide*, 2020, https://bit.ly/3aY9jte, accessed at March 2020.

11. Science Learning Hub, University of Waikato, *Earth's magnetic field*, 2011, https://www.sciencelearn.org.nz/images/1820-earth-s-magnetic-field, accessed at March 2020.

12. AspenCore Electronics Tutorials, *Hall effect Sensor*, 2019, https://bit.ly/31gRink, accessed at March 2020.

13. SunFounder, *IMU Breakout - MPU-9250*, 2020, http://wiki.sunfounder.cc/index.php?title=IMU_Breakout_-_MPU-9250, accessed at August 2020.

14. Autodesk Instructables Circuits, *TCA9548A I2C Multiplexer Module With Arduino and NodeMCU*, 2018, https://www.instructables.com/TCA9548A-I2C-Multiplexer-Module-With-Arduino-and-N/, accessed at August 2020.

15. Wikipedia contributors, *Juansempere at English Wikipedia / CC BY-SA*, 2003, https://commons.wikimedia.org/wiki/File:Plane_with_ENU_embedded_axes.svg, accessed at April 2020.

16. The MathWorks, Inc., *Sensor Fusion and Tracking Toolbox*, Natick, Massachusetts, United States, 2019, https://www.mathworks.com/help/fusion/, accessed at April 2020.

17. The MathWorks, Inc., *Estimating Orientation Using Inertial Sensor Fusion and MPU-9250*, Natick, Massachusetts, United States, 2019, https://www.mathworks.com/help/supportpkg/arduinoio/ug/estimating-orientation\-using-inertial-sensor-fusion-and-mpu9250.html, accessed at April 2020.

18. Tokyo Measuring Instruments Laboratory Co, Ltd., *PDA-PB/PDB-PB Miniature Pressure Transducer 50kPa to 3MPa*, 2019, `https://tml.jp/e/product/transducers/pda_pdb.html`, accessed at June 2020.

19. Yahia, Y. I. O., *An Experimental Study On The Behavior Of Segmental Pile With Variable Flexural Rigidity (BAP-11A04D9)*, Ph.D. Thesis, Bogazici University, 2014.

20. Sengez, M., *Lateral capacity of segmental model piles under cyclic loading (BAP-18A04P2)*, Master's Thesis, Bogazici University, 2019.

21. Ramírez, A., J. Nielsen and F. Ayuga, "On the use of plate-type normal pressure cells in silos. Part 1: Calibration and evaluation", *Computers and Electronics in Agriculture*, Vol. 71, No. 1, pp. 71–76, 2010.

22. Labuz, J. F. and B. Theroux, "Laboratory calibration of earth pressure cells", *Geotechnical Testing Journal*, Vol. 28, No. 2, pp. 188–196, 2005.

23. Chen, W. and M. F. Randolph, "Measuring radial total stresses on model suction caissons in clay", *Geotechnical Testing Journal*, Vol. 30, No. 2, pp. 124–132, 2007.

24. Paikowsky, S. G., C. J. Palmer and A. F. DiMillio, "Visual observation and measurement of aerial stress distribution under a rigid strip footing", *Proceedings of the ASCE Geo-Institute Specialty Conference on Performance Confirmation of Constructed Geotechnical Facilities - Performance Confirmation of Constructed Geotechnical Facilities, GSP 94*, Vol. 300, pp. 148–169, American Society of Civil Engineers, Reston, VA, 2000.

25. Paikowsky, S. G., C. J. Palmer and L. E. Rolwes, "The use of tactile sensor technology for measuring soil stress distribution", *GeoCongress 2006: Geotechnical Engineering in the Information Technology Age*, Vol. 2006, p. 79, 2006.

26. Ha, D., T. H. Abdoun, M. J. O'Rourke, M. D. Symans, T. D. O'Rourke, M. C.

Palmer and H. E. Stewart, "Centrifuge Modeling of Earthquake Effects on Buried High-Density Polyethylene (HDPE) Pipelines Crossing Fault Zones", *Journal of Geotechnical and Geoenvironmental Engineering*, Vol. 134, No. 10, pp. 1501–1515, 2008.

27. Gao, Y. and Y. H. Wang, "Experimental and DEM examinations of K0 in sand under different loading conditions", *Journal of Geotechnical and Geoenvironmental Engineering*, Vol. 140, No. 5, pp. 1–11, 2014.

28. Kokkali, P., T. Abdoun and I. Anastasopoulos, "Tactile pressure sensors in centrifuge modeling of rocking foundations", *Geotechnical Special Publication*, Vol. GSP 256, pp. 74–83, 2015.

29. El-Sekelly, W., T. Abdoun and R. Dobry, "Effect of sand overconsolidation and extensive liquefaction on K0", *Geotechnical Special Publication*, , No. GSP 280, pp. 478–486, 2017.

30. Nicks, J. E., M. T. Adams and J. Li, "Use of Tactile Pressure Sensors to Measure Lateral Pressures at the Face of Geosynthetic Reinforced Soil Piers", *Geo-Congress 2019*, 2016, pp. 212–221, American Society of Civil Engineers, Reston, VA, 2019.

31. Ralphs, G., T. R. Lunsford and J. Greenfield, "Measurement of plantar pressure using fuji prescale film— A preliminary study", *Journal of Prosthetics and Orthotics*, Vol. 2, No. 2, pp. 130–138, 1990.

32. Patterson, R., D. Pogue and S. Viegas, "The effects of time and light exposure on contact and pressure measurements using Fuji prescale film.", *The Iowa Orthopaedic Journal*, Vol. 17, No. 409, pp. 64–69, 1997.

33. van de Sande, B., *Assessment of Fuji Pre-scale films in tyre / road contact surface measurements*, Master's Thesis, Eindhoven University of Technology, 2007.

34. Backx, P., *Tyre/road contact measurement using pressure sensitive film*, Master's

Thesis, Eindhoven University of Technology, 2007.

35. Cirello, A., G. Marannano and G. V. Mariotti, "Experimental analysis of the contact pressure distribution in an off-road tyre", *Journal of Strain Analysis for Engineering Design*, Vol. 44, No. 4, pp. 287–295, 2009.

36. Li, H. and C. Schindler, "Analysis of soil compaction and tire mobility with finite element method", *Proceedings of the Institution of Mechanical Engineers, Part K: Journal of Multi-body Dynamics*, Vol. 227, No. 3, pp. 275–291, 2013.

37. Baykal, G., "Three techniques for the study of soil structure interface properties; 3D roughness parameter; contact stress mapping; artificially manufactured sand", *Proceedings of the International geotechnical conference "'Soil-Structure Interaction. Underground Structures and Retaining Walls"*, pp. 119 – 126, 2014.

38. Jiang, X. Z. and Y. M. Shu, "Probabilistic analysis of random contact force between geomembrane and granular material", *Journal of Central South University*, Vol. 21, No. 8, pp. 3309–3315, 2014.

39. Nemoto, K., N. Watanabe, N. Hirano and N. Tsuchiya, "Direct measurement of contact area and stress dependence of anisotropic flow through rock fracture with heterogeneous aperture distribution", *Earth and Planetary Science Letters*, Vol. 281, No. 1-2, pp. 81–87, 2009.

40. Abadi, T., L. Le Pen, A. Zervos and W. Powrie, "Measuring the Area and Number of Ballast Particle Contacts at Sleeper-Ballast and Ballast-Subgrade Interfaces", *International Journal of Railway Technology*, Vol. 4, No. 2, pp. 45–72, 2015.

41. Kim, H., "Development of wireless sensor node for landslide detection", *Landslides and Engineered Slopes. From the Past to the Future*, pp. 1183–1187, CRC Press, 2008.

42. Giri, P., K. Ng, C. Robinson, W. Phillips and M. Phillips, "Understanding the

Behavior of Rock-Fall Motion Using Wireless Sensor Technology", *Geo-Chicago 2016*, 2015, pp. 584–595, American Society of Civil Engineers, Reston, VA, 2016.

43. Weerasinghe, R. M., D. Buddika and R. M. Chandima Ratnayake, "IMU Based Real Time Underground Soil Movement Detection System: An Illustrative Investigation", *IEEE International Conference on Industrial Engineering and Engineering Management*, Vol. 2019-Decem, pp. 1016–1020, 2019.

44. Park, S. S., N. P. Doan, S. W. Woo and J. S. Lee, "Numerical Prediction of Soil Displacement Based on Imu Sensor Measurement", *International Journal of Innovative Technology and Exploring Engineering*, Vol. 8, No. 8, pp. 317–322, 2019.

45. Wikipedia contributors, *Magnetometer — Wikipedia, The Free Encyclopedia*, 2003, `https://en.wikipedia.org/wiki/Magnetometer`, accessed at March 2020.

APPENDIX A: ADDITIONAL RESULTS

The degree of change in blocks for experiments 1, 2, 3, 4, and 5 is presented in Table A.1-A.1, Table A.2-A.2, Table A.3-A.3, Table A.4-A.4, and Table A.5-A.5, respectively.

Table A.1. Degree of change in x, y and z axes from experiment 1.

Deflection at Mid Point (cm)	**X (Degree)**	**Y (Degree)**	**Z (Degree)**
Block 2			
0.50	0.75	0.80	-0.25
1.00	0.60	0.38	-0.06
1.50	0.48	0.99	-0.16
2.00	0.94	0.96	-5.53
Block 3			
0.50	-2.71	-0.45	-0.81
1.00	-2.62	0.44	-3.01
1.50	-2.84	0.99	-5.37
2.00	-2.52	-0.62	0.49
Block 4			
0.50	-0.45	-0.04	-1.87
1.00	-0.64	1.41	-3.97
1.50	-0.83	1.79	-6.34
2.00	-0.24	0.83	-0.43
Block 5			
0.50	-1.97	3.46	-3.82
1.00	-2.24	4.04	-1.79
1.50	-2.43	5.92	-0.48
2.00	-1.78	4.17	-5.15
Block 6			
0.50	-3.26	2.60	4.79
1.00	-3.76	3.62	3.37
1.50	-4.35	5.11	1.89
2.00	-3.02	6.47	6.07

Table A.1. Degree of change in x, y and z axes from experiment 1 (cont.).

Deflection at Mid Point (cm)	**X (Degree)**	**Y (Degree)**	**Z (Degree)**
Block 7			
0.50	0.97	6.56	5.68
1.00	0.47	6.88	5.94
1.50	0.69	7.74	6.23
2.00	1.07	5.88	5.46
Block 8			
0.50	87.18	5.68	6.22
1.00	87.40	5.92	7.69
1.50	77.72	5.41	6.77
2.00	32.08	9.57	8.02
Block 9			
0.50	7.38	6.91	0.78
1.00	7.49	7.55	2.42
1.50	7.10	7.32	3.54
2.00	15.06	6.67	8.58
Block 10			
0.50	N/A	N/A	N/A
1.00	N/A	N/A	N/A
1.50	N/A	N/A	N/A
2.00	N/A	N/A	N/A
Block 11			
0.50	3.55	3.15	0.77
1.00	3.59	2.87	1.19
1.50	3.97	4.18	3.39
2.00	3.20	4.74	2.55

Table A.1. Degree of change in x, y and z axes from experiment 1 (cont.).

Deflection at Mid Point (cm)	**X (Degree)**	**Y (Degree)**	**Z (Degree)**
Block 12			
0.50	-1.05	3.20	3.42
1.00	-0.48	3.41	1.21
1.50	-0.06	3.42	1.06
2.00	-1.12	4.26	4.99
Block 13			
0.50	-7.06	-1.56	6.80
1.00	-6.88	-1.31	4.74
1.50	-6.69	-1.30	2.51
2.00	-7.17	-2.40	8.28
Block 14			
0.50	-0.72	0.33	0.55
1.00	-0.26	0.29	0.27
1.50	0.02	0.57	0.02
2.00	-0.81	0.69	0.01

Table A.2. Degree of change in x, y and z axes from experiment 2.

Deflection at Mid Point (cm)	**X (Degree)**	**Y (Degree)**	**Z (Degree)**
Block 2			
0.50	0.02	0.26	-0.35
1.00	0.76	0.28	-0.35
1.50	0.68	0.35	-0.02
2.00	0.82	0.66	-0.71
Block 3			
0.50	-2.24	0.17	-0.87
1.00	-2.33	0.37	-3.11
1.50	-2.48	0.47	-5.61
2.00	-2.37	-0.32	-1.63
Block 4			
0.50	-0.35	0.65	-1.63
1.00	-0.40	1.46	-3.93
1.50	-0.59	1.84	-6.33
2.00	-0.15	1.21	-2.47
Block 5			
0.50	-1.97	4.28	-4.19
1.00	-1.96	5.00	-1.94
1.50	-2.29	6.27	-0.26
2.00	-1.78	4.94	-3.37
Block 6			
0.50	-3.21	4.08	-5.52
1.00	-3.83	4.52	-3.98
1.50	-4.28	6.11	-2.44
2.00	-3.58	4.98	-5.26

Table A.2. Degree of change in x, y and z axes from experiment 2 (cont.).

Deflection at Mid Point (cm)	**X (Degree)**	**Y (Degree)**	**Z (Degree)**
Block 7			
0.50	0.98	4.04	8.04
1.00	1.12	6.09	7.95
1.50	1.16	8.27	8.11
2.00	1.03	4.99	8.86
Block 8			
0.50	62.74	6.88	6.86
1.00	64.16	6.92	7.94
1.50	72.71	7.28	7.57
2.00	57.73	6.57	5.75
Block 9			
0.50	7.56	4.70	0.21
1.00	7.39	4.83	-1.14
1.50	7.60	5.10	-2.90
2.00	7.22	4.69	0.30
Block 10			
0.50	N/A	N/A	N/A
1.00	N/A	N/A	N/A
1.50	N/A	N/A	N/A
2.00	N/A	N/A	N/A
Block 11			
0.50	3.96	3.35	1.27
1.00	4.46	4.12	0.98
1.50	4.81	4.46	3.45
2.00	3.88	3.29	1.06

Table A.2. Degree of change in x, y and z axes from experiment 2 (cont.).

Deflection at Mid Point (cm)	**X (Degree)**	**Y (Degree)**	**Z (Degree)**
Block 12			
0.50	0.03	2.21	3.51
1.00	0.38	3.07	1.23
1.50	0.78	3.71	-1.09
2.00	0.21	3.68	3.02
Block 13			
0.50	-6.45	-3.90	7.02
1.00	-6.40	-4.27	4.94
1.50	-6.02	-4.32	2.66
2.00	-6.49	-3.91	6.67
Block 14			
0.50	0.00	0.34	0.75
1.00	0.54	0.65	0.43
1.50	0.75	0.59	0.15
2.00	0.10	0.00	0.46

Table A.3. Degree of change in x, y and z axes from experiment 3.

Deflection at Mid Point (cm)	**X (Degree)**	**Y (Degree)**	**Z (Degree)**
Block 2			
0.50	0.97	0.33	-0.42
1.00	0.68	0.17	-0.36
1.50	0.63	0.79	-0.89
2.00	0.12	0.82	-0.56
Block 3			
0.50	-2.01	0.07	-1.85
1.00	-2.12	0.74	-4.26
1.50	-2.12	1.34	-6.59
2.00	-1.83	0.04	0.38
Block 4			
0.50	-0.01	0.90	-2.77
1.00	-0.29	1.41	-5.05
1.50	-0.42	3.26	-7.39
2.00	0.19	1.04	-0.38
Block 5			
0.50	-1.67	4.65	-3.06
1.00	-1.81	5.25	-0.89
1.50	-2.07	6.59	-1.32
2.00	-1.66	3.16	-5.39
Block 6			
0.50	-3.47	3.89	4.87
1.00	-3.94	5.81	3.19
1.50	-4.38	7.70	1.69
2.00	-2.95	3.24	6.58

Table A.3. Degree of change in x, y and z axes from experiment 3 (cont.).

Deflection at Mid Point (cm)	**X (Degree)**	**Y (Degree)**	**Z (Degree)**
Block 7			
0.50	1.01	4.07	8.13
1.00	1.21	5.72	8.01
1.50	1.19	7.93	8.34
2.00	1.17	5.92	8.12
Block 8			
0.50	59.77	4.79	8.02
1.00	63.59	4.88	8.77
1.50	65.97	5.19	8.20
2.00	45.31	3.08	8.16
Block 9			
0.50	7.28	6.38	0.00
1.00	7.70	7.71	2.06
1.50	7.73	7.63	3.64
2.00	6.82	7.19	2.19
Block 10			
0.50	N/A	N/A	N/A
1.00	N/A	N/A	N/A
1.50	N/A	N/A	N/A
2.00	N/A	N/A	N/A
Block 11			
0.50	4.10	3.22	0.46
1.00	4.62	4.30	1.91
1.50	4.95	5.28	4.36
2.00	3.76	3.35	2.92

Table A.3. Degree of change in x, y and z axes from experiment 3 (cont.).

Deflection at Mid Point (cm)	**X (Degree)**	**Y (Degree)**	**Z (Degree)**
Block 12			
0.50	0.55	3.03	2.40
1.00	0.69	2.58	0.09
1.50	1.28	2.79	-2.24
2.00	-0.18	2.93	4.92
Block 13			
0.50	-6.29	-3.59	6.10
1.00	-6.15	-3.16	4.01
1.50	-5.69	-3.38	1.63
2.00	-6.37	-3.07	8.37
Block 14			
0.50	0.45	0.55	0.68
1.00	0.84	0.79	0.34
1.50	1.20	0.17	0.02
2.00	0.31	0.30	0.74

Table A.4. Degree of change in x, y and z axes from experiment 4.

Deflection at Mid Point (cm)	**X (Degree)**	**Y (Degree)**	**Z (Degree)**
Block 2			
0.50	0.19	0.00	0.81
1.00	0.06	0.92	0.87
1.50	0.81	0.88	-0.85
2.00	0.19	0.33	0.70
Block 3			
0.50	-1.25	-0.55	-1.53
1.00	-1.63	-1.15	-3.54
1.50	-1.65	0.29	-5.28
2.00	-1.78	-1.25	-0.45
Block 4			
0.50	-0.40	0.50	-1.94
1.00	-0.79	1.36	-3.88
1.50	-0.80	2.70	-5.60
2.00	-0.81	0.00	-0.92
Block 5			
0.50	-2.29	0.54	-4.51
1.00	-2.44	1.61	-2.81
1.50	-2.76	2.91	-1.17
2.00	-2.69	0.40	-5.50
Block 6			
0.50	-2.82	-7.45	3.67
1.00	-3.20	-5.43	2.46
1.50	-3.76	-4.88	1.01
2.00	-3.11	-7.81	1.57

Table A.4. Degree of change in x, y and z axes from experiment 4 (cont.).

Deflection at Mid Point (cm)	**X (Degree)**	**Y (Degree)**	**Z (Degree)**
Block 7			
0.50	0.97	4.45	6.88
1.00	0.90	6.19	6.20
1.50	0.81	6.82	4.84
2.00	0.92	7.41	6.76
Block 8			
0.50	15.56	4.90	5.16
1.00	17.13	8.95	3.42
1.50	18.27	7.08	2.36
2.00	15.13	6.12	5.23
Block 9			
0.50	7.62	5.79	2.79
1.00	7.15	6.23	2.36
1.50	6.70	6.16	1.55
2.00	6.56	6.66	3.88
Block 10			
0.50	N/A	N/A	N/A
1.00	N/A	N/A	N/A
1.50	N/A	N/A	N/A
2.00	N/A	N/A	N/A
Block 11			
0.50	3.96	3.99	2.73
1.00	4.37	5.98	0.77
1.50	4.56	4.55	1.16
2.00	3.70	3.98	3.86

Table A.4. Degree of change in x, y and z axes from experiment 4 (cont.).

Deflection at Mid Point (cm)	**X (Degree)**	**Y (Degree)**	**Z (Degree)**
Block 12			
0.50	0.41	2.05	5.24
1.00	1.12	2.16	2.90
1.50	1.53	3.35	0.85
2.00	0.23	2.26	6.24
Block 13			
0.50	-1.99	1.06	5.11
1.00	-1.70	0.71	2.86
1.50	-1.44	0.50	0.81
2.00	-2.12	0.96	6.23
Block 14			
0.50	3.00	0.55	0.25
1.00	3.42	0.91	0.03
1.50	3.71	0.99	0.04
2.00	2.72	0.73	0.43

Table A.5. Degree of change in x, y and z axes from experiment 5.

Deflection at Mid Point (cm)	**X (Degree)**	**Y (Degree)**	**Z (Degree)**
Block 2			
0.50	8.46	0.10	-0.27
1.00	8.39	0.26	-0.23
1.50	8.45	0.83	-0.85
2.00	8.37	0.49	-0.81
Block 3			
0.50	-0.80	-0.15	-1.10
1.00	-0.70	0.09	-3.21
1.50	-0.87	0.95	-5.10
2.00	-0.85	0.84	-3.46
Block 4			
0.50	0.05	0.16	-1.74
1.00	-0.10	0.62	-3.64
1.50	-0.10	1.17	-5.62
2.00	-0.24	1.52	-3.94
Block 5			
0.50	-2.59	-2.05	-5.57
1.00	-3.06	-2.45	-4.02
1.50	-3.02	-3.45	-2.48
2.00	-2.91	-3.16	-4.13
Block 6			
0.50	-2.58	-2.14	4.14
1.00	-2.89	-2.42	2.79
1.50	-3.39	-3.98	1.54
2.00	-2.99	-3.36	2.63

Table A.5. Degree of change in x, y and z axes from experiment 5 (cont.).

Deflection at Mid Point (cm)	**X (Degree)**	**Y (Degree)**	**Z (Degree)**
Block 7			
0.50	1.41	2.42	7.27
1.00	1.51	3.93	6.28
1.50	1.26	4.21	5.10
2.00	1.54	3.82	6.24
Block 8			
0.50	14.65	7.43	7.35
1.00	15.55	6.82	6.38
1.50	16.38	6.29	5.71
2.00	14.97	6.12	6.68
Block 9			
0.50	7.01	5.70	4.10
1.00	7.06	6.56	3.10
1.50	7.26	6.67	1.82
2.00	6.49	6.62	3.62
Block 10			
0.50	N/A	N/A	N/A
1.00	N/A	N/A	N/A
1.50	N/A	N/A	N/A
2.00	N/A	N/A	N/A
Block 11			
0.50	4.69	4.86	3.12
1.00	4.86	3.39	1.17
1.50	4.96	3.93	-0.79
2.00	4.89	3.87	0.94

Table A.5. Degree of change in x, y and z axes from experiment 5 (cont.).

Deflection at Mid Point (cm)	**X (Degree)**	**Y (Degree)**	**Z (Degree)**
Block 12			
0.50	0.95	3.68	5.39
1.00	1.29	3.90	3.23
1.50	1.71	3.81	1.11
2.00	1.47	3.98	2.83
Block 13			
0.50	-1.22	3.14	5.05
1.00	-1.08	3.06	2.73
1.50	-0.87	3.80	0.67
2.00	-1.09	3.64	2.57
Block 14			
0.50	0.56	0.45	0.51
1.00	0.79	0.87	0.33
1.50	0.00	0.51	0.13
2.00	0.79	0.34	0.02

APPENDIX B: SOURCE CODE

The source code of the Arduino sketch is presented in this section.

B.1. ARDUINO SKETCH

As described in the methodology chapter, each port in the multiplexer is occupied by two IMUs, say IMU00(0x68) and IMU01(0x69). The serial port of the Arduino board is directly listening by MATLAB. Therefore, the order of the array sent through the serial port to MATLAB is essential.

The data is sent line by line to MATLAB. Each of these lines corresponds to data from one port, meaning that two of the sensors. An example line and the order of the data is explained below.

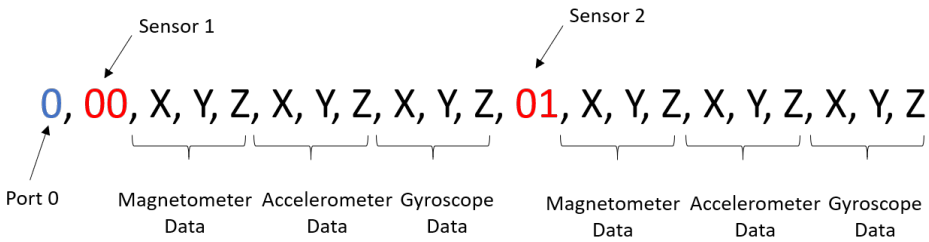

Figure B.1. An example line sent from arduino to matlab.

```
#include <Esplora.h>
#include <Arduino.h>
#include "MPU9250.h"
#include "TCA9548A.h"
#define SERIAL_BAUD 115200
TCA9548A I2CMux;
const float R2D = 180.0f / PI;
MPU9250 IMU00(Wire,0x68);
MPU9250 IMU01(Wire,0x69);
int status00;
int status01;
int portNumber;
void setup() {
 Serial.begin(SERIAL_BAUD);
 while(!Serial) {}
 I2CMux.begin(Wire);          // TwoWire isntance can be passed here as 3rd argument
 for (portNumber = 0; portNumber < 7; portNumber++) {
  I2CMux.openChannel(portNumber);
  Serial.print("\nChannel ");
  Serial.print(portNumber);
  Serial.print("\n");
  status00 = IMU00.begin();
  if (status00 < 0) {
  Serial.println("IMU00: NO CONNECTION");
  //Serial.print("Status: ");
  //Serial.print(status00);
  } else {
  Serial.println("IMU00: OK");
  IMU00.setAccelRange(MPU9250::ACCEL_RANGE_8G);
  IMU00.setGyroRange(MPU9250::GYRO_RANGE_500DPS);
  IMU00.setDlpfBandwidth(MPU9250::DLPF_BANDWIDTH_20HZ);
```

```
if (portNumber == 0) {
IMU00.setAccelCalX(0.03,1);
IMU00.setAccelCalY(0.10,1.01);
IMU00.setAccelCalZ(0.13,0.99);
IMU00.setGyroBiasX_rads(0.029426);
IMU00.setGyroBiasY_rads(0.013665);
IMU00.setGyroBiasZ_rads(-0.001558);
}
else if (portNumber == 1) {
IMU00.setAccelCalX(0.10,1);
IMU00.setAccelCalY(0.10,1);
IMU00.setAccelCalZ(0.24,0.99);
IMU00.setGyroBiasX_rads(0.005216);
IMU00.setGyroBiasY_rads(-0.017311);
IMU00.setGyroBiasZ_rads(0.020368);
}
else if (portNumber == 2) {
IMU00.setAccelCalX(0.13,1);
IMU00.setAccelCalY(0.05,1);
IMU00.setAccelCalZ(0.17,0.99);
IMU00.setGyroBiasX_rads(-0.012235);
IMU00.setGyroBiasY_rads(-0.029471);
IMU00.setGyroBiasZ_rads(-0.007208);
}
else if (portNumber == 3) {
IMU00.setAccelCalX(0.02,1);
IMU00.setAccelCalY(0.15,1);
IMU00.setAccelCalZ(0.21,0.98);
IMU00.setGyroBiasX_rads(0.000077);
IMU00.setGyroBiasY_rads(0.013385);
IMU00.setGyroBiasZ_rads(-0.003772);
```

```
}
else if (portNumber == 4) {
IMU00.setAccelCalX(-0.01,1);
IMU00.setAccelCalY(-0.03,1);
IMU00.setAccelCalZ(-0.33,0.99);
IMU00.setGyroBiasX_rads(0.027860);
IMU00.setGyroBiasY_rads(0.000387);
IMU00.setGyroBiasZ_rads(-0.025222);
}
else if (portNumber == 5) {
IMU00.setAccelCalX(0.04,1);
IMU00.setAccelCalY(0.16,1);
IMU00.setAccelCalZ(0.20,1);
IMU00.setGyroBiasX_rads(-0.004097);
IMU00.setGyroBiasY_rads(0.019168);
IMU00.setGyroBiasZ_rads(0.005028);
}
else if (portNumber == 6) {
IMU00.setAccelCalX(0.17,1);
IMU00.setAccelCalY(0.23,1);
IMU00.setAccelCalZ(0,1);
IMU00.setGyroBiasX_rads(0.041815);
IMU00.setGyroBiasY_rads(0.011026);
IMU00.setGyroBiasZ_rads(0.016339);
}
IMU00.setSrd(19);
}
status01 = IMU01.begin();
if (status01 < 0) {
Serial.println("IMU01: NO CONNECTION");
//Serial.print("Status: ");
```

```
//Serial.print(status01);
} else {
Serial.println("IMU01: OK");
IMU01.setAccelRange(MPU9250::ACCEL_RANGE_8G);
IMU01.setGyroRange(MPU9250::GYRO_RANGE_500DPS);
IMU01.setDlpfBandwidth(MPU9250::DLPF_BANDWIDTH_20HZ);
IMU01.setSrd(19);
if (portNumber == 0) {
IMU01.setAccelCalX(0.05,1);
IMU01.setAccelCalY(0.04,1);
IMU01.setAccelCalZ(-0.67,0.99);

IMU01.setGyroBiasX_rads(0.006217);
IMU01.setGyroBiasY_rads(0.011562);
IMU01.setGyroBiasZ_rads(0.004025);
}
else if (portNumber == 1) {
IMU01.setAccelCalX(0.09,1);
IMU01.setAccelCalY(0.02,1);
IMU01.setAccelCalZ(0.27,0.98);
IMU01.setGyroBiasX_rads(-0.011974);
IMU01.setGyroBiasY_rads(-0.015734);
IMU01.setGyroBiasZ_rads(0.020897);
}
else if (portNumber == 2) {
IMU01.setAccelCalX(0.01,1);
IMU01.setAccelCalY(-0.03,1.01);
IMU01.setAccelCalZ(0,1);
IMU01.setGyroBiasX_rads(-0.010849);
IMU01.setGyroBiasY_rads(0.003650);
IMU01.setGyroBiasZ_rads(-0.001928);
```

```
}
else if (portNumber == 3) {
IMU01.setAccelCalX(0,1);
IMU01.setAccelCalY(0.06,1.01);
IMU01.setAccelCalZ(-0.78,0.99);
IMU01.setGyroBiasX_rads(-0.006472);
IMU01.setGyroBiasY_rads(-0.001545);
IMU01.setGyroBiasZ_rads(0.006557);
}
else if (portNumber == 4) {
IMU01.setAccelCalX(0.14,1);
IMU01.setAccelCalY(0.31,1);
IMU01.setAccelCalZ(0,1);
IMU01.setGyroBiasX_rads(0.017970);
IMU01.setGyroBiasY_rads(0.002599);
IMU01.setGyroBiasZ_rads(0.003578);
}
else if (portNumber == 5) {
IMU01.setAccelCalX(0.02,1);
IMU01.setAccelCalY(0.02,1.01);
IMU01.setAccelCalZ(0.78,0.99);
IMU01.setGyroBiasX_rads(-0.007073);
IMU01.setGyroBiasY_rads(0.007787);
IMU01.setGyroBiasZ_rads(-0.000736);
}
else if (portNumber == 6) {
IMU01.setAccelCalX(0.15,1);
IMU01.setAccelCalY(0.08,1);
IMU01.setAccelCalZ(0.20,0.99);
IMU01.setGyroBiasX_rads(0.013582);
IMU01.setGyroBiasY_rads(-0.014905);
```

```
    IMU01.setGyroBiasZ_rads(0.001281);
    }
    }
    I2CMux.closeChannel(portNumber);
  }
}
void loop() {
  I2CMux.begin(Wire);
  for (portNumber = 0; portNumber < 7; portNumber++) {
    I2CMux.openChannel(portNumber);
    Serial.print(portNumber);
    Serial.print(",");
    Serial.print("00,");
    IMU00.readSensor();
    Serial.print(IMU00.getMagX_uT(),6);
    Serial.print(",");
    Serial.print(IMU00.getMagY_uT(),6);
    Serial.print(",");
    Serial.print(IMU00.getMagZ_uT(),6);
    Serial.print(",");
    Serial.print(IMU00.getAccelX_mss(),6);
    Serial.print(",");
    Serial.print(IMU00.getAccelY_mss(),6);
    Serial.print(",");
    Serial.print(IMU00.getAccelZ_mss(),6);
    Serial.print(",");
    Serial.print(IMU00.getGyroX_rads(),6);
    Serial.print(",");
    Serial.print(IMU00.getGyroY_rads(),6);
    Serial.print(",");
    Serial.print(IMU00.getGyroZ_rads(),6);
```

```
    Serial.print(",");
    Serial.print("01,");
    IMU01.readSensor();
    Serial.print(IMU01.getMagX_uT(),6);
    Serial.print(",");
    Serial.print(IMU01.getMagY_uT(),6);
    Serial.print(",");
    Serial.print(IMU01.getMagZ_uT(),6);
    Serial.print(",");
    Serial.print(IMU01.getAccelX_mss(),6);
    Serial.print(",");
    Serial.print(IMU01.getAccelY_mss(),6);
    Serial.print(",");
    Serial.print(IMU01.getAccelZ_mss(),6);
    Serial.print(",");
    Serial.print(IMU01.getGyroX_rads(),6);
    Serial.print(",");
    Serial.print(IMU01.getGyroY_rads(),6);
    Serial.print(",");
    Serial.print(IMU01.getGyroZ_rads(),6);
    Serial.print("\n");
    delay(1);
    I2CMux.closeChannel(portNumber);
  }
}
```